FIRST PRINCIPLES INVESTIGATION OF STRUCTURAL, MECHANICAL AND THERMODYNAMIC PROPERTIES OF MAX PHASES

A Dissertation

by

WOONGRAK SON

Submitted to the Office of Graduate and Professional Studies of
Texas A&M University
in partial fulfillment of the requirements for the degree of

DOCTOR OF PHILOSOPHY

Chair of Committee,	Raymundo Arróyave
Committee Members,	Miladin Radovic
	Xiaofeng Qian
	Ankit Srivastava
	Choongho Yu
Head of Department,	Ibrahim Karaman

August 2018

Major Subject: Materials Science and Engineering

ABSTRACT

MAX phases are layered carbides or nitrides with general formula of $M_{n+1}AX_n$. In this work we present a first principles investigation of structural, mechanical, and thermodynamic properties of MAX phases. Up to date approximately 70 pure MAX phases are synthesized and characterized. But the possible number of MAX phases is large when we consider different chemicals in M, A, and X sublattices as well as the possible stacking numbers, n. First, we studied Ti_3AlC_2, Ti_3SiC_2, and their solid solutions to understand the composition-properties relationship. Among the pure MAX phases, the Al-containing MAX phases are some of the most important as they are considered to be promising high-temperature applicable materials. They are known to form continuous alumina layer when exposed to high temperature oxidizing environment, and have excellent oxidation properties. While their overall strength is low compared to other MAX phases. In contrast, the Si-containing MAX phases have excellent mechanical properties. Finally solid solution MAX phases offer the opportunity to tune the thermodynamic, and mechanical properties of MAX phases. Solid solution MAX phases were modeled using special quasirandom structures (SQS), and calculated thermodynamic and mechanical properties using Density Functional Theory (DFT), which is implemented in the Vienna Ab initio Simulation Package (VASP). Second, we studied $Ti_{n+1}AlC_n$ and $Ta_{n+1}AlC_n$ systems to understand structure-properties relationship, and to address the effect of stacking layers, and the effect of different M chemicals on deformation behavior. Since, many MAX phases with n = 1-3 have studied, but higher order MAX phases have not been studied in detail. Third, we studied the cleavage and shear behavior of TiC, Ti_2AlC, Ti, and graphite to understand what is MAX phases in terms of the deformation behavior. MAX phases have a unique combination of properties, which are both of metals and ceramics, since MAX phases have ceramic like MX layers and metal like A layers. By comparing deformation behaviors of different types of layers materials, we studied whether the deformation behavior of MAX phases is similar to ceramics or metals. Lastly, we studied structural and elastic properties of $(M_1M_2)AlC$ systems, and the deformation behaviors of M_2AlC systems. The critical stress and

USFE of M_2AlC have a good trend in the periodic table, and the analysis suggest that some M_2AlC MAX phases have stable or metastable state in the sheared structure.

DEDICATION

To my mother, my father, my brother, and my wife.

ACKNOWLEDGMENTS

CONTRIBUTORS AND FUNDING SOURCES

Contributors

Funding Sources

TABLE OF CONTENTS

LIST OF FIGURES

x

xii

1. INTRODUCTION

$M_{n+1}AX_n$, or in short MAX, phases are a group of nanolayered hexagonal compounds, wherein $M_{n+1}X_n$ layers are interleaved with A layers. M is typically early transition metals, A is mostly 13 and 14 groups elements, and X is carbon or nitrogen. MAX phases have a unique combination of properties, which are both of metals and ceramics. Like metals, MAX phases are relatively soft and readily machinable with good thermal shock resistance and good damage tolerance. In addition, like ceramics, MAX phases have good chemical resistance and thermal stability [9, 10, 11].

Among the 70 pure MAX phases synthesized and characterized to date, the Al-containing MAX phases, such as Ti_2AlC and Ti_3AlC_2, are important as they have good thermal stability and chemical resistance, since the passivating continuous alumina layer is formed when exposed to high-temperature oxidation environment [12, 13, 14]. Besides , these MAX phases exhibit self healing-behavior. The alumina layers are formed when cracks exposed to oxidizing environments as Al migrates from Al layer to react with oxygen in atmosphere [15]. Many Al-containing MAX phases have excellent thermal stability and chemical resistance, while these MAX phases have relatively low strength when compared to other MAX phases. In contrast to Al-containing MAX phases, Si-containing MAX phases, such as Ti_2SiC and Ti_3SiC_2, have good mechanical properties [16, 17]. The ultimate goal is that tuning the properties beyond the pure MAX phases through making solid solution MAX phases. In this research we studied $Ti_3Si_xAl_{1-x}C_2$, which has the combination of Si and Al in the A lattice sites, to have not only good thermal stability and chemical resistance, but also have good mechanical properties.

Depending on the number of n, MAX phases have a different number of MAX stacking layers between A layers. The higher order MAX phases have not studied in detail even though they offer the opportunity to tune the properties like solid solutions [18]. By the example of $Ti_{n+1}SiC_n$, it is known that the bulk modulus is increasing from 205 GPa with n = 1, to 254 GPa with n = 4 [19]. In this research we studied $Ti_{n+1}AlC_n$ and $Ta_{n+1}AlC_n$ with n = 1 - 5. Two different interfacial energetics, cleavage and shear, are considered to study deformation behavior to address a response

1

of material to applied stress.

The M-A bond is important on deformation behavior, since the M-A bond strength is relatively weaker than the M-X bond strength. To understand the M-A bond compare to other bonding types, for instance, ionic bond, metallic bond, and van der Waals force, we studied cleavage and shear behavior of TiC, Ti_2AlC, Ti, and graphite.

The possible number of MAX phases are large, thus we studied structural and elastic properties of $(M_1M_2)AlC$ and deformation behaviors of M_2AlC to study composition-properties relationship in MAX phases.

In this work, we studied the structural, elastic, and thermodynamic properties, and deformation behaviors of Ti_3AlC_2, Ti_3SiC_2, and their solid solutions. We study the cleavage and shear energetics of $Ti_{n+1}AlC_n$ and $Ta_{n+1}AlC_n$ to study the effect of the number of stacking layers and different M chemical effect on deformation behavior. In addition, we studied the cleavage and shear behavior of TiC, Ti2AlC, Ti, and graphene to understand deformation energetics with different bonding types. Lastly we studied the structural and elastic properties of $(M_1M_2)AlC$ and deformation behaviors of M_2AlC to study composition-properties relationship in MAX phases.

2. LITERATURE REVIEW

2.1 Experimental Work

In the 1960s, H. Nowotny and co-workers discovered a new class of carbide and nitride phases, named H-phases, which is now MAX phases. The distribution of H-phases are listed in Table 2.1, and they are synthesized by hot-pressing from powder mixtures [5, 6, 7, 8]. In the 1990s, Barsoum et al. have reported fully dense and pure Ti_3SiC_2 phase, fabricated from Ti, C, and SiC powders by hot-pressing, with a total SiC and TiC_x content that was less than 1% [20]. The fully dense sample increases the oxidation resistance. For example, the parabolic rate constant of 95% dense sample reported by [21] et al. is roughly 3 orders higher than the fully dense sample reported by [20] et al. One of the most importance is that Ti_3SiC_2 has a unique combination of properties, which is both of metals and ceramics. Like metals, it is easily machinable, relatively soft, and an excellent electric and thermal conductor. Like ceramics, it is elastically stiff and oxidation resistant. The Young's modulus of Ti_3SiC_2 was estimated to be 320 GPa using the resonance frequency technique shows that it is elastically stiff material. The machinability is shown by the SEM image of the cross-section of the threaded hole. Holes are easily drillable using commonly available high-speed steel drill and form very precise internal thread. In the 2000s, Zhang et al. have synthesized high purity of Ti_3SiC_2 from powders by spark plasma sintering (SPS), which is more competitive sintering technique compare to the hot-pressing [22]. With the help of SPS technique, MAX phases can be rapidly sintered under relatively low temperature and short time. The MAX phases are in the general form of $M_{n+1}AX_n$, and n = 1-6. M represents an early transition metal, A represents an A group element, X represents carbon or nitrogen. M_2AX, M_3AX_2, M_4AX_4, M_5AX_4, M_6AX_5, and M_7AX_6 are referred to 211, 312, 413, 514, 615, and 716, depending on the number of n. So the family of MAX phases is very large, and the properties of MAX phases can be tuned with different chemical elements. To date, over 70 pure MAX phases, ternary MAX phases, are known to be synthesized, and still the tunability is very high by synthesizing solid solution MAX phases [18].

	Ternary Carbides	Ternary Nitrides
211 phases	Ti_2AlC, Ti_2GaC, Ti_2GeC, Ti_2CdC, Ti_2InC, Ti_2SnC, Ti_2TlC, Ti_2PbC	Ti_2AlN, Ti_2GaN, Ti_2InN
	V_2AlC, V_2GaC, V_2GeC	Zr_2InN
	Cr_2AlC, Cr_2GaC, Cr_2GeC,	
	Zr_2InC, Zr_2SnC, Zr_2TlC, Zr_2PbC	
	Nb_2AlC, Nb_2GaC, Nb_2InC, Nb_2SnC	
	Mo_2GaC	
	Hf_2InC, Hf_2SnC, Hf_2TlC, Hf_2PbC	
	Ta_2AlC Ta_2GaC	
312 phases	Ti_3SiC_2, Ti_3GeC_2	

Table 2.1: 211 and 312 H-phases [5, 6, 7, 8].

2.2 Density Functional Theory (DFT)

Density Functional Theory (DFT) is a very popular quantum mechanical calculations in solid-state physics to investigate properties of materials such as structure, free energy, elastic constants, etc. DFT is independent of experimental data and relies on the basis of quantum mechanical considerations known as first principles or ab initio approaches. In 1926, Erwin Schrödinger introduced Schrödinger equation, which is a partial differential equation describes the wave function of system [23]. In solid-state physics, the goal of most approaches is to solve the time-independent, non-relativistic Schrödinger equation:

$$\hat{H}\psi_i(\vec{x}_1, \vec{x}_2, \ldots, \vec{x}_N, \vec{R}_1, \vec{R}_2, \ldots, \vec{R}_M) = E_i\psi_i(\vec{x}_1, \vec{x}_2, \ldots, \vec{x}_N, \vec{R}_1, \vec{R}_2, \ldots, \vec{R}_M),$$

(2.1)

where $\hat{H}$ is the Hamiltonian for a system consisting of M nuclei and N electrons, ψ is the wave-function and E is the energy. The Hamiltonian is given by:

$$\hat{H} = -\frac{1}{2}\sum_{i=1}^{N}\nabla_i^2 - \frac{1}{2}\sum_{A=1}^{M}\frac{1}{M_A}\nabla_A^2 - \sum_{i=1}^{N}\sum_{A=1}^{M}\frac{Z_A}{r_{iA}} + \sum_{i=1}^{N}\sum_{j>1}^{N}\frac{1}{r_{ij}} + \sum_{A=1}^{M}\sum_{B>A}^{M}\frac{Z_AZ_B}{R_{AB}}.$$

(2.2)

4

The first and second terms describe the kinetic energy of the electrons and nuclei. The third term represents the attractive electrostatic interaction between the electrons and nuclei. The fourth term represents the repulsive potential due to the electron-electron interactions, and the fifth term represents the repulsive potential due to the nucleus-nucleus interactions. In 1927, Born-Oppenheimer approximation was proposed [24]. This approximation considers the electrons move in the field of fixed nuclei, hence the nuclear kinetic energy is zero, and their potential energy is constant. Since the mass of nuclei is much higher than the mass of electrons, so nuclei move much slower than electrons. Then, the electronic Hamiltonian reduces to

$$\hat{H}_{elec} = -\frac{1}{2}\sum_{i=1}^{N}\nabla_i^2 - \sum_{i=1}^{N}\sum_{A=1}^{N}\frac{Z_A}{r_{iA}} + \sum_{i=1}^{N}\sum_{j>i}^{N}\frac{1}{r_{ij}}. \tag{2.3}$$

The Schrödinger equation equation reduces to

$$\hat{H}_{elec}\psi_{elec} = E_{elec}\psi_{elec}. \tag{2.4}$$

, where $\hat{H}_{elec}$ is the electronic Hamiltonian, ψ_{elec} is the electronic wave function, and E_{elec} is the electronic energy. Then, the total energy is the sum of the electronic energy, E_{elec}, and the nuclear repulsion term, E_{nuc}.

$$E_{nuc} = \sum_{A=1}^{M}\sum_{B>A}^{M}\frac{Z_A Z_B}{R_{AB}}. \tag{2.5}$$

After invoking the Born-Oppenheimer approximation, Hartree-Fock theory was developed to solve the electronic Schrödinger equation. When a system is in the state ψ, the variational principle states that the energy calculated from a guessed ψ is an upper bound to the ground state energy. Hence, the energy minimization by varying the parameters of wave function allows us to obtain better approximation of wave function, ψ. For many electrons problem, the wave function can be

represented by a Slater determinant.

$$\psi = \frac{1}{\sqrt{N!}} \begin{vmatrix} \psi_1(\vec{x}_1) & \psi_2(\vec{x}_1) & \ldots & \psi_N(\vec{x}_1) \\ \psi_1(\vec{x}_2) & \psi_2(\vec{x}_2) & \ldots & \psi_N(\vec{x}_2) \\ \vdots & \vdots & & \vdots \\ \psi_1(\vec{x}_N) & \psi_2(\vec{x}_N) & \ldots & \psi_N(\vec{x}_N) \end{vmatrix}. \tag{2.6}$$

The wave function, ψ, contains the full information of a system, and the Schrödinger equation is successfully validated for systems like H and H_2. However, ψ is a very complicated quantity that cannot be solve many-electron problem. So much progress has been made to find approximate solutions for many-electron problem. In 1927, shortly after the introduction of the Schrödinger equation, the Thomas-Fermi model is developed, which is a quantum mechanical theory for the electronic structure of many-body systems [25, 26]. In this model, the electron density plays a central role to avoid the complication of searching for the many-electron wave function. For a system with N particles, the electron density, $\rho(\vec{r})$, is defined as follow:

$$\rho(\vec{r}) = \int \ldots \int |\psi(\vec{x}_1, \vec{x}_2, \ldots, \vec{x}_N)|^2 d\vec{x}_1 d\vec{x}_2 \ldots d\vec{x}_N. \tag{2.7}$$

According to the Thomas-Fermi model, the kinetic energy, and potential energies can be expressed as follows:

$$T[\rho(\vec{r})] = \frac{3}{10}(r\pi^2)^{2/3} \int \rho^{(5/3)}(\vec{r}) d\vec{r}, \tag{2.8}$$

$$U_{eN} = -Z \int \frac{\rho(\vec{r})}{r} d\vec{r}, \tag{2.9}$$

$$U_{ee} = \frac{1}{2} \int \int \frac{\rho(\vec{r}_1)\rho(\vec{r}_2)}{r_{12}} d\vec{r}_1 d\vec{r}_2, \tag{2.10}$$

where T is the kinetic energy of electrons, U_{eN} is the attractive potential energy due to the interaction between electrons and nuclei, and U_{ee} is the repulsive potential energy due to the electron-

electron interactions. Finally the energy obtained in terms of the electron density is:

$$E[\rho(\overrightarrow{r})] = \frac{3}{10}(r\pi^2)^{2/3}\int \rho^{(5/3)}(\overrightarrow{r})d\overrightarrow{r} - Z\int \frac{\rho(\overrightarrow{r})}{r}d\overrightarrow{r} + \frac{1}{2}\int\int \frac{\rho(\overrightarrow{r}_1)\rho(\overrightarrow{r}_2)}{r_{12}}d\overrightarrow{r}_1 d\overrightarrow{r}_2.$$

(2.11)

In 1964, the Hohenberg-Kohn theorem confirms that the Thomas-Fermi model is correct [27]. The first Hohenberg-Kohn theorem demonstrates that the external potential $V_{ext}(\overrightarrow{r})$ is uniquely determined by the electron density, $\rho(r)$. Assuming that within a given same $\rho(r)$ for its ground state, there were two different external potential $V_{ext}(\overrightarrow{r})$ and $V'_{ext}(\overrightarrow{r})$. There would exist two different Hamiltonians $\hat{H}$ and $\hat{H}'$, ground state energies E and E' with two different wave functions ψ and ψ'. Taking ψ' as a trial wave function for the $\hat{H}$ problem

$$E_0 < \langle\psi'|\hat{H}|\psi'\rangle = \langle\psi'|\hat{H}'|\psi'\rangle + \langle\psi'|\hat{H}-\hat{H}'|\psi'\rangle = E'_0 + \int \rho(\overrightarrow{r})[V_{ext}(\overrightarrow{r})-V'_{ext}(\overrightarrow{r})]d\overrightarrow{r}. \quad (2.12)$$

Similarly, taking ψ as a trial wave function for the $\hat{H}'$ problem

$$E'_0 < \langle\psi|\hat{H}'|\psi\rangle = \langle\psi|\hat{H}|\psi\rangle + \langle\psi|\hat{H}'-\hat{H}|\psi\rangle = E_0 + \int \rho(\overrightarrow{r})[V'_{ext}(\overrightarrow{r})-V_{ext}(\overrightarrow{r})]d\overrightarrow{r}. \quad (2.13)$$

Now addition of Eq. 12 and 13 leads to inconsistency

$$E_0 + E'_0 < E'_0 + E_0. \tag{2.14}$$

Thus V_{ext} is a unique functional of $\rho(\overrightarrow{r})$. Since V_{ext} fixes H, in turn, the many-body ground state is a unique functional of $\rho(\overrightarrow{r})$. Hohenberg and Kohn applied variational principles on the energy functional, and the second Hohenberg-Kohn theorem states that the ground state density delivers the lowest energy.

$$E_0 \leq E[\tilde{\rho}] = T[\tilde{\rho}] + E_{eN}[\tilde{\rho}] + E_{ee}[\tilde{\rho}]. \tag{2.15}$$

For any trial density $\tilde{\rho}$, which satisfies the necessary boundary conditions such as $\tilde{\rho} \geq 0$, $\int \tilde{\rho}(\overrightarrow{r})d\overrightarrow{r} = N$, the energy associated with some external potential $\tilde{V}_{ext}$ represents an upper bound to the ground

state energy E_0. In 1964, Kohn-Sham equations are named after Walter Kohn and Lu Jeu Sham, and they introduced a concept of separating unknown many-body interacting energies from the rest, which is so called exchange-correlation energy [28]. The ground-state energy can be written in the form of

$$E = V_{ext}[\overrightarrow{\rho}] + J[\overrightarrow{\rho}] + T_s[\overrightarrow{\rho}] + E_{XC}[\overrightarrow{\rho}], \tag{2.16}$$

where $V_{ext}[\overrightarrow{\rho}]$ is the potential energy from the external field due to positively charged nuclei.

$$V_{ext}[\overrightarrow{\rho}] = \int \rho(\overrightarrow{r})V_{Ne}d\overrightarrow{r}. \tag{2.17}$$

$J[\overrightarrow{\rho}]$ is the classical Coulomb potential due to the electron-electron interactions.

$$J[\overrightarrow{\rho}] = \frac{1}{2} \int \int \frac{\rho(\overrightarrow{r}_1)\rho(\overrightarrow{r}_2)}{|\overrightarrow{r}_1 - \overrightarrow{r}_2|}d\overrightarrow{r}_1 d\overrightarrow{r}_2. \tag{2.18}$$

$T_s[\overrightarrow{\rho}]$ is the kinetic energy of a system of non-interacting electrons.

$$T_s[\rho(\overrightarrow{r})] = -\frac{1}{2}\sum_i^N \langle\psi_i|\nabla^2|\psi_i\rangle. \tag{2.19}$$

E_{XC} is the so-called exchange-correlation energy, which is defined as $E_{XC} = T - T_0 + U - J$. If we know the exact form of E_{XC}, the Kohn-Sham equation would lead to the exact ground-state energy of system. However, the exact functionals for exchange and correlation are not known. There exists a number of approximations to estimate exchange-correlation potentials. The local density approximations (LDA) are approximations to the exchange-correlation energy functional in the form of [29]:

$$E_{XC}^{LSD}[n_\uparrow, n_\downarrow] = \int n(r)\epsilon_{XC}(n_\uparrow(r), n_\downarrow(r))d^3r, \tag{2.20}$$

where $\epsilon_{XC}(n_\uparrow(r), n_\downarrow(r))$ is the known exchange-correlation energy per particle with uniform spin densities, $n_\uparrow, n_\downarrow, n = n_\uparrow + n_\downarrow$ [30]. Further $\epsilon_{XC}(n_\uparrow(r), n_\downarrow(r))$ can be split into exchange and

correlation contributions.

$$\epsilon_{XC}(n_\uparrow(r), n_\downarrow(r)) = \epsilon_X(n_\uparrow(r), n_\downarrow(r)) + \epsilon_C(\rho(n_\uparrow(r), n_\downarrow(r)). \tag{2.21}$$

Local density approximations are clearly valid when the spin densities vary slowly, but it fails where the densities undergo rapid changes. An improvement to LDA can be made by considering the gradient of charge densities, $\nabla_\uparrow(r)$ and $\nabla_\uparrow(r)$. Thus, the exchange-correlation energy so-called generalized gradient approximations (GGA) can be written as:

$$E_{XC}^{GGA} = \int f(n_\uparrow, n_\downarrow, \nabla n_\uparrow, \nabla n_\uparrow)d^3r. \tag{2.22}$$

In this study, the total energy calculations were carried out through the Density Functional Theory (DFT) [28], which is implemented in the Vienna Ab-initio Simulation Package (VASP) [31, 32]. VASP uses a plane wave basis set, and calculate the forces acting on ions using Hellmann-Feynman theorem [33]. The interaction between ions and electrons is described by the projector augmented-wave method [34]. The Generalized Gradient Approximation (GGA) is used for the exchange correlation, and the Perdew-Burke-Ernzerhof (PBE) is the simplified version of the GGA.

2.3 Special Quasirandom Structures (SQS)

The fully disordered crystalline alloys have to be obtained to investigate the solid solution of MAX phases with tunable properties. The SQS is known as the best periodic supercell approximation for a given number of atoms per supercell. In this study, the "mcsqs" code is used to generate SQS structures, which is implemented in the Alloy Theoretic Automated Toolkit (ATAT) [35]. The SQS generation algorithm is based on Monte Carlo simulated annealing relaxation of candidate configurations, with the objective of matching the largest number of random correlation functions derived from occupancies of different sites within a given symmetrically unique cluster:

$$\rho_\alpha(\sigma) = \langle \Gamma_{\alpha'}(\sigma) \rangle_\alpha, \tag{2.23}$$

9

where the σ, $\sigma_i = 0,\ldots, M_{i-1}$, denotes chemical species that occupy site i, the α, $\alpha_i = 0,\ldots, M_{i-1}$, considers particular correlation called cluster, and $\langle \Gamma_{\alpha'}(\sigma) \rangle$ is a cluster function, defined as

$$\langle \Gamma_{\alpha'}(\sigma) \rangle = \Pi \gamma_{\alpha_i, M_i}(\sigma_i). \tag{2.24}$$

Details of the approach can be found in Walle et al [35]. In this work, the SQS were generated to study $Ti_3(Si_xAl_{1-x})C_2$ solid solutions, where x corresponds to 0.25, 0.5 and 0.75.

2.4 Elastic Properties

The elastic constants were estimated by stress-strain approach [36, 37, 38]. $\bar{A}$ is the deformed lattice vectors when a set of strains ($\varepsilon = \varepsilon_1 - \varepsilon_6$) is applied to A, which is lattice vectors prior to the deformation.

$$\bar{A} = A \begin{vmatrix} 1 + \varepsilon_1 & \frac{\varepsilon_6}{2} & \frac{\varepsilon_5}{2} \\ \frac{\varepsilon_6}{2} & 1 + \varepsilon_2 & \frac{\varepsilon_4}{2} \\ \frac{\varepsilon_5}{2} & \frac{\varepsilon_4}{2} & 1 + \varepsilon_3 \end{vmatrix}. \tag{2.25}$$

A set of stresses ($\sigma = \sigma_1 - \sigma_6$) is calculated using the DFT methods, and the elastic constants were calculated using Hooke's law from n set of strains and the resulting stresses as shown below.

$$\begin{vmatrix} C_{11} & \cdots & C_{16} \\ \vdots & & \vdots \\ C_{61} & \cdots & C_{66} \end{vmatrix} = \begin{vmatrix} \varepsilon_{1,1} & \cdots & \varepsilon_{1,n} \\ \vdots & & \vdots \\ \varepsilon_{6,1} & \cdots & \varepsilon_{6,n} \end{vmatrix}^{-1} \begin{vmatrix} \sigma_{1,1} & \cdots & \sigma_{1,n} \\ \vdots & & \vdots \\ \sigma_{6,1} & \cdots & \sigma_{6,n} \end{vmatrix}. \tag{2.26}$$

The elastic moduli of hexagonal structures were estimated based on Voigt's approximation. A calculation of the bulk, shear and Young's modulus are shown as follows [39]:

$$B_V = \frac{2(C_{11} + C_{12}) + 4C_{13} + C_{33}}{9}, \tag{2.27}$$

$$G_V = \frac{M + 12C_{44} + 12C_{66}}{30}, \tag{2.28}$$

$$M = C_{11} + C_{12} + 2C_{33} - 4C_{13}, \tag{2.29}$$

$$E = \frac{9BG}{3B + G}, \tag{2.30}$$

where B is bulk modulus, G is shear modulus, E is Young's modulus.

2.5 Finite-temperature Properties

The finite-temperature thermodynamic properties can be derived from the total free energy of a system. For the total free energy calculation, we consider vibrational and electronic contributions and anharmonic correction. The vibrational contribution is obtained by the supercell method, which is implemented in the ATAT package [40]. A unit cell system is fully relaxed, then sets of supercells are generated with displacement. The forces on atoms are calculated, then compile all the forces into the so-called dynamical matrix. The dynamical matrix has eigenvalues (frequencies) of the normal modes of oscillation in the system, which allows to calculate phonon density of states (PDOS). The vibrational free energy is obtained from the PDOS through the statistical mechanics [41, 42]:

$$F_{vib}(V,T) = k_B T \int_0^\infty ln[2sinh(\frac{h\nu}{2k_B T})]g(\nu)|_V d\nu, \tag{2.31}$$

where k_B is Boltzmann's constant, h is Planck's constant, T is temperature, V is the quasi-harmonic volume, ν is the frequency and $g(\nu)|_V$ is the phonon density of states of the structure corresponding to V.

The electronic degrees of freedom affect to the total free energy of a system. The electronic density of states, $n(\varepsilon)$, and the Fermi function, f, are related to the free energy of electrons by the statistical physics as follows:

$$F_{el}(V,T) = E_{el}(V,T) - TS_{el}(V,T). \tag{2.32}$$

$$E_{el}(V,T) = \int n(\varepsilon)|_V f\varepsilon d\varepsilon - \int^{\varepsilon_F} n(\varepsilon)|_V \varepsilon d\varepsilon. \tag{2.33}$$

$$S_{el}(V,T) = -k_B \int n(\varepsilon)|_V [flnf + (1-f)ln(1-f)]d\varepsilon. \tag{2.34}$$

Wallace developed the anharmonic free energy equation, which is related to the expansion of the crystal potential.

$$F_{anhar} = A_2 T^2 + A_0 + A_{-2}T^{-2} + L. \tag{2.35}$$

$$A_2 = \frac{3k_B}{\Theta}(0.0078 < \gamma > -0.0154). \tag{2.36}$$

The Gruneisen parameter, γ, and the coefficients are based on an empirical data. The anharmonic free energy is only reasonable in the high temperature region since they ignore the last three terms, which cannot be easily determined. Then, Oganov developed the anharmonic free energy, and extended it to all temperature region. Using themodynamic perturbation theory he obtained an expression for the anharmonic free energy as a function of temperature:

$$\frac{F_{anhar}}{3nk_B} = \frac{a}{6}[(\frac{1}{2}\theta + \frac{\theta}{exp(\theta/T) - 1})^2 + 2(\frac{\theta}{T})^2 \frac{exp(\theta/T)}{(exp(\theta/T) - 1)^2}T^2], \tag{2.37}$$

where a is $1/2A_2$ and θ corresponds to the high temperature Harmonic Debye temperature, defined as $\theta = \frac{\bar{h}}{k_B}(\frac{5}{3} < \omega^2 >)^{\frac{1}{2}}$.

The total free energy of the system is the summation of the aforementioned energy terms:

$$F_{total}(V,T) = E_{0K}(V) + F_{vib}(V,T) + F_{el}(V,T) + F_{anhar}(V,T), \tag{2.38}$$

where $E_{0K}(V)$ is the zero-temperature energy at each quasi-harmonic volume. Thermodynamic properties can be calculated using the total free energy:

$$S = -\frac{\partial F(T)}{\partial T}, C_P = T\frac{\partial S}{\partial T}. \tag{2.39}$$

2.6   Cleavage Energy

High strength and good ductility are important properties of materials. The strength of materials is that how much stress a material can sustain. Ideally, the strength in a single crystal without any defects is determined solely by the chemical bonding strength between neighboring atoms. To

12

(a) z=0   (b) z=1   (c) z=2   (d) z=3
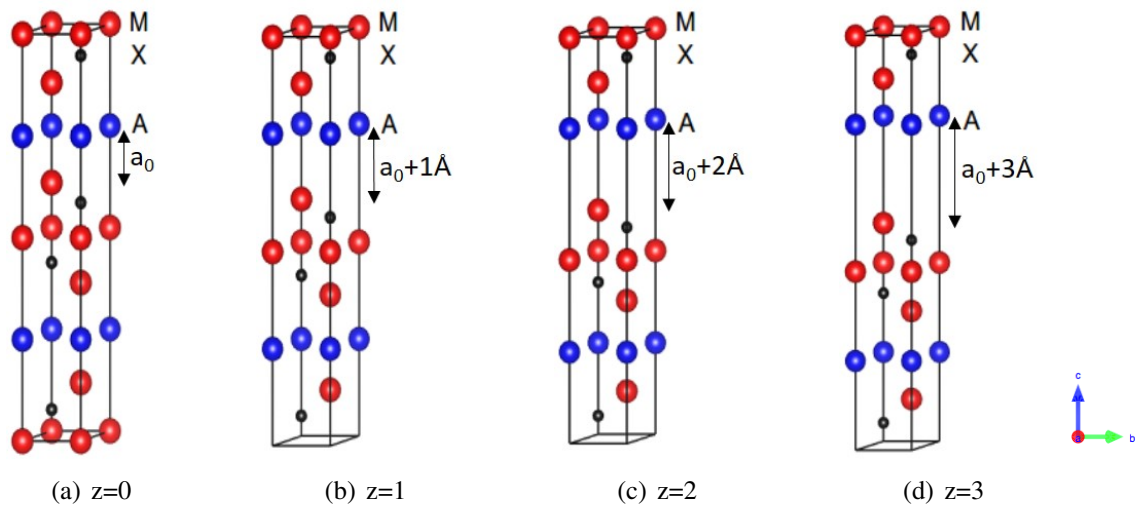
Figure 2.1: Cleavage between M and A layer under loading mode I. The cleavage distance z (Å) for (a), (b), (c) and (d) is 0, 1, 2 and 3, respectively. Reprinted with permission from [1].

(a)   (b)   (c)   (d)   (e)
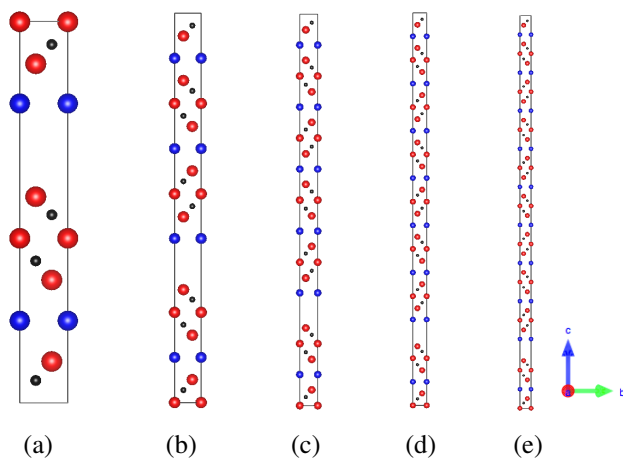
Figure 2.2: Cleavage between M and A layer under loading mode I. The (a), (b), (c), (d), and (e) systems have 1, 2, 3, 4, and 5 unit cells, respectively, with one single cleavage surface. Reprinted with permission from [1].

study the strength of a material, we study the cleavage behavior based on density functional theory under loading mode I [43] as shown in Fig. 2.1. In this model, two slabs are separated for the generation of crack. In particular, M and A layers are cleaved since M-A bond is known as relatively weaker than M-X bond. Then systems are fully relaxed while fixing the atoms on cleavage planes to avoid additional internal stresses, which do not correspond to the cleavage deformation. The cleavage energy at every separation level was calculated through DFT as follows:

$$\Delta E/A = E(z)/A - E(0)/A, \tag{2.40}$$

where z is the cleavage distance between M and A layers. The stress $\sigma(z)$ is defined by the first derivative,

$$\sigma(z) = \left(\frac{dE}{dz}\right). \tag{2.41}$$

The critical stress, σ_c, is the maximum value of the cleavage stress, σ_c=max[$\sigma(z)$], under the cleavage deformation. The critical stress is the required tensile stress to cut the M-A bonds, which are atomic bonds between the given two cleavage planes. For the validation of the cleavage model, we considered internal stresses in the unit cell, and out of the unit cell. First, to consider internal stresses in the unit cell, we studied the elastic response of neighboring regions in the unit cell. We consider a so-called ideal brittle cleavage, in addition to the relaxation scheme described above. The ideal brittle cleavage is considered by cleaving M-A layer along the c direction, without allowing any relaxation. The cleavage energy and stress of the ideal brittle model are compared to those of the relaxation model to study the effect of elastic relaxation on cleavage energy, as the latter consists of two parts: the atomic de-cohesion energy and the strain energy released in the crystal on either side of the cleavage surface. Second, to consider internal stresses out of the unit cell, we generated systems with 1,2,3,4, and 5 unit cells containing one single cleavage surface, as shown in Fig. 2.2. Each of the systems with different numbers of unit cells was cleaved along c direction, then relaxation is followed with atoms not belonging to the cleavage surfaces. The cleavage energy and stress are calculated by equation 40 and 41 to study the effect of the system size.
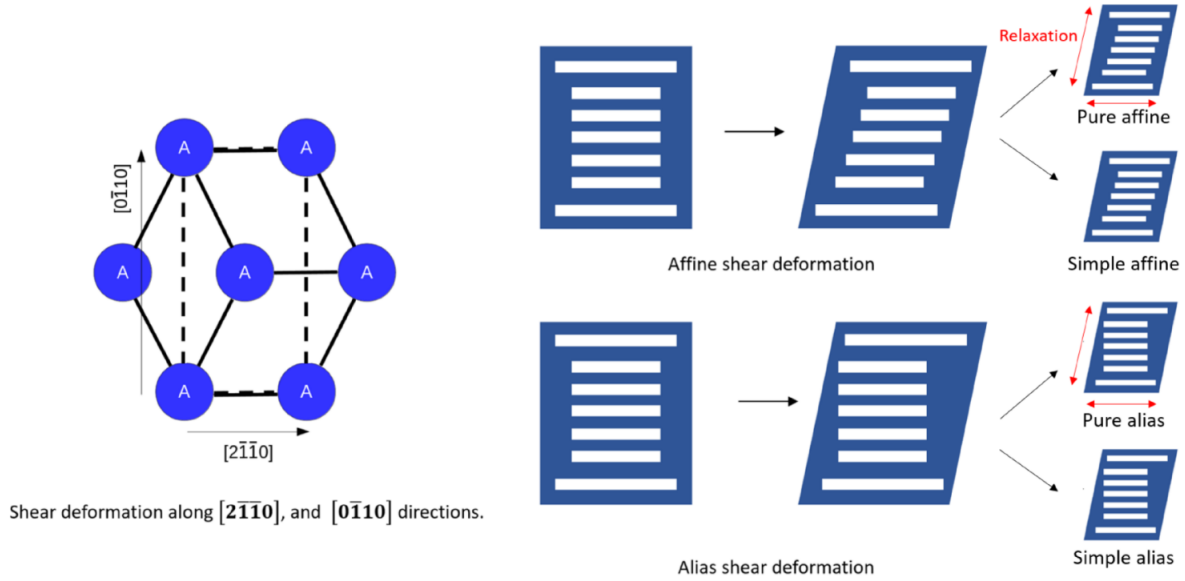
Figure 2.3: The orthorhombic super cell (dashed line) and schematic view of pure affine, simple affine, pure alias, and simple alias shear deformations. Reprinted with permission from [1].

2.7 Stacking Fault Energy (SFE)

Generally, the ductility of a material is related to the plastic deformation, which is controlled by the movement of dislocations. An edge dislocation model can be produced by shearing crystal half a lattice and carefully joining planes together. A dislocation is characterized by a Burgers vector, which is a connection of starting and end points of a path defined by a series of lattice vectors in a region where a line defect could exist. For an edge dislocation, The Burgers vector is perpendicular to the dislocation line. Ab initio density functional calculations have been used to study the response of MAX phases to shearing. The MAX phases are layered hexagonal structure, and the most active slip system of hexagonal close packed structure is $\langle 2\bar{1}\bar{1}0 \rangle \{0001\}$ slip system, which describes direction and close-packed plane. The magnitude and direction of slip is described by the Burgers vector, b = 1/3 $\langle 2\bar{1}\bar{1}0 \rangle \{0001\}$. This dislocation can be separated into two partial dislocations $\langle 1\bar{1}00 \rangle \{0001\}$ and $\langle 10\bar{1}0 \rangle \{0001\}$, which are identical to $\langle 0\bar{1}10 \rangle \{0001\}$. We present resultant energy curves for both of the $\langle 2\bar{1}\bar{1}0 \rangle \{0001\}$ and $\langle 0\bar{1}10 \rangle \{0001\}$ shear deformations.

The orthorhombic supercell has generated to study shear deformations of hexagonal close

15

packed (HCP) system of Ti_3AlC_2, $Ti_3(Al_{0.5}Si_{0.5})C_2$, Ti_3SiC_2 as shown in Fig. 2.3. The basal plane of the orthorhombic system is parallel to the basal plane of hcp system. The a, b, and c lattice vectors of the orthorhombic system is parallel to the $\langle 2\bar{1}\bar{1}0 \rangle$, $\langle 0\bar{1}10 \rangle$, and $\langle 0001 \rangle$ of hcp system. In this work, we study the shear deformation along the a and b lattice vectors of orthorhombic system. Alias and affine shear deformation are applied to the orthorhombic system to study the shear deformation [44]. Alias shear deformation displaces only the top most layer along the shear direction, while affine shear deformation proportionally displaces all atoms along shear direction. For both shear deformations, we considered simple and pure shear. Simple shear does not allow the system to relax any degree of freedoms at sheared system. On the other hand, pure shear fully relaxes sheared system, while only fixing the angle of shear to vanish all internal stresses do not correspond to the shear deformation process. For the pure shear deformation we used the external optimizer GADGET developed by Bucko et al. [45], since VASP does not allowed to carry on relaxations under arbitrary constraints.

3. STRUCTURAL, ELECTRONIC, MECHANICAL AND THERMODYNAMIC PROPERTIES OF Ti_3AlC_2, Ti_3SiC_2, AND $Ti_3(Si_xAl_{1-x})C_2$

3.1 Structural and Electronic Properties

The $Ti_3(Si_xAl_{1-x})C_2$ systems form into nano-layered hexagonal structures, and the optimized structures are shown in Fig. 3.1, visualized using VESTA. The stability of $Ti_3Si_xAl_{1-x}C_2$ is considered through the calculation of formation enthalpy ΔH as given by:

$$\Delta H(Ti_3(Si_xAl_{1-x})C_2) = E(Ti_3(Si_xAl_{1-x})C_2) - nE(Ti) - nE(xSi) - nE((1-x)Al) - nE(C),$$

$$(3.1)$$

where E is the total energy per atom, n is a fraction of element in $Ti_3(Si_xAl_{1-x})C_2$ system, and x is a fraction of silicon in $Ti_3(Si_xAl_{1-x})C_2$ system. The calculated formation enthalpies of $Ti_3(Si_xAl_{1-x})C_2$ with x= 0, 0.25, 0.5, 0.75, and 1 are -0.812, -0.826, -0.838, -0.849, -0.861, respectively in the unit of eV/atom.

The resultant a- and c- lattice parameters, and their experimental results [2] are shown in Fig. 3.2(a). Both of calculated and experimental results show that the a-lattice parameter is almost constant around the value of 3 , and the c-lattice parameter is decreasing from around 18.5 to

(a) z=0   (b) z=1   (c) z=2   (d) z=3   (e) z=3
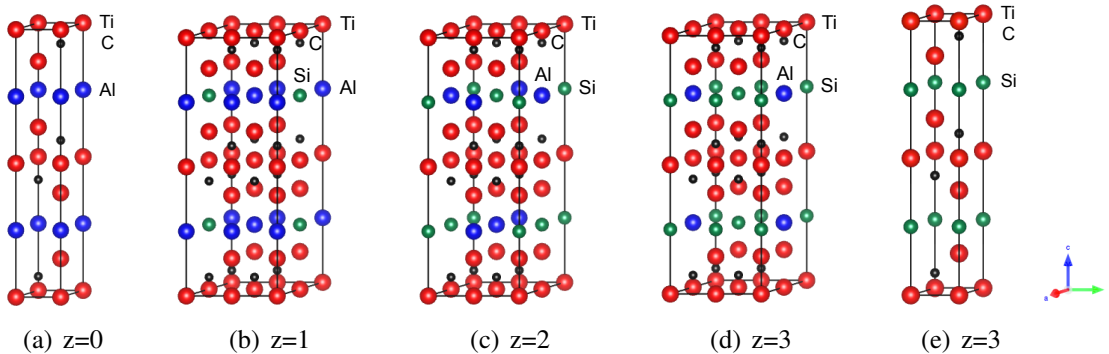
Figure 3.1: Crystal structure of the $Ti_3Si_xAl_{1-x}C_2$ with (a) x=0, (b) x=0.25, (c) x=0.5, (d) x=0.75, and (e) x=1. Reprinted with permission from [1].

(a) Lattice parameters   (b) Bond length
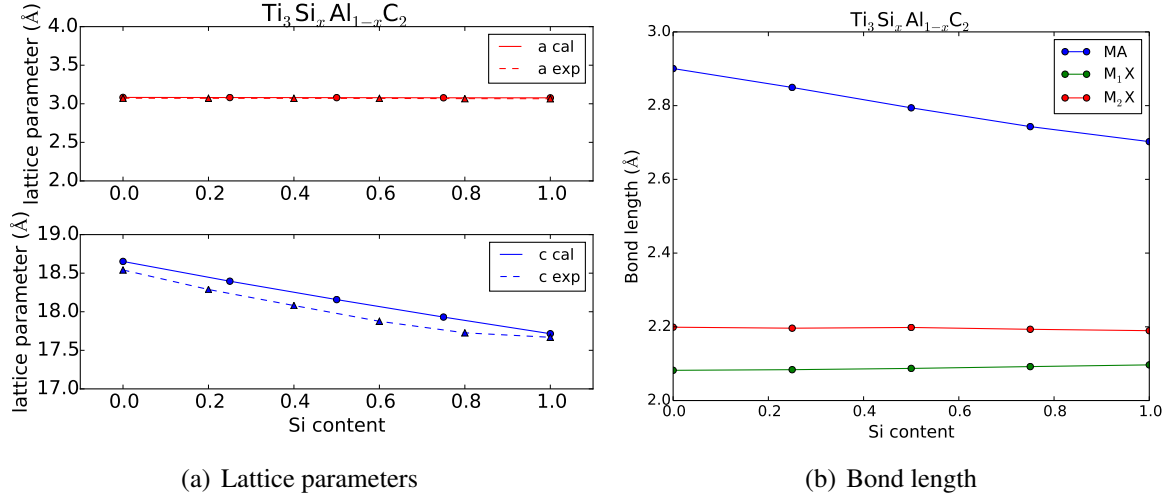
Figure 3.2: (a) The a- and c-lattice parameter as a function of Si composition, the solid lines represent the calculated data using DFT while the dash lines are the experimental data retrieved from XRD [2]. (b) Bond length of M-A, M_1-X, and M_2-X, where M_1 is a M element near the A element, and M_2 is a M element far from the A element. Reprinted with permission from [1].

17.5 with increasing amount of Si. The M-A, M_1-X, and M_2-X bond lengths are shown in Fig. 3.2(b). Both M_1-X, and M_2-X bond lengths are almost constant, while M-A bond length is decreasing with increasing amount of Si. Since MAX phases are layered materials, the decreasing c-lattice parameter with increasing amount of Si can be explained by decreasing M-A bond length, which is atomic bond along the c-lattice direction. The substitution of Al with Si makes the M-A bonds stronger so that the M-A bond length and c-lattice parameters are decreasing. The analysis of Electron Localization Function (ELF), charge densities and electronic density of states (EDOS) are carried out to demonstrate the bond strengths.

Fig. 3.3 corresponds to a 2-dimensional representation of (100) plane of the ELF for $Ti_3Si_xAl_{1-x}C_2$ systems. The ELF represents the sum of the number of electrons. ELF is suitable for the observation of electrons in real space, which corresponds to chemical bonding of each atom, and it is scaled between zero and one. As can be seen from the figure, distributions of electrons between M-A and A-X bonds are getting higher and higher with increasing Si-content.

The (100) plane view of the charge density of $Ti_3(Si_xAl_{1-x})C_2$ is shown in Fig. 3.4, which is

18
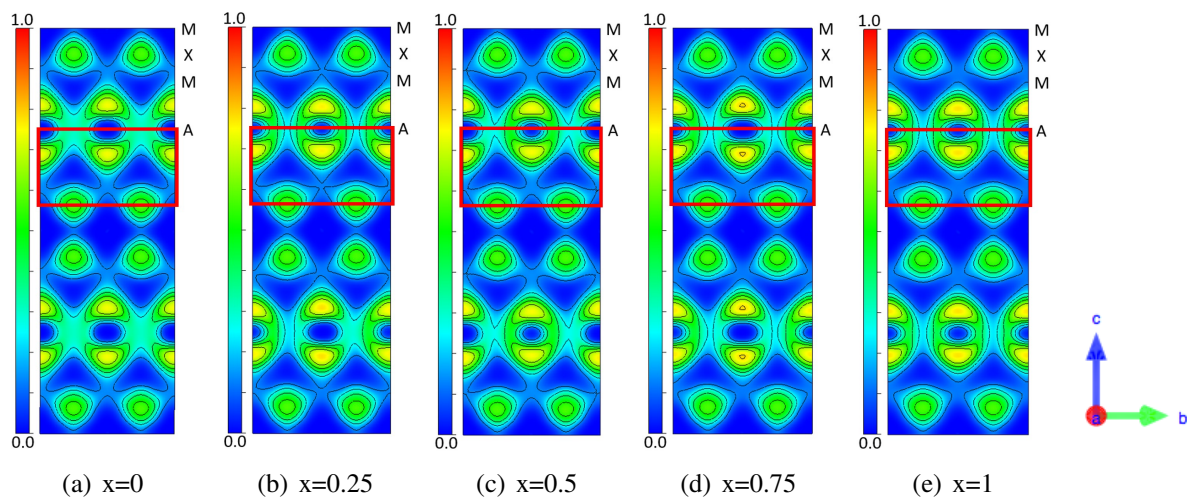
Figure 3.3: (100) Plane view of Electron Localization Function (ELF) of the $Ti_3(Si_xAl_{1-x})C_2$ with (a) x=0, (b) x=0.25, (c) x=0.5, (d) x=0.75, and (e) x=1. Reprinted with permission from [1].
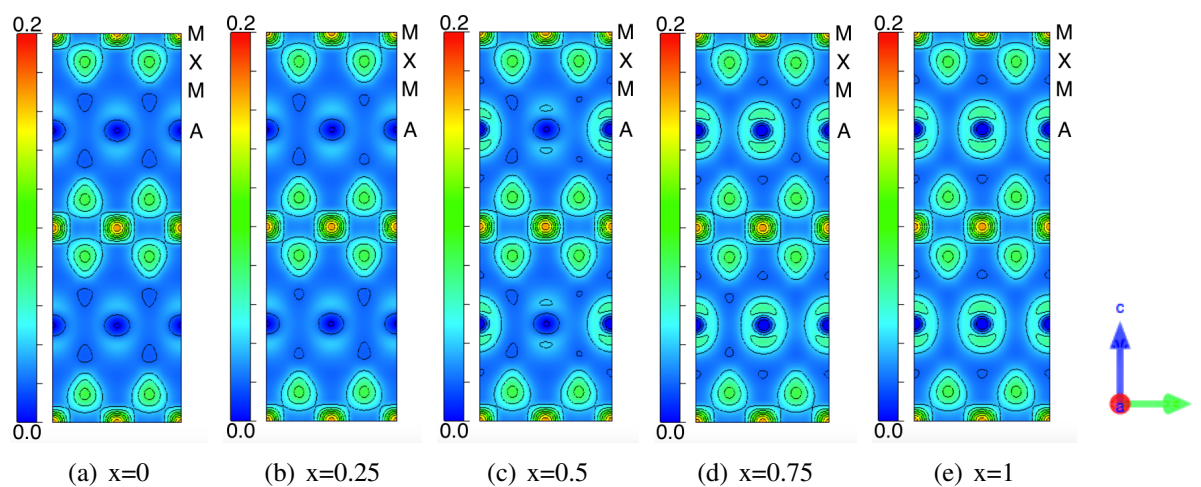
Figure 3.4: (100) Plane view of charge density of the $Ti_3Si_xAl_{1-x}C_2$ with (a) x=0, (b) x=0.25, (c) x=0.5, (d) x=0.75, and (e) x=1. Reprinted with permission from [1].

Phase	Ti$_3$AlC$_2$	Ti$_3$Si$_{0.25}$Al$_{0.75}$C$_2$	Ti$_3$Si$_{0.5}$Al$_{0.5}$C$_2$	Ti$_3$Si$_{0.75}$Al$_{0.25}$C$_2$	Ti$_3$SiC$_2$
Ti (d3s1)	1.905 (-2.095)	1.896 (-2.104)	1.890 (-2.11)	1.885 (-2.115)	1.883 (-2.117)
Al (s2p1)	4.156 (+1.156)	4.093 (+1.093)	4.008 (+1.008)	3.826 (+0.826)	
Si (s2p2)		5.573 (+1.573)	5.539 (+1.539)	5.499 (+1.499)	5.378 (+1.378)
C (s2p2)	6.564 (+2.564)	6.550 (+2.550)	6.530 (+2.530)	6.507 (+2.507)	6.486 (+2.486)
Ti (total)	45.72	45.504	45.36	45.24	45.192
Al & Si (total)	33.248	35.704	38.188	40.646	43.024
C (total)	105.024	104.8	104.48	104.112	103.776

Table 3.1: The number of valence electrons (and charge transfer) is obtained by Bader analysis.

related to the bond strength. The charge density represents the absolute value of the charge, and the bright regions around atoms represent that atoms are highly charged negatively or positively. The high charge density of Si element compare to the Al element indicates that M-Si bonds are stronger than M-Al bonds.

The number of valence electrons and charge transfer is shown in Table 3.1, which is obtained by the Bader analysis. In Ti$_3$(Si$_x$Al$_{1-x}$)C$_2$ systems, Ti atoms are positively charged and the total charge density of Ti changes from 45.72 to 45.192. C atoms are negatively charged and the total charge density changes from 105.02 to 103.77. Both Ti and C total charge density are almost constant with different amount of Si. However, the total charge density of negatively charged Al and Si changes from 33.25 to 43.02. The increasing charge density of Al and Si means that the M-A bonds get stronger with increasing amount of Si. This analysis demonstrates that M-A bond strength is increasing and the c-lattice parameter is decreasing with increasing amount of Si.

The total and atom-projected electron density of states (EDOS) of Ti$_3$(Si$_x$Al$_{1-x}$)C$_2$ are shown in Fig. 3.5. The total EDOS of Ti$_3$(Si$_x$Al$_{1-x}$)C$_2$ shows that Ti mostly contributes to the EDOS at Fermi level, and atom-projected EDOS shows that it is mostly d-electrons. The electrical con-

(a) Ti$_3$AlC$_2$

(b) Ti$_3$(Si$_{0.25}$Al$_{0.75}$)C$_2$

(c) Ti$_3$(Si$_{0.5}$Al$_{0.5}$)C$_2$

(d) Ti$_3$(Si$_{0.75}$Al$_{0.25}$)C$_2$
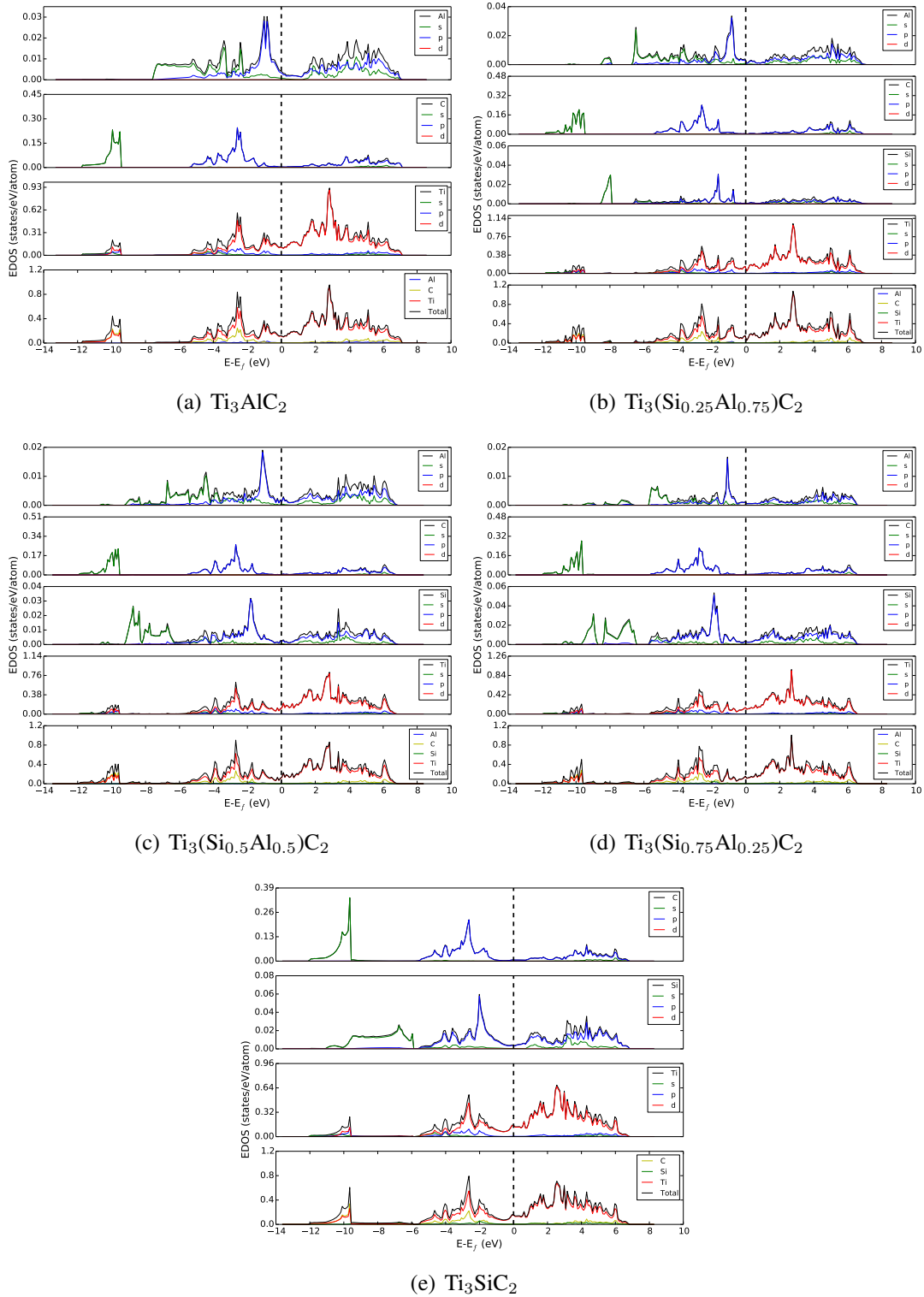
(e) Ti$_3$SiC$_2$

Figure 3.5: Calculated electronic density of states (EDOS) for (a) Ti$_3$AlC$_2$, (b) Ti$_3$(Si$_{0.25}$Al$_{0.75}$)C$_2$, (c) Ti$_3$(Si$_{0.5}$Al$_{0.5}$)C$_2$, (d) Ti$_3$(Si$_{0.75}$Al$_{0.25}$)C$_2$, and (e) Ti$_3$SiC$_2$. The bottom panel indicates total and atom-projected DOS. The upper panels indicate site-projected DOS. The dashed line indicates the Fermi level. Reprinted with permission from [1].
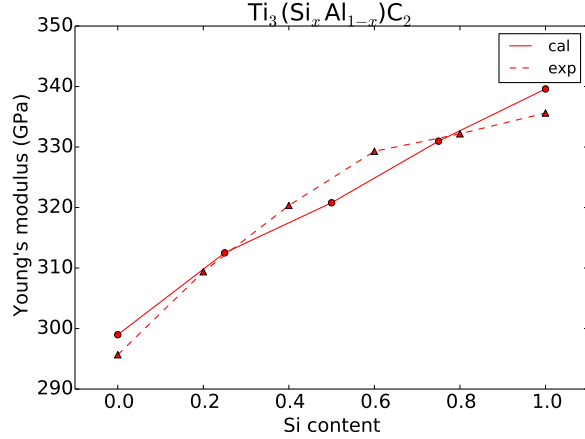
Figure 3.6: Comparison of Young's modulus obtained by DFT calculations (cal.) and RUS measurements (exp.). Reprinted with permission from [1].

ductivity comes from the EDOS of titanium's d-electrons. Moreover, the peak around -2.5 eV of atom-projected EDOS shows that p-C and d-Ti electrons are hybridized, the peak around -2.0 eV shows that p-Si and d-Ti electrons are hybridized, and the peak around -1.0 eV shows that p-Al and d-Ti electrons are hybridized. This analysis shows that M-X bond is stronger than M-A bond, and it supports that why we need to focus on A layer for the cleavage and shear behaviors in the following sections.

3.2 Elastic Properties

Under the ground state condition, the elastic constants were calculated by the stress-strain approach based on DFT, then the bulk (B), shear (G), and Young's (E) modulus were estimated using Voigt's approximation. The calculated and experimental Young's modulus agree well and shown in Fig. 3.6. All the calculated elastic constants and modulus are shown in Table 3.2. It shows that B, G, and E are increasing with increasing amount of Si. Again it could be attributed to the charge density shown in Table 3.1. In particular, the substitution of Al with Si increases the total charge density of the A element atoms from 33.25 to 43.02. However, the total charge density of M and X element atoms does not change significantly. The increased charge density makes the M-A bonds stronger, and thus harder to stretch. Moreover, in the $Ti_3(Si_xAl_{1-x})C_2$ system, C_{11}

22

Phase	C_{11}	C_{33}	C_{44}	C_{12}	C_{13}	B	G	E
Ti_3AlC_2	355.45	292.89	119.03	84.63	76.03	163.02	125.17	298.98
$Ti_3Si_{0.25}Al_{0.75}C_2$	362.45	304.47	128.30	85.75	82.73	170.20	130.87	312.51
$Ti_3Si_{0.5}Al_{0.5}C_2$	365.02	317.32	136.93	90.32	90.99	176.88	133.91	320.79
$Ti_3Si_{0.75}Al_{0.25}C_2$	368.92	334.66	145.89	93.85	99.62	184.30	137.82	330.97
Ti_3SiC_2	370.47	349.71	155.43	97.22	112.11	192.61	140.78	339.60

Table 3.2: Elastic constants, bulk modulus (B), shear modulus (G), and Young's modulus (E).

changes from 355.45 GPa to 370.47 GPa, and C_{33} changes from 292.89 GPa to 349.71 GPa. The large change of C_{33} could be related to the large change of c lattice parameter shown in Fig. 3.2.

3.3 Finite-temperature Properties

As mentioned above, the total free energy of a system can be obtained from the ground state energy, vibrational contribution, electronic contribution, and anharmonic correction, which is the energy as a function of temperature and volume. Then the energy as a function of temperature and pressure can be obtained through thermodynamic relationships.

$$G(T, p) = min[U(V) + F_{vib}(T; V) + pV], \qquad (3.2)$$

where V and p are the volume and pressure. It can be fitted to the integral form of the equation of state, and the bulk modulus of $Ti_3(Si_xAl_{1-x})C_2$ were obtained as shown in Fig. 3.7(a). From 0 K to 2000 K, the bulk modulus is increasing with increasing amount of Si, since the substitution of Al with Si makes the M-A bond stronger. Generally, the elastic modulus and thermal expansion are inversely related. However, as shown in Fig. 3.7(b), the coefficient of thermal expansion (CTE) of Ti_3SiC_2 is higher than that of Ti_3AlC_2. To address this phenomenon, the total and partial phonon density of states (PDOS) were studied as shown in Fig. 3.8. The PDOS of the Ti and C show
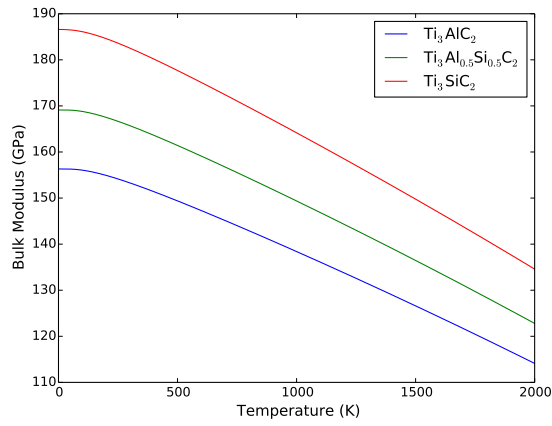
(a) Bulk modulus
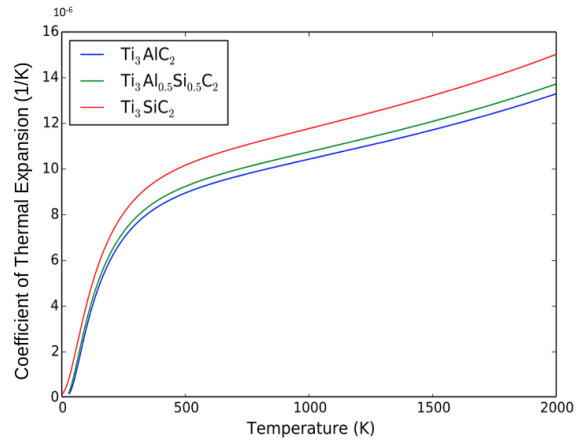
(b) Coefficient of Thermal Expansion

Figure 3.7: (a) The Bulk modulus, and (b) Coefficient of Thermal Expansion (CTE) of Ti_3AlC_2, Ti_3SiC_2, and $Ti_3(Si_{0.25}Al_{0.75})C_2$ as a function of temperature. Reprinted from [3].
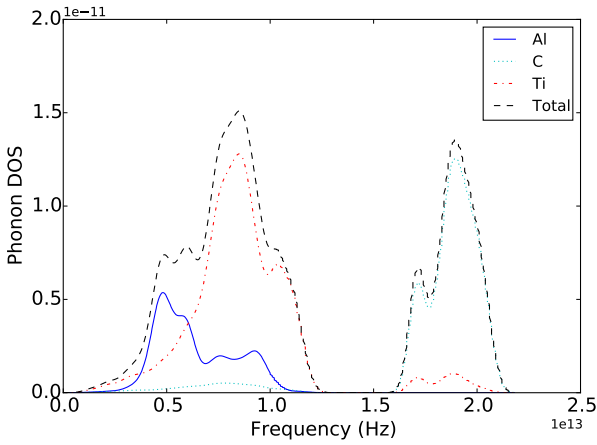
(a) Ti_3AlC_2
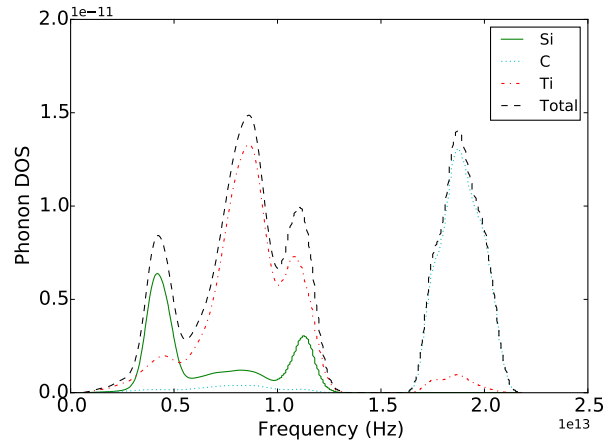
(b) Ti_3SiC_2

Figure 3.8: Total and partial Phonon Density of States (PDOS) of a) Ti_3AlC_2 and b) Ti_3SiC_2. The dashed, dashed-dotted, and dotted curves denote total, Ti, and C, respectively, and the solid line denotes Al and Si. Reprinted from [3].

(a) Free energy, F (b) Heat capacity, C_p
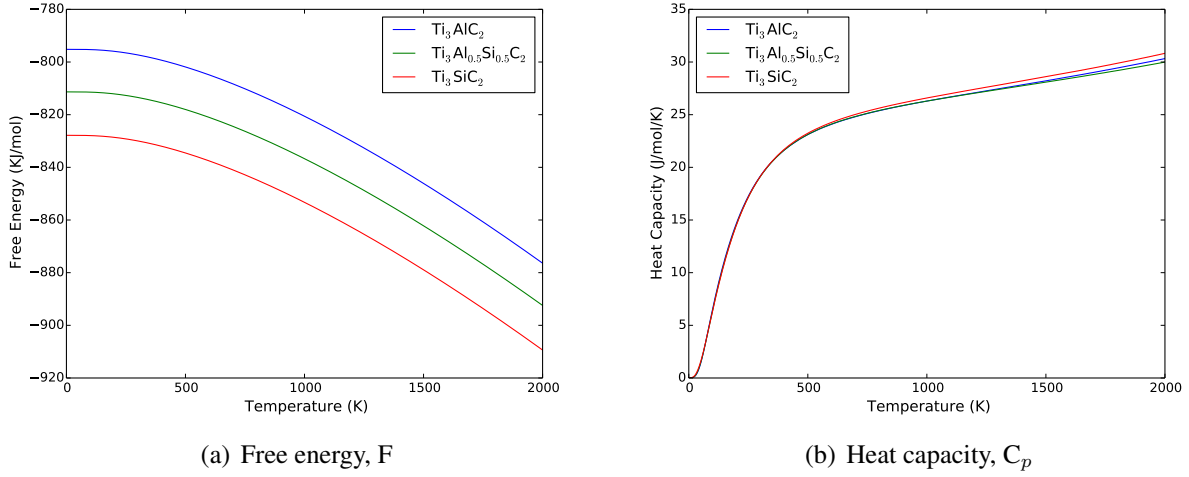
Figure 3.9: (a) Free energies, and (b) heat capacities of Ti_3AlC_2, Ti_3SiC_2, and $Ti_3(Si_{0.25}Al_{0.75})C_2$ as a function of temperature. Reprinted from [3].

similarity in both Ti_3AlC_2, and Ti_3SiC_2. However, the PDOS of Al and Si are different in acoustic region (under 15THz). The area under the PDOS curve of Al and Si are 3.89 and 6.40, respectively. The higher PDOS of the Si than the PDOS of the Al, in the acoustic region, addresses the higher CTE of Ti_3SiC_2 than the CTE of Ti_3AlC_2.

The calculated total free energy and heat capacity of $Ti_3(Si_xAl_{1-x})C_2$ are shown in Fig. 3.9. From 0 K to 2000 K, the total free energy is increasing with increasing amount of Al. However, the slopes are identical, since the vibrational, electronic, and anharmonic contributions of $Ti_3(Si_xAl_{1-x})C_2$ are equal. Hence, the heat capacity derived from the total energy are identical for $Ti_3(Si_xAl_{1-x})C_2$, which agree well with the experimented values of heat capacities by Gao et al.[2].

3.4 Cleavage Energy

We study the cleavage and shear behavior of $Ti_3(Si_xAl_{1-x})C_2$ alloys to study the mechanical behavior beyond the elastic region. This is to shed some light onto the experimental observations regarding the increase in hardness in the case of Si-contained MAX phases. The knowledge about cleavage and slip is also found to be of interest developing constitutive models aimed at predicting

(a) Cleavage energy

(b) Cleavage stress
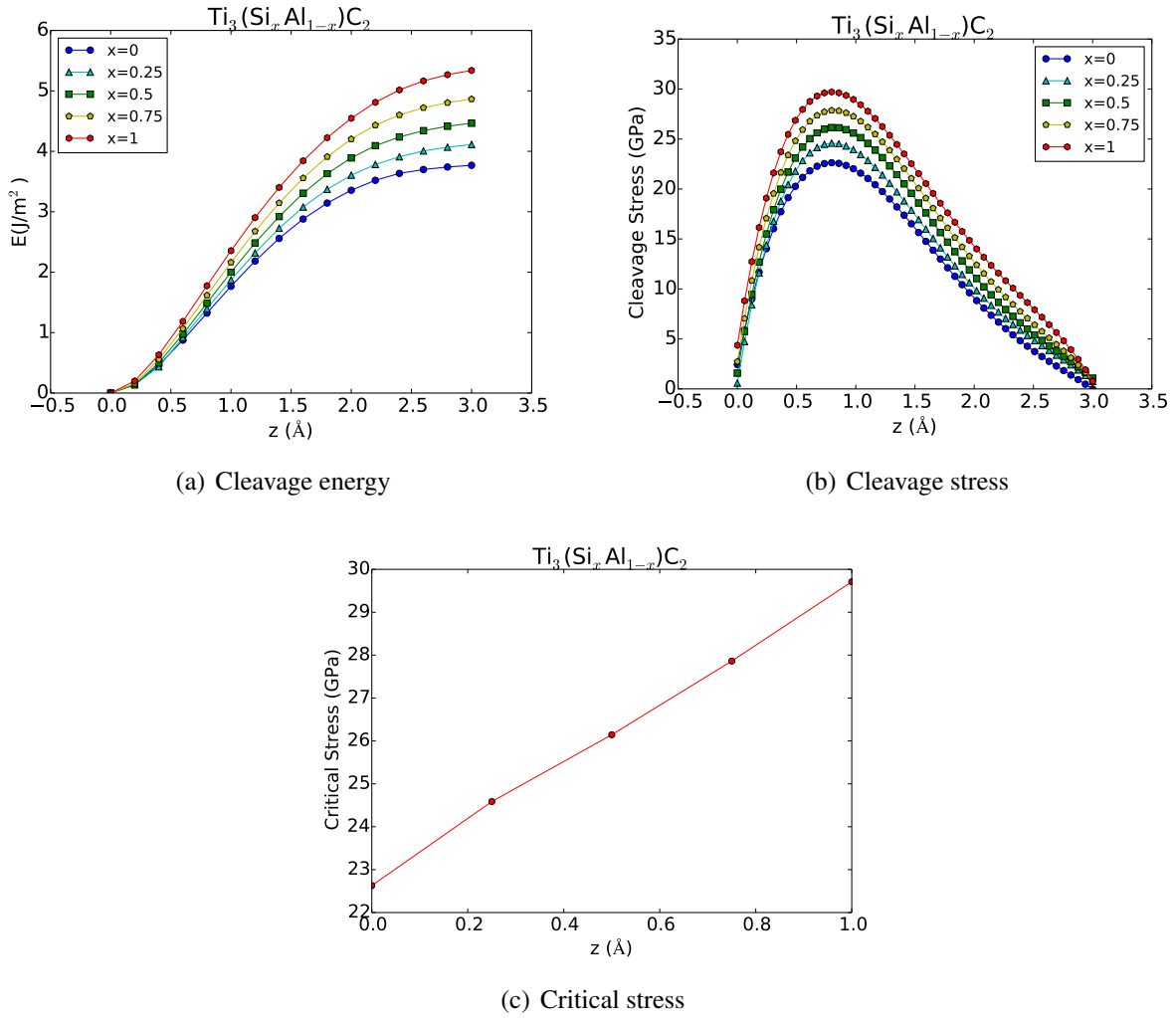
(c) Critical stress

Figure 3.10: (a) Cleavage energy, (b) cleavage stress, and (c) critical stress of the $Ti_3(Si_xAl_{1-x})C_2$. Reprinted with permission from [1].

		x=0	x=0.25	x=0.5	x=0.75	x=1
Critical stress (GPa)	calc	22.63	24.59	26.14	27.86	29.71
Intrinsic hardness (GPa)	exp	11.4 [46]				26 [47]

Table 3.3: Calculated maximum cleavage stress (critical stress) values of $Ti_3(Si_xAl_{1-x})C_2$, and experimentally reported intrinsic hardness of Ti_3AlC_2 and Ti_3SiC_2.

the mechanical properties of MAX phases in the continuum limit as cleavage/slip energy as a function of displacement and separation can be used to build cohesive zone models that account for the highly anisotropic behavior in these materials.

Here, we present the results of our investigation of the cleavage energy in these MAX alloys. The results of the calculated cleavage energies are shown in Fig. 3.10(a). As can be seen from this figure, the cleavage energy sharply increases up to 1 of cleavage distance, and it is almost constant around the cleavage distance of 3 . The cleavage stress, shown in Fig. 3.10(b), is derived from the cleavage energy, and the maximum cleavage stress appears around the cleavage distance of 0.9 . The critical stress (maximum cleavage stress) of $Ti_3(Si_xAl_{1-x})C_2$ increases with increasing amount of Si, and it is shown in Fig. 3.10(c). In Table 3.3, we compared the calculated critical stress values of Ti_3AlC_2 and Ti_3SiC_2 with nano-indentation experimental data (intrinsic hardness) and not the Vickers hardness. When a large force is applied, Vickers hardness measurement (macroscopic hardness) captures the effect of defect and grain boundary effects on the deformation, and it is thus not surprising that the Vickers hardness is underestimated when compared to the intrinsic hardness and calculated cleavage stress. One must consider, however, that there might be a few defect and grain boundary effects on the intrinsic hardness measurement so that it is underestimated when compared to the calculated cleavage stress [46]. Also tension-shear coupling would lower the upper limit of the cleavage stress in an indentation experiment [48]. Our calculations do not include the effects of defects and grain boundaries, so the calculated cleavage energy and cleavage stress show purely the chemical effect, which is related to the bond strengths in the $Ti_3(Si_xAl_{1-x})C_2$ system.

As aforementioned above, we considered internal stresses in the unit cell, and out of the unit cell to validate the cleavage model. First, to consider internal stresses in the unit cell, we studied the elastic response of neighboring regions in the unit cell. Fig. 3.11 shows the cleavage energy and stress of ideal brittle model and relaxation model. The ideal brittle model has higher cleavage energy and stress than those of relaxation model. Particularly, the critical stress of ideal brittle model is 23.02 GPa and that of relaxation model is 22.63 GPa. The cleavage energy of the ideal brittle model is composed of the decohesion energy and strain energy in the system, while the

27

(a) Cleavage energy　　　　　(b) Cleavage stress
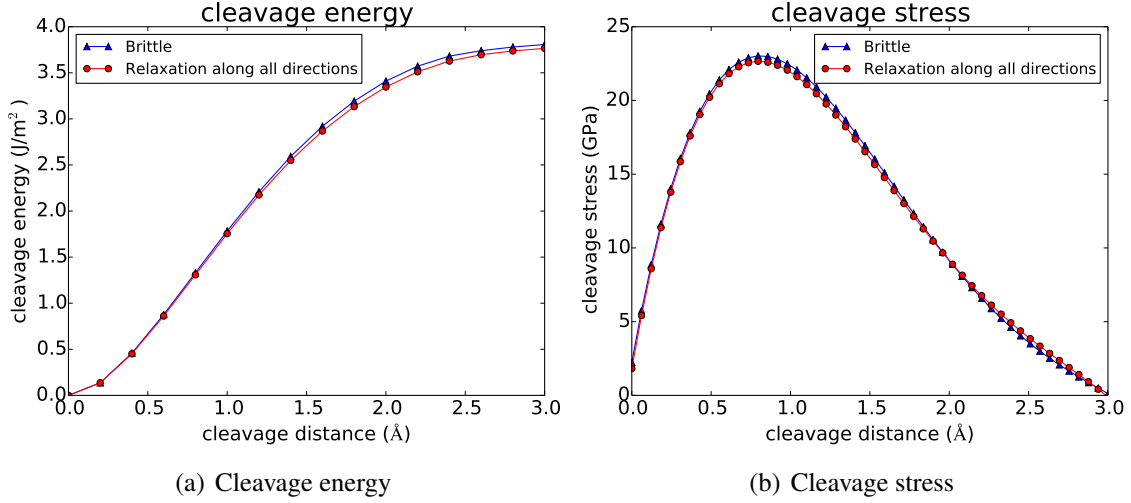
Figure 3.11: (a) and (b) show the cleavage energy and stress of ideal brittle model and relaxation model of Ti_3AlC_2. Reprinted with permission from [1].

relaxation model minimized the strain energy and the decohesion energy is dominant during the cleavage process.

Second, to further elucidate, the effect of system size on our cleavage calculations are studied. We generated systems with 1,2,3,4, and 5 unit cells along c directions containing one single cleavage surface. Then the cleavage energy and stress of different system sizes are calculated and shown in Fig. 3.12. Our results suggest that the cleavage energy of all systems is increasing sharply around 1 and converging at 3 of cleavage distance. The cleavage stress of system is derived from the cleavage energy and shows the maximum value around 0.9 of cleavage distance. The critical stress of 1, 2, 3, 4, and 5 unit cells in the Ti_3AlC_2 systems are 22.66, 22.60, 22.57, 22.54, and 22.52, respectively in the unit of GPa. These calculations suggest that the size of the system does not affect the results of the cleavage energy and stress calculations and thus one can use a single unit cell and obtain results that correspond to the intrinsic cleavage behavior in the large N limit.

3.5　Stacking Fault Energy (SFE)

Energy and shear stress curves under $\langle 2\bar{1}\bar{1}0 \rangle \{0001\}$ and $\langle 0\bar{1}10 \rangle \{0001\}$ shear deformations for Ti_3AlC_2, $Ti_3(Al_{0.5}Si_{0.5})C_2$, and Ti_3SiC_2 are presented in Fig. 3.13 and Fig. 3.14, respectively.

(a) Cleavage energy   (b) Cleavage stress
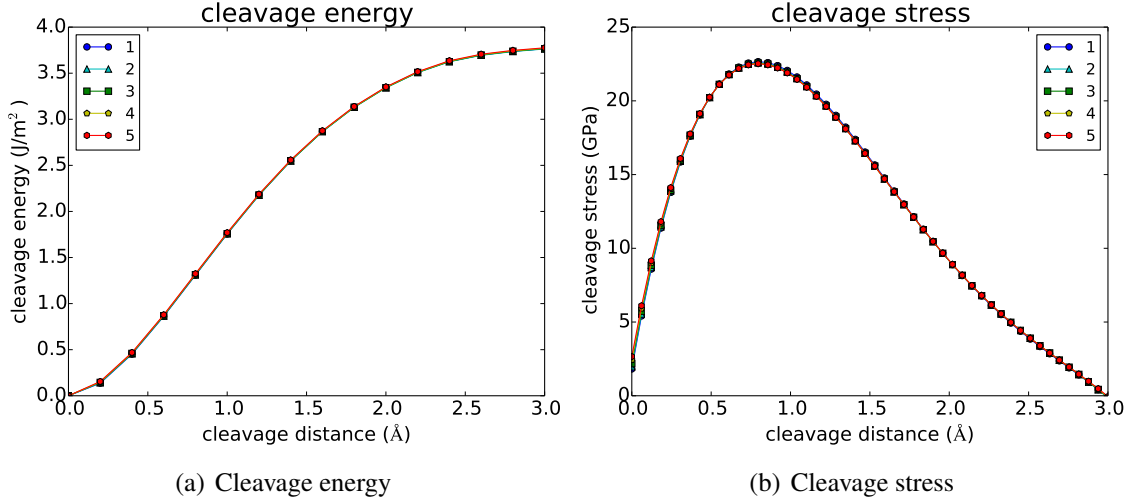
Figure 3.12: (a) and (b) show the cleavage energy and stress of 1, 2, 3, 4, and 5 unicells in the Ti$_3$AlC$_2$ systems with one cleavage surface. Reprinted with permission from [1].

	Ti$_3$AlC$_2$	Ti$_3$(Al$_{0.5}$Si$_{0.5}$)C$_2$	Ti$_3$SiC$_2$
USFE under $\langle 0\bar{1}10 \rangle \{0001\}$ pure alias shear deformation	1.34	1.45	1.71
USFE under $\langle 2\bar{1}\bar{1}0 \rangle \{0001\}$ pure alias shear deformation	0.56	0.79	1.02
2C$_{44}$/(C$_{11}$-C$_{12}$)	0.879	0.997	1.138

Table 3.4: USFE in the unit of J/m^2 under $\langle 0\bar{1}10 \rangle \{0001\}$ and $\langle 2\bar{1}\bar{1}0 \rangle \{0001\}$ pure alias shear deformation, and the anisotropy ratio for Ti$_3$AlC$_2$, Ti$_3$(Al$_{0.5}$Si$_{0.5}$)C$_2$, and Ti$_3$SiC$_2$.
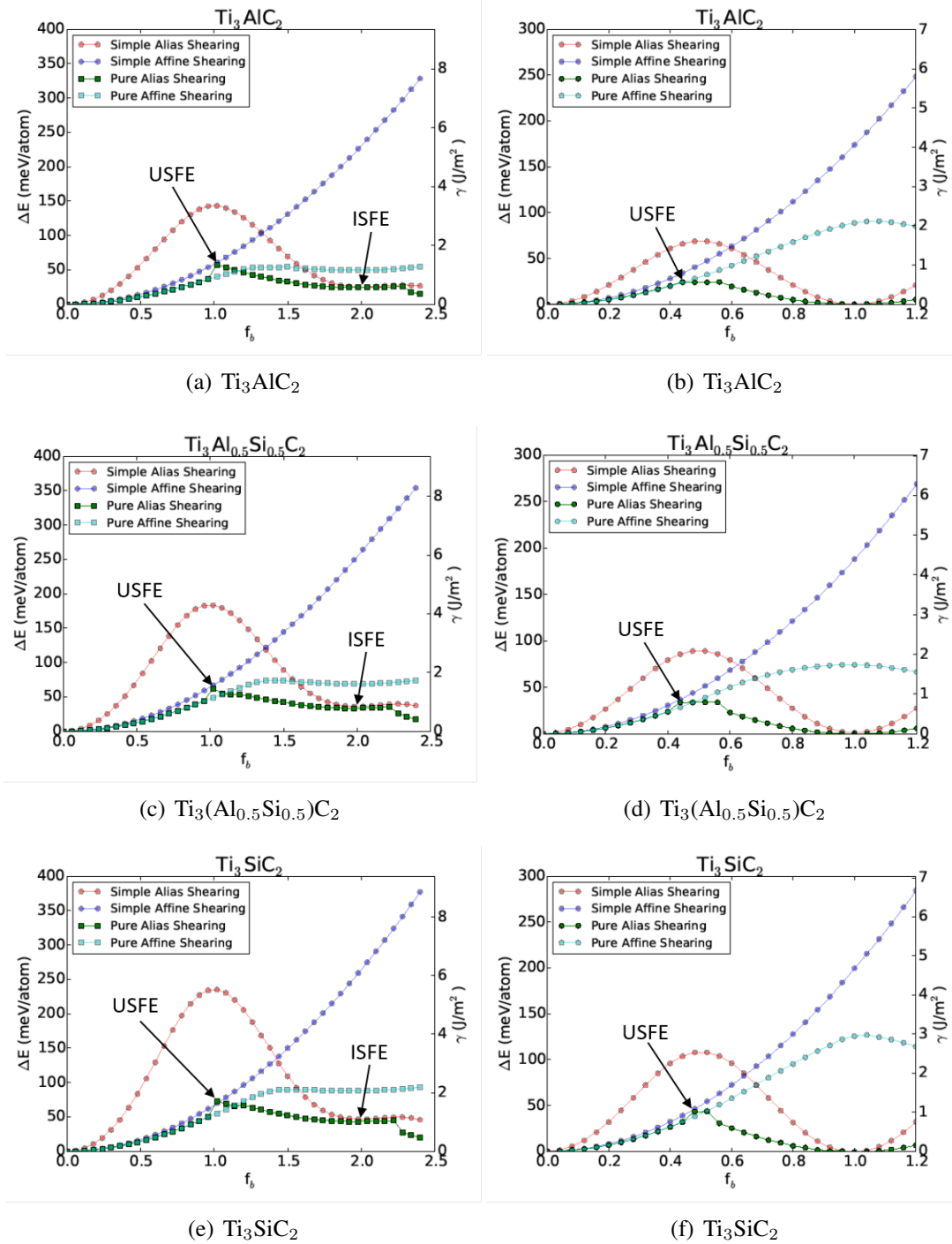
Figure 3.13: Energy as a function of fraction of Burgers vector, f_b. (a), (c), and (e) are under $\langle 0\bar{1}10\rangle\{0001\}$ shear deformation for Ti_3AlC_2, $Ti_3Al_{0.5}Si_{0.5}C_2$, and Ti_3SiC_2, respectively. (b), (d), and (f) are under $\langle 2\bar{1}\bar{1}0\rangle\{0001\}$ shear deformation for Ti_3AlC_2, $Ti_3Al_{0.5}Si_{0.5}C_2$, and Ti_3SiC_2, respectively. Reprinted with permission from [1].
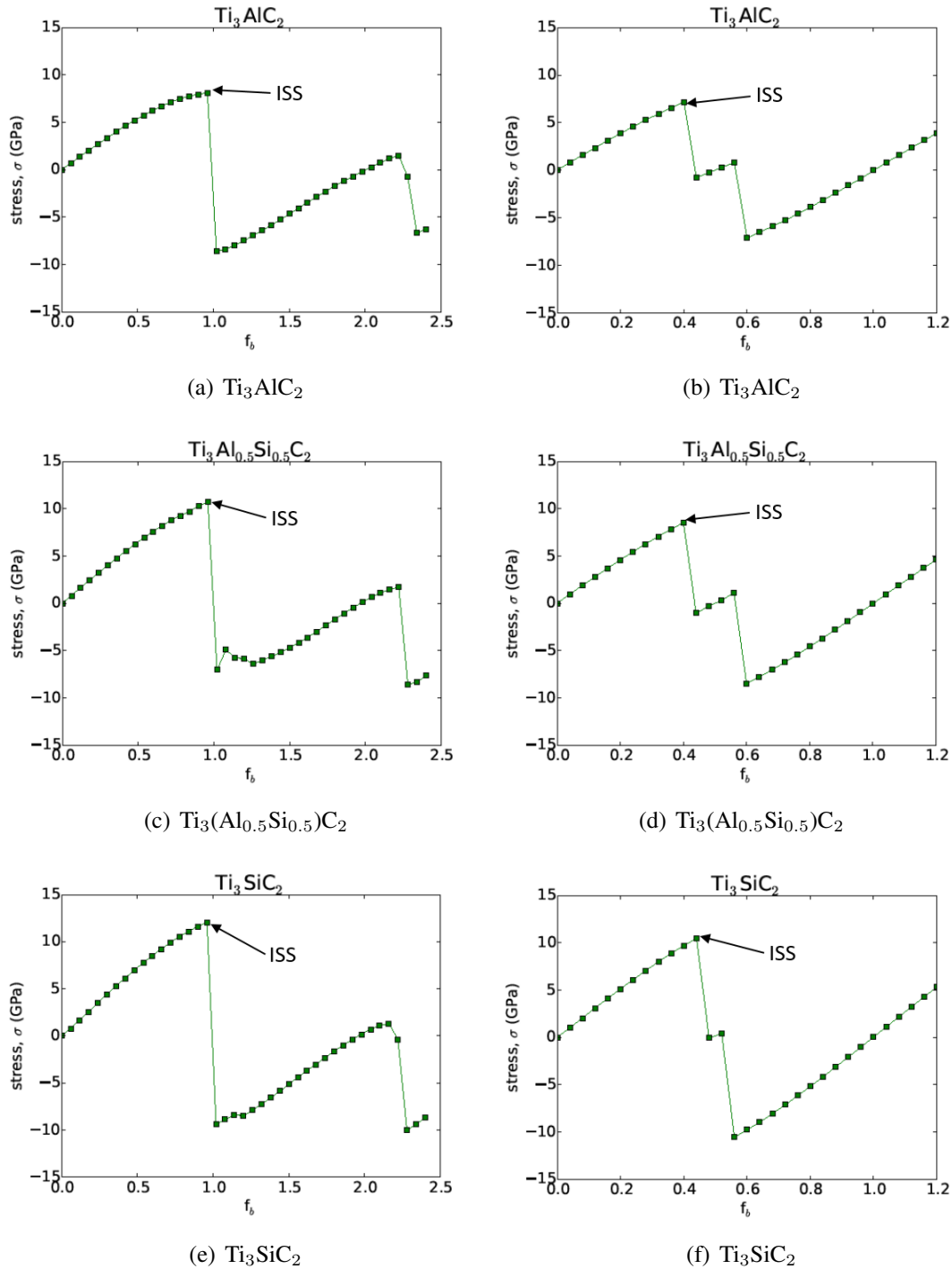
Figure 3.14: Stress as a function of fraction of Burgers vector, f_b. (a), (c), and (e) are under $\langle 0\bar{1}10 \rangle \{0001\}$ shear deformation for Ti_3AlC_2, $Ti_3Al_{0.5}Si_{0.5}C_2$, and Ti_3SiC_2, respectively. (b), (d), and (f) are under $\langle 2\bar{1}\bar{1}0 \rangle \{0001\}$ shear deformation for Ti_3AlC_2, $Ti_3Al_{0.5}Si_{0.5}C_2$, and Ti_3SiC_2, respectively. Reprinted with permission from [1].

The energy variation is presented as a function of the fraction of the Burgers vector, f_b. The maximum energy corresponds to the unstable stacking fault energy (USFE), which can be related to the energy needed for the dislocation nucleation. The minimum energy is the intrinsic stacking fault energy (ISFE), which can be related to the ductility of a material. The maximum shear stress corresponds to the ideal shear stress (ISS), which is related to the stress necessary for the formation of stacking faults. The pure alias shear deformation is a more reliable description of dislocation generation mechanism, since displacement is generated at the top layer, and relaxation leads to displacement from top to lower layers. The USFE under pure alias shear deformation for Ti_3AlC_2, $Ti_3(Al_{0.5}Si_{0.5})C_2$, and Ti_3SiC_2 are presented in Table 3.4. The USFE increases with increasing Si so that the Ti_3AlC_2 is more ductile than Ti_3SiC_2. The anisotropy ratio, $2C_{44}/(C_{11}-C_{12})$, quantifies how easy or difficult the shear deformation is. The low anisotropy ratio values in Table 3.4 suggest that Ti_3AlC_2 is more ductile than the Ti_3SiC_2.

Under $\langle 0\bar{1}10 \rangle$ $\{0001\}$ shear deformation, the USFE increases with increasing Si as shown in Fig. 3.13(a), (c), and (e). Up to 30% of shear deformation, all the deformation modes are identical except for simple alias shear. Beyond 30% of shear deformation, the energy of simple affine shear is higher than that of pure affine and alias shear. Investigation of pure shear deformation is important since it allows all the atoms to be fully relaxed so that the stresses do not correspond to the shear deformation is vanished. The unit cell angles of shear are presented in Fig. 3.15(a). The α, β, and γ are unit cell angles, and as it can be seen in Fig. 3.15(a) α is changing with constant β and γ. The shear energetics in Fig. 3.13(a) shows that the stacking fault has generated at 1.0 and 2.3 of f_b under pure alias shear deformation of Ti_3AlC_2. To clarify the generation of stacking fault, α' is shown in Fig. 3.15(a) and (b), which is the cell angle containing M and A elements. Under pure alias shear deformation, α' is decreasing like α, however, α' sharply increases at 1.0 and 2.3 of f_b. It represents the stacking fault has generated between M and A layers.

Under $\langle 2\bar{1}\bar{1}0 \rangle$ $\{0001\}$ shear deformation, the USFE increases with increasing Si as shown in Fig. 3.13(b), (d), and (f). Up to 20 % of shear deformation, all the deformation modes are identical except for simple alias shear. Beyond 20 % of shear deformation, the energy of simple affine shear

32
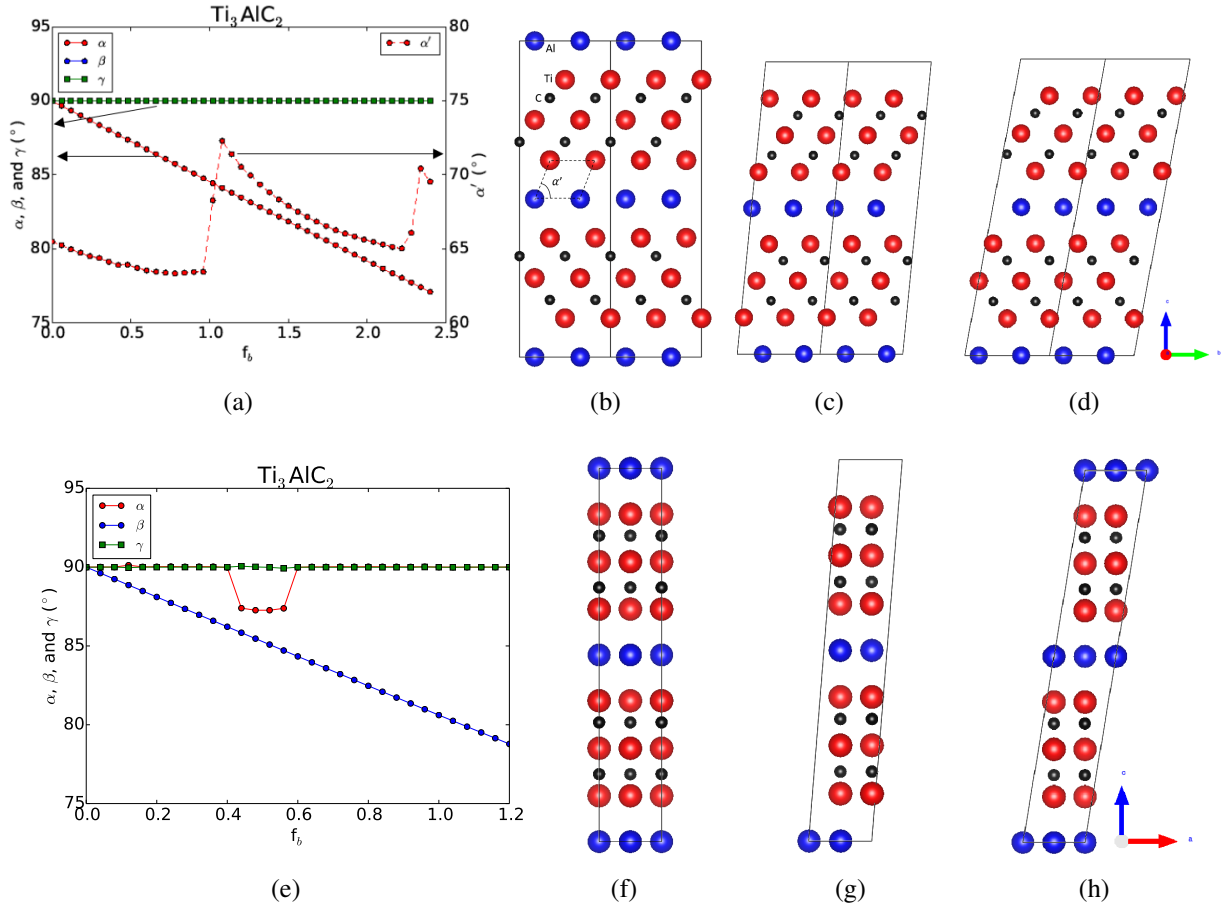
Figure 3.15: (a) shows cell angles of the Ti_3AlC_2 system under $\langle 0\bar{1}10 \rangle \{0001\}$ pure alias shear deformation. (b), (c), and (d) show the structure of Ti_3AlC_2 system under $\langle 0\bar{1}10 \rangle \{0001\}$ pure alias shear deformation of $f_b = 0$, 1.0, and 2.0, respectively. (e) is unit cell angles of the Ti_3AlC_2 system under $\langle 2\bar{1}\bar{1}0 \rangle \{0001\}$ pure alias shear deformation. (f), (g), and (h) are the Ti_3AlC_2 system under $\langle 2\bar{1}\bar{1}0 \rangle \{0001\}$ pure alias shear deformation of f_b=0, 0.44, 1.0, respectively. Red, blue, and black atoms are Ti, Al, and C, respectively. Reprinted with permission from [1].
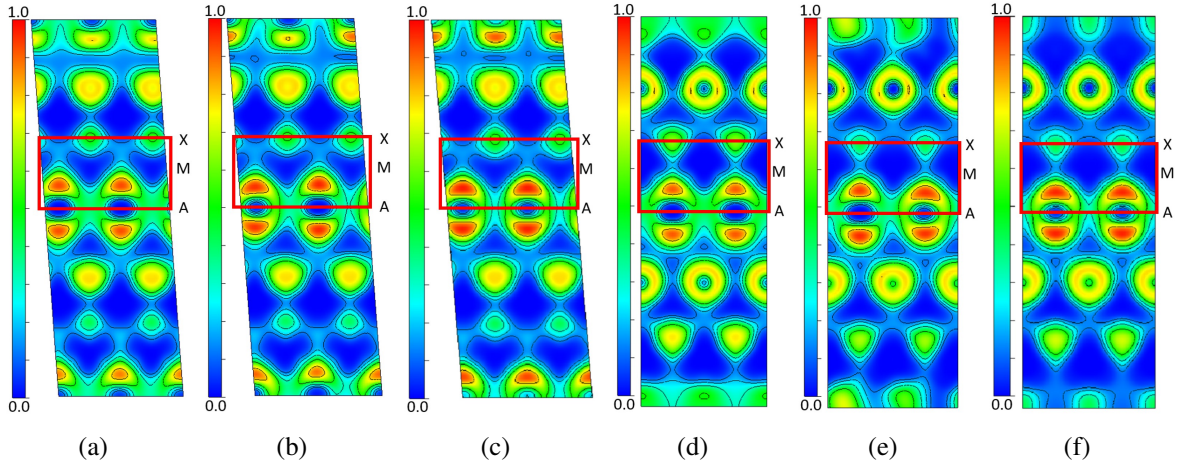
Figure 3.16: (010) Plane view of electron localization function (ELF) under $\langle 2\bar{1}\bar{1}0 \rangle \{0001\}$ pure alias shear deformation of $Ti_3(Si_xAl_{1-x})C_2$ with (a) x=0, (b) x=0.5, (c) x=1, and $\langle 0\bar{1}10 \rangle \{0001\}$ pure alias shear deformation with (d) x=0, (e) x=0.5, and (f) x=1 at the level of USFE. Reprinted with permission from [1].

is higher than that of pure affine and alias shear. As mentioned above, pure shear leads to a more stable system than simple shear. The unit cell angles at various stages of shears are presented in Fig. 3.15(e). Unlike $\langle 0\bar{1}10 \rangle \{0001\}$ shear deformation, α changes around 0.5 of f_b under $\langle 2\bar{1}\bar{1}0 \rangle \{0001\}$ shear deformation.

Both USFE under $\langle 2\bar{1}\bar{1}0 \rangle \{0001\}$ and $\langle 0\bar{1}10 \rangle \{0001\}$ shear deformation increase with an increasing amount of Si. In addition, USFE under $\langle 2\bar{1}\bar{1}0 \rangle \{0001\}$ shear deformation is lower than USFE under $\langle 0\bar{1}10 \rangle \{0001\}$ shear deformation, thus $\langle 2\bar{1}\bar{1}0 \rangle \{0001\}$ shear deformation will be preferable under the deformation behavior. To demonstrate this, analysis of ELF and charge density were carried out. As shown in FIg. 3.16, distributions of electrons between M-A and are getting higher with increasing Si-content under both $\langle 2\bar{1}\bar{1}0 \rangle \{0001\}$ and $\langle 0\bar{1}10 \rangle \{0001\}$ shear deformations. This causes A elements to be charged more negatively with increasing amount of Si. Fig. 3.17 shows the increased charge density of A element under both $\langle 2\bar{1}\bar{1}0 \rangle \{0001\}$ and $\langle 0\bar{1}10 \rangle \{0001\}$ shear deformations, which makes the atomic bond between the M-A layer stronger. The number of valence electrons per atom are shown in Table 3.5. The number of valence electrons of M and X elements are almost constant, while that of A element is increasing with increasing
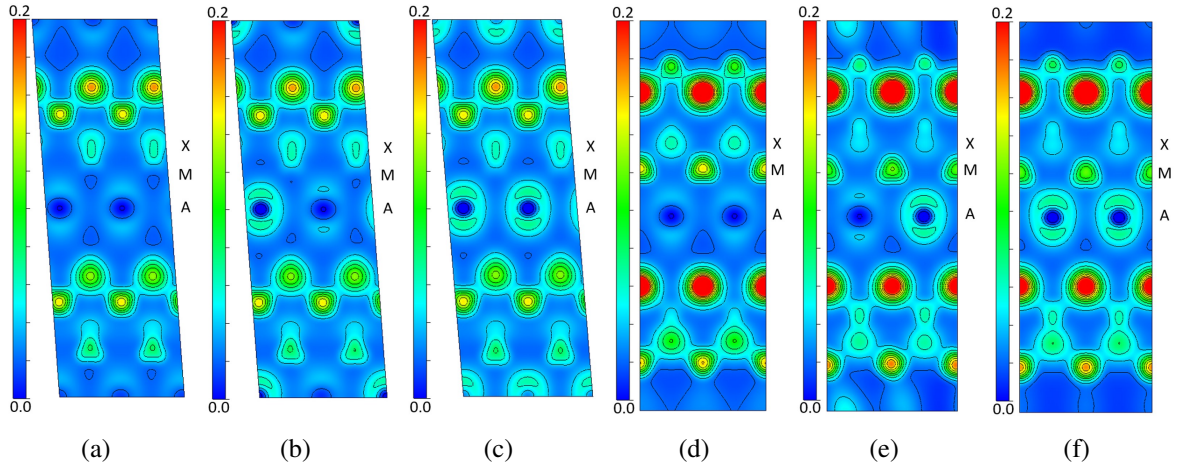
Figure 3.17: (010) Plane view of charge density under $\langle 2\bar{1}\bar{1}0 \rangle \{0001\}$ pure alias shear deformation of $Ti_3(Si_xAl_{1-x})C_2$ with (a) x=0, (b) x=0.5, (c) x=1, and $\langle 0\bar{1}10 \rangle \{0001\}$ pure alias shear deformation with (d) x=0, (e) x=0.5, and (f) x=1 at the level of USFE. Reprinted with permission from [1].

Phase	Ti_3AlC_2	$Ti_3(Si_{0.5}Al_{0.5})C_2$	Ti_3SiC_2
$\langle 2\bar{1}\bar{1}0 \rangle$ pure alias shear deformation			
Ti	1.91	1.90	1.89
Al & Si	4.11	4.72	5.33
C	6.58	6.55	6.51
$\langle 0\bar{1}10 \rangle$ pure alias shear deformation			
Ti	1.92	1.90	1.89
Al & Si	4.07	4.68	5.27
C	6.59	6.56	6.53

Table 3.5: The number of valence electrons per atom at the level of USFE under $\langle 2\bar{1}\bar{1}0 \rangle \{0001\}$ and $\langle 0\bar{1}10 \rangle \{0001\}$ pure alias shear deformations.
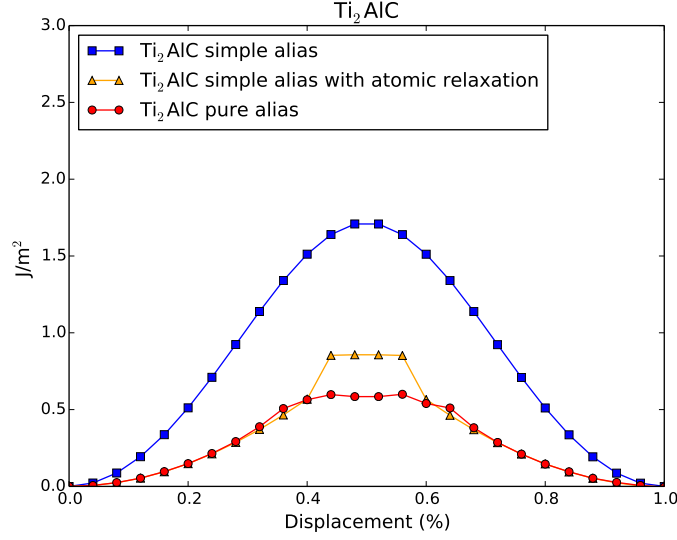
Figure 3.18: Energetics of $\langle 2\bar{1}\bar{1}0 \rangle \{0001\}$ alias shear deformation of Ti_2AlC. Reprinted from [4].

amount of Si. This results in increasing USFE with increasing amount of Si. In addition, the number of valence electrons of the A element under $\langle 2\bar{1}\bar{1}0 \rangle$ shear deformation is higher compared to that of A element under $\langle 0\bar{1}10 \rangle$ shear deformation. Under $\langle 2\bar{1}\bar{1}0 \rangle$ shear deformation, the strong atomic bond between the M-A layer makes the system more stable than $\langle 0\bar{1}10 \rangle$ shear deformation, thus $\langle 2\bar{1}\bar{1}0 \rangle$ shear deformation will be preferable than $\langle 0\bar{1}10 \rangle$ shear deformation.

To validate the shear model, the resultant energy curves of three different calculation modes are shown in Fig. 3.18. Here we studied Ti_2AlC system, which is the most simple structure of $Ti_{n+1}AlC_n$ to minimize the computational cost. First, we compared energetics of simple alias model and simple alias with atomic relaxation model. The simple alias model does not allow any relaxation under the shear deformation, while simple alias with atomic relaxation model allows the atomic relaxation to vanish stress not corresponds to the shear deformation. The energy of atomic relaxation model dramatically drops down compared to the simple alias model. It suggests that the relaxation of atomic positions has to be followed during the shear deformation. Second, we compared energetics of atomic relaxation model to the pure alias model. Like relaxation model, pure alias model considers the atomic relaxation, while, unlike atomic relaxation model, pure alias model also considers the structural relaxation, which include the relaxation of volume and shape.

Up to 40 % the energy of atomic relaxation model and pure alias mode show very similar trend, however between 40 % and 60 % the pure alias model shows much lower energy than atomic relaxation model. It suggests that the structural relaxation plays an important role at the level of the generation of stacking fault.

4.   THE EFFECT OF NUMBER OF STACKING LAYERS ON DEFORMATION BEHAVIORS IN $Ti_{n+1}AlC_n$ AND $Ta_{n+1}AlC_n$ SYSTEMS

4.1   Structural and Electonic Properties

The optimized structures of $Ti_{n+1}AlC_n$ and $Ta_{n+1}AlC_n$ systems are shown in Fig. 4.1, using VESTA. The calculated a- and c- lattice parameters are shown in Table 4.1, which agree well with experimental and other calculated results [18]. Both a- and c- lattice parameter values of $Ta_{n+1}AlC_n$ are higher than those of $Ti_{n+1}AlC_n$. In addition, with the increasing number of stacking layers, increasing number of n, a-lattice parameter is almost constant, while c-lattice parameter increases. This intuitively makes sense and points to the relative insensitivity of structural parameters to specific stacking number, indicating strong localization of the bonding within the M-A layers.

4.2   Cleavage energy

In $Ti_{n+1}AlC_n$ and $Ta_{n+1}AlC_n$ systems we present the cleavage energy and stress calculations as a function of stacking number, n. The resultant cleavage energy and stress are shown in Fig. 4.2. As it is shown in Fig. 4.2(a) and 4.2(c), the cleavage energy increases sharply up to around 1 of separation, after which its rate of increase decays and in fact saturates at about 3 in both $Ti_{n+1}AlC_n$ and $Ta_{n+1}AlC_n$ systems. The cleavage stress is derived from the cleavage energy, and it is shown in Fig. 4.2(b) and 4.2(d). The maximum cleavage stress (critical stress) appears at around 0.9 of separation. The critical stress of $Ti_{n+1}AlC_n$ is 23.88, 22.65, 22.55, 22.51, and 22.46 GPa with n = 1, 2, 3, 4, and 5, respectively. The critical stress of $Ti_{n+1}AlC_n$ is 28.33, 28.32, 26.29, 26.81, and 26.65 GPa with n = 1, 2, 3, 4, and 5, respectively.

The critical stress of $Ta_{n+1}AlC_n$ is higher than the critical stress of $Ti_{n+1}AlC_n$, while the number of stacking layers (the number of n) does not significantly affect the critical stress. The slight changes of critical stress in $Ti_{n+1}AlC_n$ and $Ta_{n+1}AlC_n$ systems with a different number of stacking layers can be explained by the analysis of charge transfer of Ti, Ta, and Al in cleaved layers.
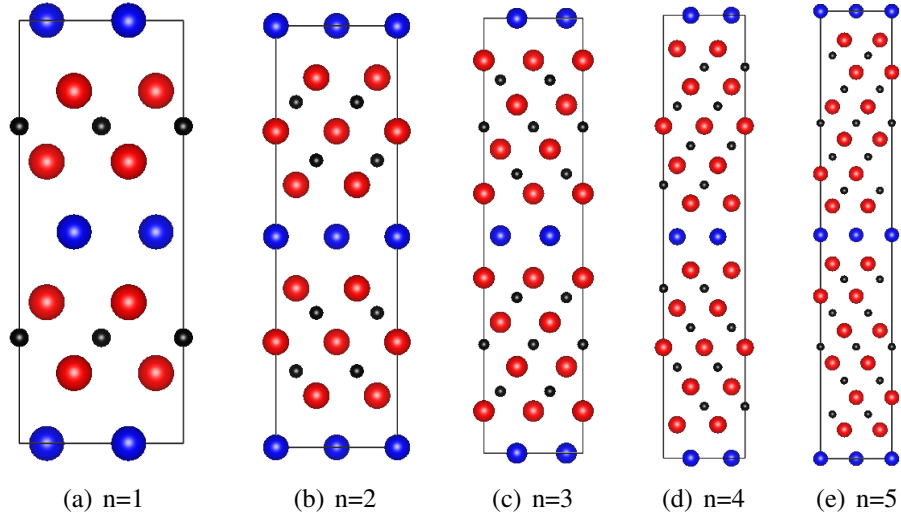
(a) n=1   (b) n=2   (c) n=3   (d) n=4   (e) n=5

Figure 4.1: Crystal structure of the $Ti_{n+1}AlC_n$ ($Ta_{n+1}AlC_n$) with (a) n=1, (b) n=2, (c) n=3, (d) n=4, and (e) n=5. Red, blue, and black atoms represent Ti (Ta), Al, and C, respectively. Reprinted from [4].

Phase	Ti_2AlC	Ti_3AlC_2	Ti_4AlC_3	Ti_5AlC_4	Ti_6AlC_5
a	3.069	3.082	3.085	3.085	3.084
c	13.734	18.652	23.588	28.541	33.505
Phase	Ta_2AlC	Ta_3AlC_2	Ta_4AlC_3	Ta_5AlC_4	Ta_6AlC_5
a	3.092	3.099	3.136	3.130	3.145
c	13.951	19.252	24.261	29.546	34.550

Table 4.1: The a- and c- lattice parameter values of $Ti_{n+1}AlC_n$ and $Ta_{n+1}AlC_n$ (n=1, 2, 3, 4, and 5) in the unit of .
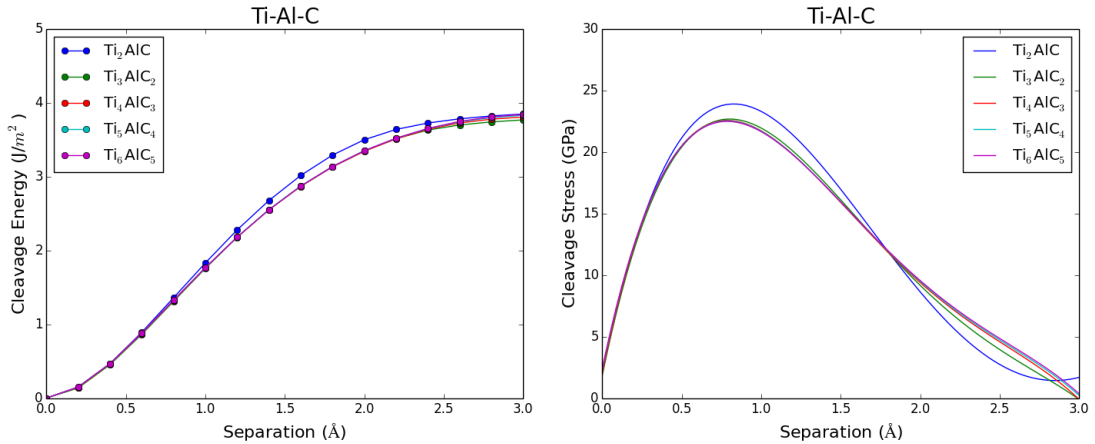
(a) Cleavage energy of $\text{Ti}_{n+1}\text{AlC}_n$

(b) Cleavage stress of $\text{Ti}_{n+1}\text{AlC}_n$
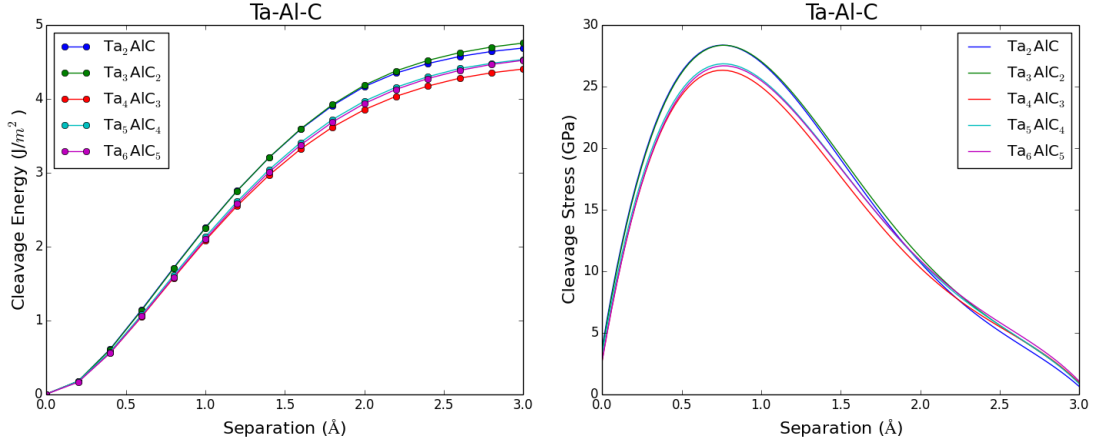
(c) Cleavage energy of $\text{Ta}_{n+1}\text{AlC}_n$

(d) Cleavage stress of $\text{Ta}_{n+1}\text{AlC}_n$
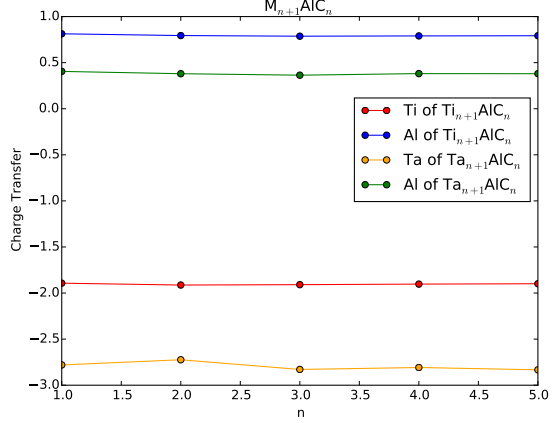
(e) Charge transfer of $\text{M}_{n+1}\text{AlC}_n$

Figure 4.2: Cleavage energy and stress of the (a), (b) $\text{Ti}_{n+1}\text{AlC}_n$ and (c), (d) $\text{Ta}_{n+1}\text{AlC}_n$ with n=1, n=2, n=3, n=4, and n=5. (e) Charge transfer of Ti, Ta, and Al of $\text{M}_{n+1}\text{AlC}_n$ (M = Ti and Ta). Reprinted from [4].

Phase	Ti_2AlC	Ti_3AlC_2	Ti_4AlC_3	Ti_5AlC_4	Ti_6AlC_5
Ti	2.107 (-1.893)	2.087 (-1.913)	2.091 (-1.909)	2.097 (-1.903)	2.101 (-1.899)
Al	3.813 (+0.813)	3.794 (+0.794)	3.787 (+0.787)	3.79 (+0.79)	3.792 (+0.792)

Phase	Ta_2AlC	Ta_3AlC_2	Ta_4AlC_3	Ta_5AlC_4	Ta_6AlC_5
Ta	2.22 (-2.78)	2.276 (-2.724)	2.171 (-2.829)	2.192 (-2.808)	2.167 (-2.833)
Al	3.405 (+0.405)	3.38 (+0.38)	3.364 (+0.364)	3.381 (+0.381)	3.38 (+0.38)

Table 4.2: Calculated number of valence electrons (charge transfer) in $Ti_{n+1}AlC_n$ and $Ta_{n+1}AlC_n$ is obtained by Bader analysis. Particularly, charge analysis of Ti, Ta, and Al in cleaved layers.

The number of valence electrons and charge transfer are shown in Table 4.2 and Fig. 4.2(e). In the $Ti_{n+1}AlC_n$ system, the calculated charge transfer of Ti is -1.893, -1.913, -1.909, -1.903, and -1.899, and that of Al is 0.813, 0.794, 0.787, 0.79, and 0.792 with n = 1, 2, 3, 4, and 5, respectively. In $Ta_{n+1}AlC_n$ system, the calculated charge transfer of Ta is -2.78, -2.724, -2.829, -2.808, and -2.833, and calculated charge transfer of Al is 0.405, 0.38, 0.364, 0.381, and 0.38 with n = 1, 2, 3, 4, and 5, respectively. The charge transfer of Ti, Ta, and Al changes by about 1% at most with changing n, providing a rationalization for the fact that the critical cleavage stress in $Ti_{n+1}AlC_n$ and $Ta_{n+1}AlC_n$ is insensitive to stacking number: the strength of the bonding between M and A layers is highly localized within the M-A layers themselves and the stacking number does not affect their interactions.

4.3 Stacking Fault Energy (SFE)

In the previous section, it has been shown that the $\langle 2\bar{1}\bar{1}0 \rangle \{0001\}$ alias shear deformation is the most preferable shear deformation. Hence we present energy curves under $\langle 2\bar{1}\bar{1}0 \rangle \{0001\}$ alias shear deformation of $Ti_{n+1}AlC_n$ and $Ta_{n+1}AlC_n$ to study chemistry and stacking layer number effects on shear deformation. The energetics of $Ti_{n+1}AlC_n$ under simple shear deformations by shearing M-X and M-A layers as a function of the fraction of the Burgers vector are shown in
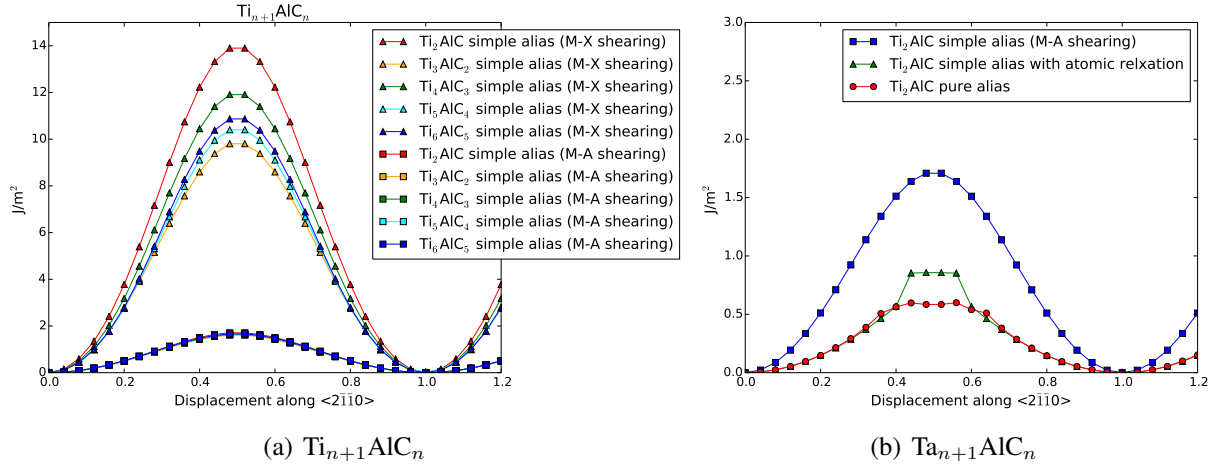
Figure 4.3: (a) Simple alias shear deformation energy curves of $Ti_{n+1}AlC_n$ by shearing M-X (triangle) and M-A (square) layers with n = 1-5. (b) Shear energy curves of Ti_2AlC under simple alias without (square) and with (triangle) atomic relaxation, and pure alias (circle) shear deformation. Reprinted from [4].

Fig. 4.3(a). The resultant energies for the simple alias calculations by shearing M-X layers are much higher than those corresponding to the simple alias calculation by shearing M-A layers. This shows that the M-X bond strength is much higher than M-A bond strength, thus M-X layers are much more difficult to shear than M-A layers. In addition, the maximum energy is the required energy to shear layers, and the maximum energy for shearing M-X layers changes significantly with a different number of stacking layers. While, the maximum energy for shearing M-A layers does not change significantly with a different number of stacking layers. The analysis suggests that the number of stacking layers significantly affects the resultant energies under simple alias deformation by shearing M-X layers, which corresponds to the energy required to slip M and X layers, while the number of stacking layers does not significantly affect the resultant energies under simple alias deformation by shearing M-A layers. The energetics of simple alias calculations without and with atomic relaxation, and pure alias calculations are shown in Fig. 4.3(b). The resultant energies for the simple alias calculations are much higher than those corresponding to the pure alias calculation. The reason for this considerable overestimation is the fact that atomic relaxations consistent with the shear deformation of the cell must be taken into account in order

42
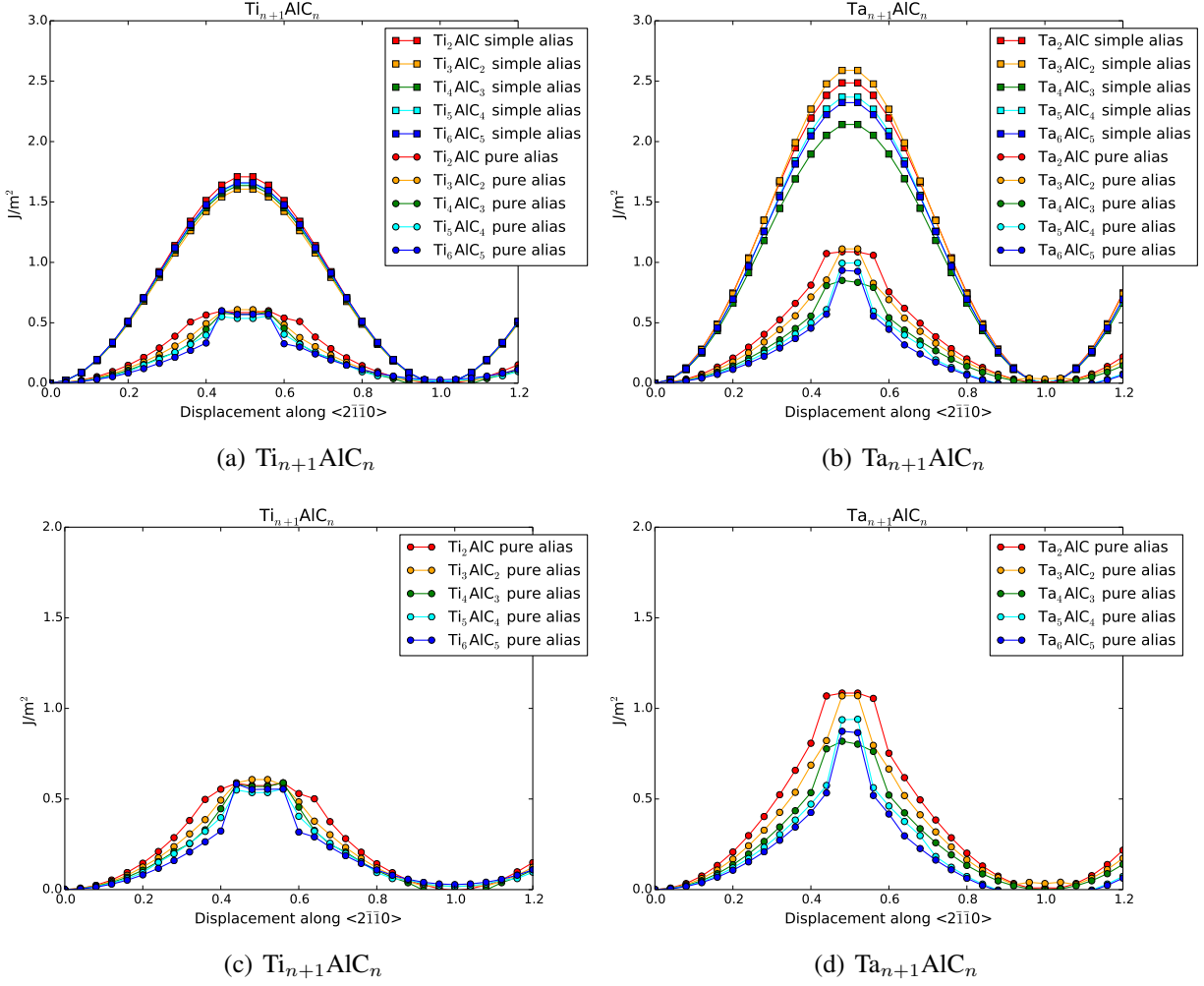
Figure 4.4: Shear energy curves of the (a) $Ti_{n+1}AlC_n$ and (b) $Ta_{n+1}AlC_n$ with n=1, n=2, n=3, n=4, and n=5. Pure alias shear energy curves of the (c) $Ti_{n+1}AlC_n$ and (d) $Ta_{n+1}AlC_n$ with n=1, n=2, n=3, n=4, and n=5. Reprinted from [4].

to minimize the total strain energy of the system. We note, however, that carrying out a simple alias shear, but allowing at least local ionic relaxations is sufficient to reduce the energy barrier to shear to values close to those obtained using the pure shear construction. Note, however, that when carrying out the pure shear transformation no assumption as to the identity of the sheared layers had to be made as this is a direct outcome of the constrained relaxation scheme.

The energetics of shear deformation for $Ti_{n+1}AlC_n$ and $Ta_{n+1}AlC_n$ systems are shown in Fig. 4.4. The unstable stacking fault energy (USFE), shown in Table 4.3, is the maximum energy

43

Phase	Ti_2AlC	Ti_3AlC_2	Ti_4AlC_3	Ti_5AlC_4	Ti_6AlC_5
USFE	0.588	0.607	0.589	0.556	0.555

Phase	Ta_2AlC	Ta_3AlC_2	Ta_4AlC_3	Ta_5AlC_4	Ta_6AlC_5
USFE	1.084	1.070	0.818	0.940	0.873

Table 4.3: The Unstable Stacking Fault Energy (USFE) of $Ti_{n+1}AlC_n$ and $Ta_{n+1}AlC_n$ systems with n = 1, 2, 3, 4, and 5 in the unit of J/m^2.

during the shear process, which is the required energy for the generation of stacking fault, and can be related to the required energy for the nucleation of dislocations [49]. In the $Ti_{n+1}AlC_n$ system, the USFE is 0.588, 0.607, 0.589, 0.556, and 0.555 in the unit of J/m^2 with n = 1, 2, 3, 4, and 5, respectively. In $Ta_{n+1}AlC_n$ system, the USFE is 1.084, 1.070, 0.818, 0.940, and 0.873 in the unit of J/m^2 with n = 1, 2, 3, 4, and 5, respectively. The USFE of $Ta_{n+1}AlC_n$ is considerably higher than that of $Ta_{n+1}AlC_n$, while the number of stacking layers does not significantly affect the USFE, which is consistent with the finding derived from the cleavage calculations. Here we note that the same conclusion would not have been arrived at if one were to consider shear deformation of these systems under simple alias deformation, which would predict differences of more than 30% in the calculated values for the USFE in the case of Ta-MAX phases. Moreover, the results show that the stacking fault is generated between M and A layers, not M and X layers, with the former pair being the most weakly bonded of the two, as M-X bonds tend to be covalent in nature and are much stronger than the predominantly metallic M-A bonds. Again, the generation of the stacking fault is highly localized and it is thus reasonable that the number of stacking layers does not affect the USFE. The difference between Ti- and Ta- MAX phases points, however, to the significant effect of chemistry on the strength between M and A layers in MAX phases.

To better understand the slip between M and A layers under shear deformation, the bond lengths of M-A and M-X were calculated and shown in Fig. 4.5. It has been shown that the USFE occurs when the shear deformation has reached a magnitude of about 0.4 Burgers vector, and stacking

(a) $\text{Ti}_{n+1}\text{AlC}_n$ (b) $\text{Ta}_{n+1}\text{AlC}_n$
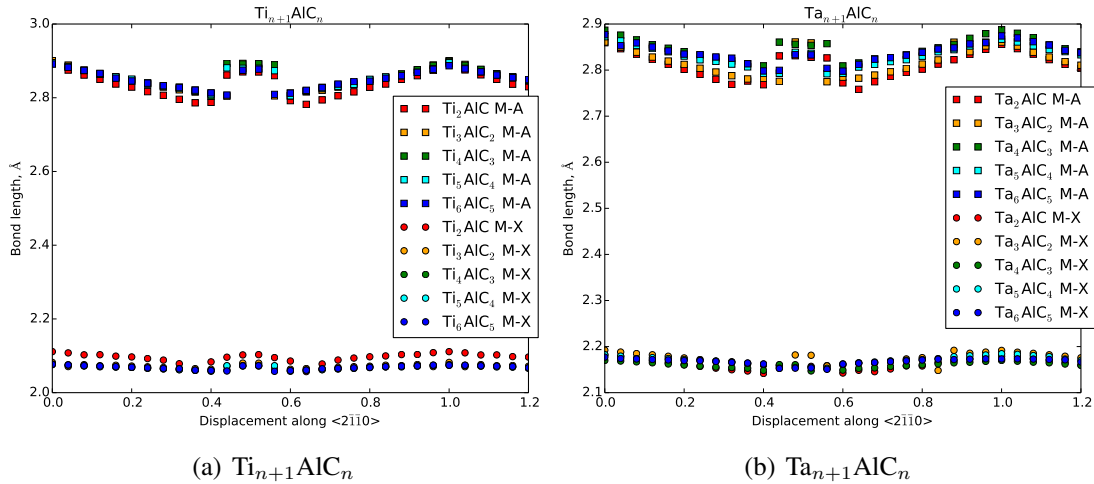
Figure 4.5: M-A and M-X bond lengths of the (a) $\text{Ti}_{n+1}\text{AlC}_n$ and (b) $\text{Ta}_{n+1}\text{AlC}_n$ with n=1, n=2, n=3, n=4, and n=5. Reprinted from [4].

fault has generated at this point as the system is unstable and incapable of resisting the formation of this stacking defect. The figure indicates that just before the generation of the stacking fault, the bond lengths of M-A and M-X are decreasing linearly. The decreasing in M-A bond length is thus associated with the considerable increase in the energetics of the shear deformation profile as the structure is being sheared. At the displacement level corresponding to the point at which the stacking fault is generated, the M-A bond length increases sharply by about 2%, while the M-X bond length is increased in a more parsimonious manner, indicating that the M-X layers are not affected significantly by the formation of the stacking fault. This figure shows that stacking fault is dominated by slip between the M and A layers.

To justify the unit cell alone is sufficient to achieve reasonable stacking fault energies, we studied pure alias shear deformation of Ti_2AlC with different system sizes. We studied the pure alias shear deformation along $\langle 2\bar{1}\bar{1}0 \rangle \{0001\}$ of Ti_2AlC with single unit cell and two unit cells along out of plane, and it is shown in Fig. 4.6. Both single unit cell and extended unit cell show the maximum energy, USFE, at 40 % of displacement. The USFE of the single unit cell and extended unit cell are 0.60 and 0.62 J/m^2, respectively. The calculated USFE of different cell sizes suggest that the system size does not affect the results of shear energy significantly and thus single unit cell

45

Figure 4.6: Shear energy curves of the Ti$_2$ALC system with one single unit cell (solid line) and two unit cells along out of plane (dashed line). Reprinted from [4].

is sufficient to study shear behavior and achieve reasonable stacking fault energy.

5. CLEAVAGE AND SHEAR BEHAVIORS OF DIFFERENT TYPES OF LAYERED

MATERIALS (TiC, Ti$_2$AlC, Ti, GRAPHENE)

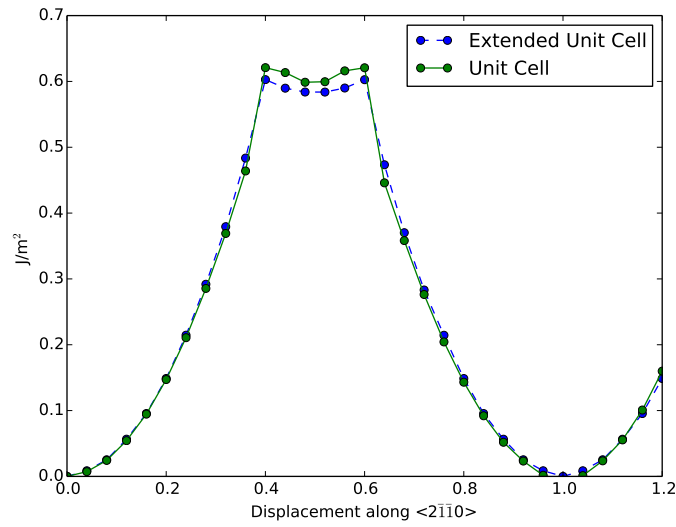## 5.1 Structural and Elastic Properties of Layered Materials

In the previous sections, we studied cleavage and shear behavior of MAX phases. First, we studied cleavage and shear behavior of Ti$_3$AlC$_2$ and Ti$_3$SiC$_2$. Si-containing MAX phases are well known as a elastically very stiff material. The elasticity by-itself is a very important material's property, since it tells us how large force a material can sustain without a permanent plastic deformation. We want to know how the material will behavior beyond the elastic region, and we believe that studying of the cleavage and shear behavior would be a very good starting point to understand the plastic deformation beyond the elastic region. To better understand of the cleavage and shear behavior of Ti$_3$SiC$_2$, we studied cleavage energy and shear energy of Ti$_3$AlC$_2$ and compared to those of Ti$_3$SiC$_2$. Particularly we choose Ti$_3$AlC$_2$, since the aluminium component in MAX phases can diffuse out and form alumina oxide layer and it is expected to have a good oxidation and thermal resistance. Ti$_3$AlC$_2$ is known as having a lower elastic modulus compared to the Ti$_3$SiC$_2$, and it is good to study how the different chemical components affect the cleavage and shear energy by comparing the cleavage and shear energies of Ti$_3$SiC$_2$ and Ti$_3$AlC$_2$. Then we have the cleavage and shear behavior of Ti$_{n+1}$AlC$_n$ and Ta$_{n+1}$AlC$_n$ to understand how the different stacking numbers, n, affect the cleavage and shear behavior. Particularly, we choose Ta$_{n+1}$AlC$_n$ system, since high order Ta$_{n+1}$AlC$_n$ has reported as they are experimentally synthesizable.

Here we studied the cleavage and shear behavior of different types of layered materials. We choose TiC, Ti$_2$AlC, Ti, and graphite to study how different types of materials like ceramic, MAX phases, metal, and van der Walls force dominant materials behave under the cleavage and shear process. First, we generated hexagonal closed packed systems of layered materials to study how the metal like A layer and ceramic like M-X layer are different in terms of the cleavage and shear. The crystal structures of TiC, Ti$_2$AlC, Ti, and graphite are shown in Fig. 5.1, and they are visualized
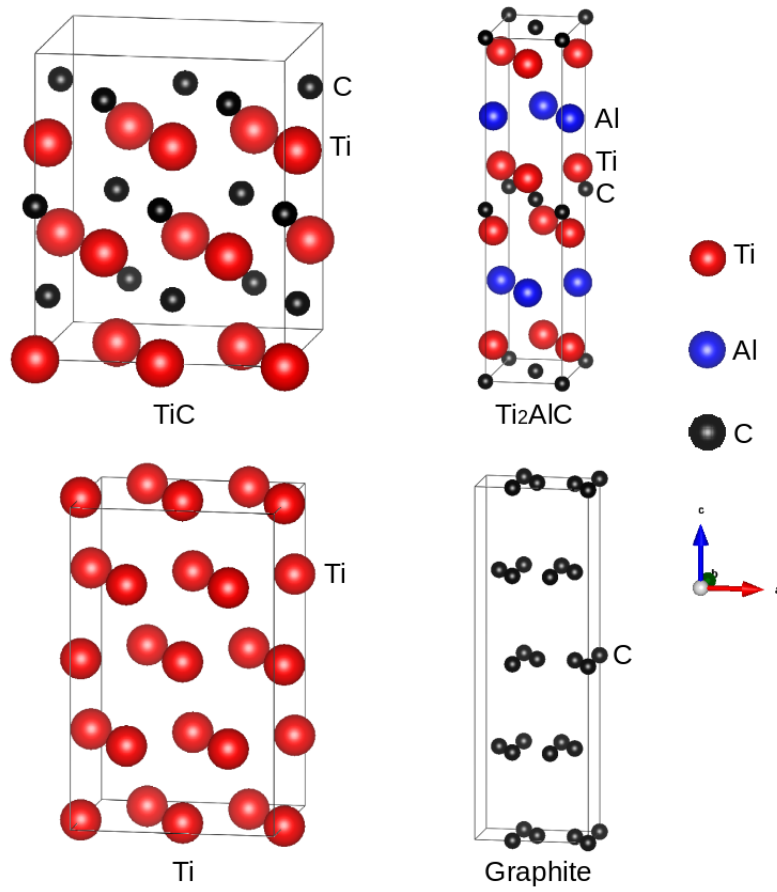
Figure 5.1: Crystal structures of the (a) TiC, (b) Ti$_2$AlC, (c) Ti, and (d) Graphene.

by VESTA. For the calculations of TiC, Ti_2AlC, and Ti systems, metallic, ionic, and covalent bonds are dominant so that van der Waals force can be negligible. However, for the calculations of graphite, the van der Waals force is dominant between layers, thus vdW-DF method has been used. This method considers non-local correlation functional so that it approximately accounts for the electronic dispersion interactions.

The elastic constants are calculated using VASP with IBRION = 6 flag. This flag allows to determine the Hessian matrix, which is the second derivatives of the energy for atomic positions. For the calculation of elastic constants, ISIF = 3 flag is used with IBRION = 6 flag, which allows lattice distortions during the relaxation of systems. Then the elastic tensor is determined by the strain-stress relationship. The calculated elastic constants of TiC, Ti_2AlC, Ti, and graphite are described below in the unit of GPa:

$$C_{ij}(TiC) = \begin{bmatrix} 500 & 138 & 152 & 0 & -21 & 0 \\ 138 & 492 & 164 & 0 & 22 & 0 \\ 152 & 164 & 477 & 0 & -1 & 0 \\ 0 & 0 & 0 & 175 & 0 & -18 \\ -21 & 22 & -1 & 0 & 184 & 0 \\ 0 & 0 & 0 & -18 & 0 & 187 \end{bmatrix}, \tag{5.1}$$

$$C_{ij}(Ti_2AlC) = \begin{bmatrix} 302 & 68 & 64 & 0 & 0 & 0 \\ 68 & 302 & 64 & 0 & 0 & 0 \\ 64 & 64 & 268 & 0 & 0 & 0 \\ 0 & 0 & 0 & 175 & 0 & 0 \\ 0 & 0 & 0 & 0 & 175 & 0 \\ 0 & 0 & 0 & 0 & 0 & 117 \end{bmatrix}, \tag{5.2}$$

$$C_{ij}(Ti) = \begin{bmatrix} 170 & 94 & 82 & 0 & 0 & 0 \\ 94 & 170 & 83 & 0 & 0 & 0 \\ 82 & 83 & 186 & 0 & 0 & 0 \\ 0 & 0 & 0 & 39 & 0 & 0 \\ 0 & 0 & 0 & 0 & 38 & 0 \\ 0 & 0 & 0 & 0 & 0 & 39 \end{bmatrix}, \tag{5.3}$$

$$C_{ij}(Graphite) = \begin{bmatrix} 1061 & 187 & -4 & 0 & 0 & 0 \\ 187 & 1064 & -6 & 0 & 0 & 0 \\ -4 & -6 & 41 & 0 & 0 & 0 \\ 0 & 0 & 0 & 425 & 0 & 0 \\ 0 & 0 & 0 & 0 & 3 & 0 \\ 0 & 0 & 0 & 0 & 0 & 3 \end{bmatrix}. \tag{5.4}$$

The calculated C_{11} and C_{33} of TiC are 500 GPa and 477 GPa, and those of Ti are 170 GPa and 186 GPa. The covalent bond in TiC (ceramic) material is stronger than metallic bond in Ti (metal). The calculated C_{11} and C_{33} of Ti$_2$AlC are 302 GPa and 268 GPa. The MAX phases have both ceramic and metal like layers in the system, and the C_{11} and C_{33} values of Ti$_2$AlC are in between TiC (ceramic material) and Ti (metal material). The calculated C_{11} and C_{33} of graphene are 1061 GPa and 41 GPa. In the basal plane, the covalent bond is dominant, which is very strong, thus C_{11} elastic constant value of graphene is very high. However, between basal planes, the van der Waals force is dominant, which is very weak, thus C_{33} elastic constant value of graphene is very low.

5.2 Cleavage Energy

In TiC, Ti$_2$AlC, Ti, and graphite systems, we present the cleavage energy and stress calculations as a function of separation distances. The cleavage behavior is important to understand a material's response to the tensile load, and it can be related to the fracture behavior. In addition, the cleavage energy is important in terms of synthesis of 2-dimensional materials from layered materials by delamination. In 2015, Mahesh et al. reported the shear induced micromechanical
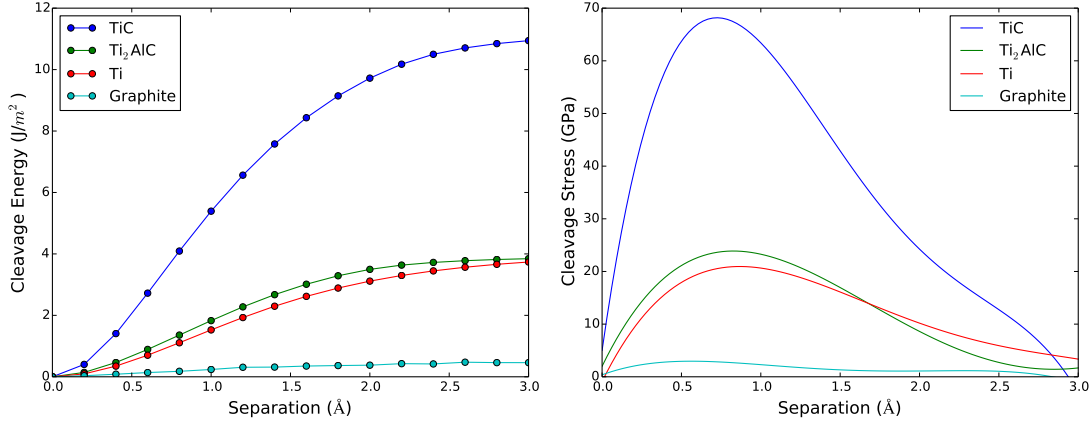
Figure 5.2: (a) Cleavage energy and (b) cleavage stress of TiC, Ti_2AlC, Ti, and graphene.

synthesis of Ti_3SiC_2, which is named as MAXene [50]. This work is very interesting and important, since, generally 2-dimensional MX layers are obtained by selective etching of Al atoms from the MAX phases. These 2-dimensional MX layers are named as MXene, and they have similar properties with graphene. The synthesis of MXene requires toxic HF as an etchant, while the synthesis of MAXene does not require any etchant. The rotational force has applied to Ti_3SiC_2 by the micromechanical milling to partially exfoliate Ti_3SiC_2 layers, then fully exfoliated Ti_3SiC_2 MAXene has obtained by the ultrasonication. In graphene, layers are very weakly bonded by the van der Waals force, and simple ultrasonication can mechanically break the weakly bonded graphite layers. In Ti_3AlC_2 system, layers are strongly bonded compared to the graphene, and it cannot be delaminated by the simple ultrasonication, however, after partial exfoliation by applying rotational force fully exfoliated Ti_3SiC_2 MAXene can be obtained by ultrasonication.

The resultant cleavage energy and stress of TiC, Ti_2AlC, Ti, and graphite are shown in Fig. 5.2. The cleavage energy increases sharply up to around 1 of separation for all cases, and the energy converges to a certain value at about 3 of separation. The cleavage stress is derived from the cleavage energy, and the maximum cleavage stress (critical stress) values of TiC, Ti_2AlC, Ti, and graphite are 66.95, 23.59, 20.51, and 2.90 in the unit of GPa, respectively. The TiC system shows the highest value of critical stress, which shows the ionic bond in ceramic material is very strong
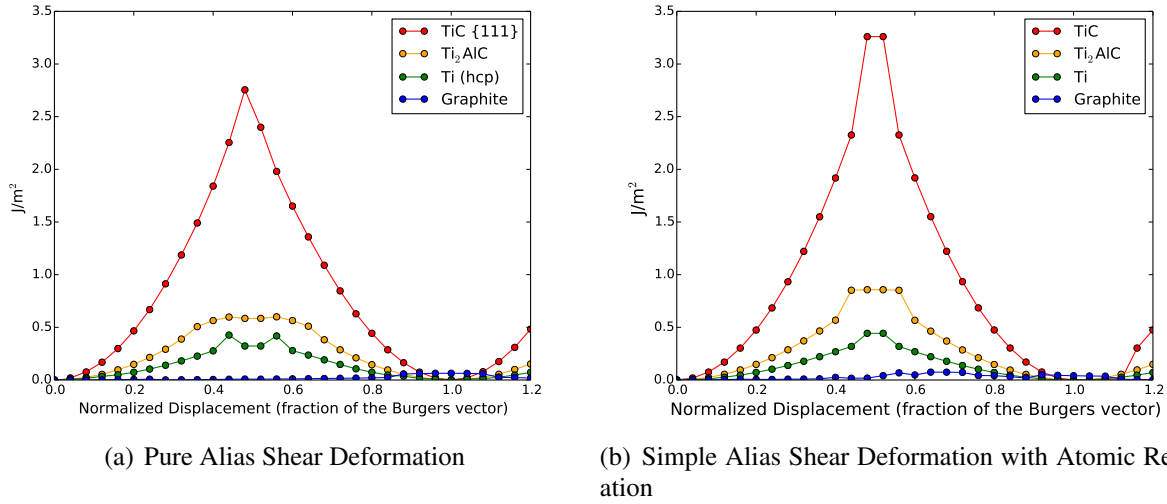
51

(a) Pure Alias Shear Deformation

(b) Simple Alias Shear Deformation with Atomic Relaxation

Figure 5.3: Energy curves of TiC, Ti_2AlC, Ti, and graphite under (a) pure alias shear deformation and (b) simple alias shear deformation with atomic relaxation.

and hard to break. The critical stress of Ti_2AlC is very close to Ti and slightly high. Generally, in MAX phases, metal like A layers are weakly bonded compared to the ceramic like MX layers, and weakly bonded M-A layers plays an important role during the cleavage process. Not surprisingly, Ti_2AlC shows a similar cleavage behavior to Ti. The graphene has the lowest critical stress value, since layers are very weakly bonded with van der Waals force.

5.3   Stacking Fault Energy (SFE)

Here we present energy curves of TiC, Ti_2AlC, Ti, and graphite under pure alias shear deformation and simple alias shear deformation with atomic relaxation, as shown in Fig. 5.3, to study the shear behaviors of different types of materials. In the previous section, we have compared pure alias shear deformation, simple alias shear deformation, and simple alias shear deformation with atomic relaxation, and the resultant energy of simple alias shear deformation is much higher than other cases, thus here we present resultant energies of pure alias shear deformation and simple alias shear deformation with atomic relaxation. MAX phases have both ceramic like MX layers and metal like A layers, which causes the unique combination of properties both of ceramics and metals. To better understand the shear behavior of MAX phases, we studied shear behaviors of ce-

ramics and metals as well as graphite. The shear behaviors of ceramics and metals will help us to understand the property of MAX phases shear behavior like if the shear behavior of MAX phases is similar to ceramics or similar to metals. In addition, we study the shear behavior of graphite to study how the shear behavior of MAX phases is different from the graphite, and see how the ceramic like and metal like bonding in MAX phases are different from the van der Waals force. Further, we would see if van der Waals functional really needs to be considered or not. Under the pure alias shear deformation, the USFE of TiC, Ti$_2$AlC, Ti, and graphite are 2.75, 0.59, 0.42, and 0.06 in the unit of J/m^2, respectively. Under the simple alias shear deformation with atomic relaxation, the USFE of TiC, Ti$_2$AlC, Ti, and graphite are 3.26, 0.85, 0.44, and 0.07 in the unit of J/m^2, respectively. The USFE is around the 0.5 displacement, which related to the generation of stacking fault, and the resultant energies of pure alias shear deformation are lower than those of simple alias shear deformation with atomic relaxation for all cases of different types of materials. Here again, the analysis shows that the relaxation during the shear process is very important to lower the energy and find the most stable and reliable state.

To better understand why the resultant energies under pure alias shear deformation are lower than the resultant energies of simple alias shear deformation with atomic relaxation, we compared pure alias shear deformation to the simple alias shear deformation with atomic relaxation. The strain curves under simple alias shear deformation with atomic relaxation is shown in Fig. 5.4 and under pure alias shear deformation is shown in Fig. 5.5. We calculated normal strains and shear strains. Normal strains, ϵ_{11}, ϵ_{22}, and ϵ_{33} are strains perpendicular to the surfaces, and shear strains, ϵ_{12}, ϵ_{13}, and ϵ_{23} are strains parallel to the surfaces. Simple relaxed alias shear deformation does not allow change of volume and shape of the system, thus only ϵ_{13} is changing linearly, while other strains remain as zero in all cases of TiC, Ti$_2$AlC, Ti, and graphite. The ϵ_{13} corresponds to the displacement of the top layer to the shear direction, along a direction. Pure alias shear deformation allows change of volume and shape of the system during the shear process, thus ϵ_{13} increases linearly with changes of other strains in all cases. In TiC system, at the level of stacking fault generation, ϵ_{33} shows a positive value, and ϵ_{23} shows a negative value, and they are 0.03, and

(a) TiC

(b) Ti$_2$AlC

(c) Ti
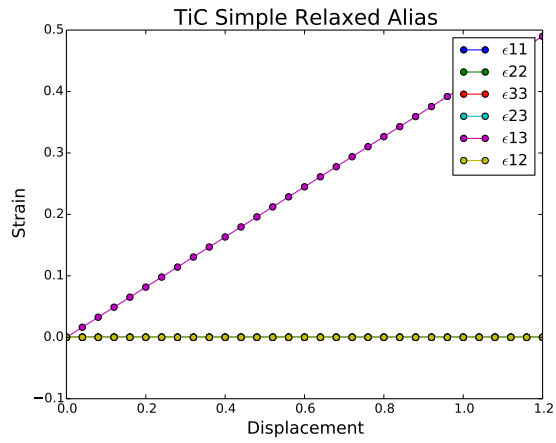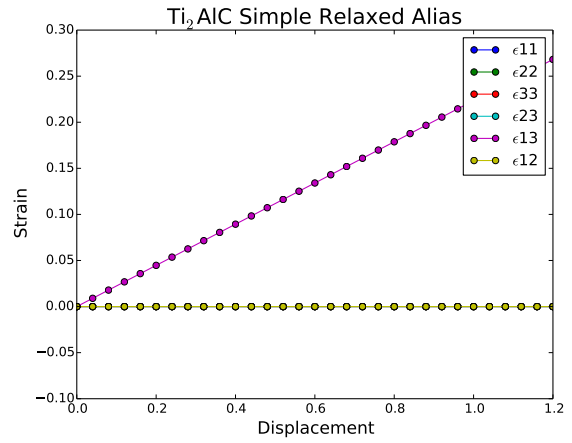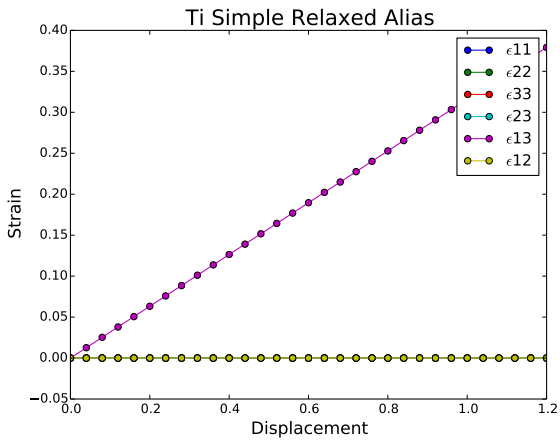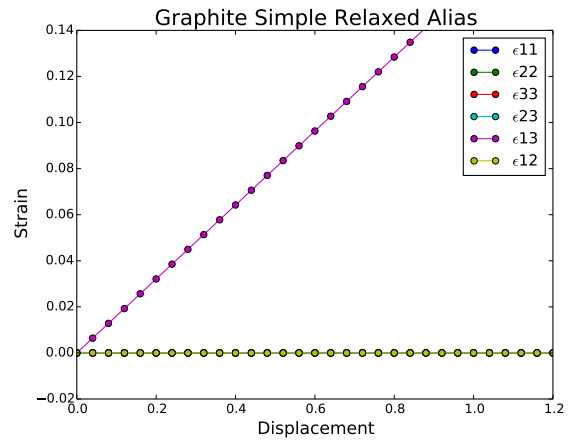
(d) Graphite

Figure 5.4: Strain curves of (a) TiC, (b) Ti$_2$AlC, (c) Ti, and (d) graphite under simple alias shear deformation with atomic relaxation.

54

Figure 5.5: Strain curves of (a) TiC, (b) Ti$_2$AlC, (c) Ti, and (d) graphite under pure alias shear deformation.

-0.02, respectively. In Ti$_2$AlC system, at the level of stacking fault generation, ϵ_{33} shows a positive value, and ϵ_{23} shows a negative value, and they are 0.01, and -0.06, respectively. In Ti system, at the level of stacking fault generation, ϵ_{33} shows a positive value, and ϵ_{23} shows a negative val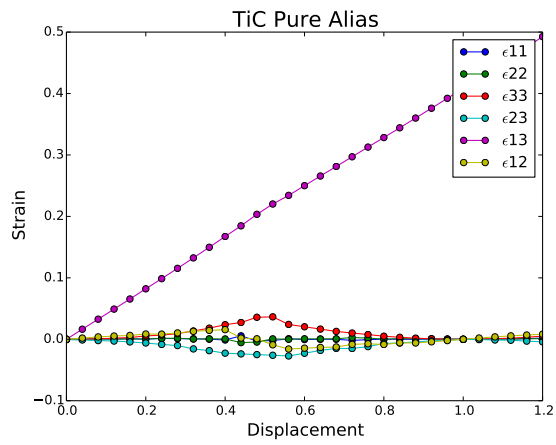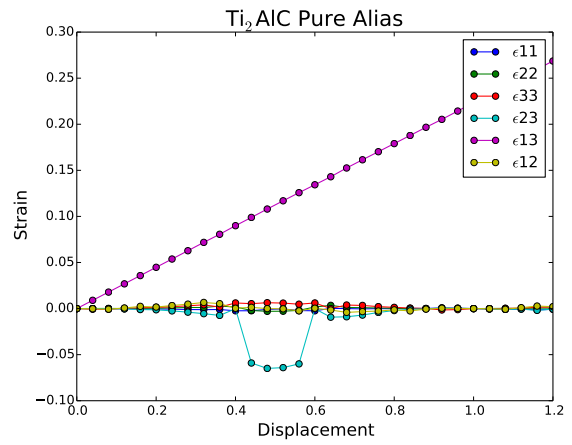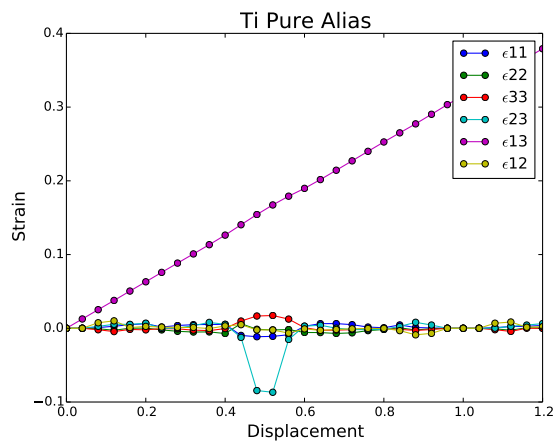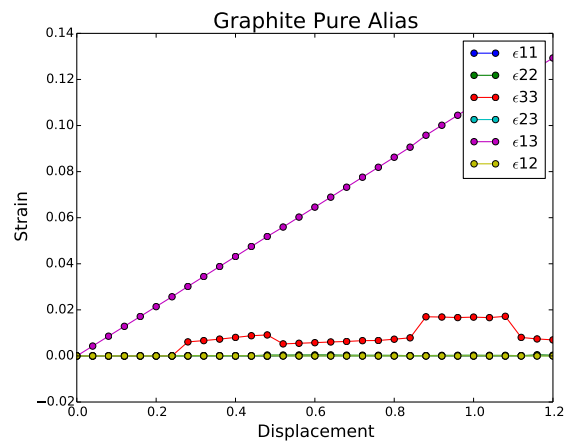ue, and they are 0.01, and -0.08, respectively. In TiC, Ti$_2$AlC, and Ti systems, all have same signs of ϵ_{33}, and ϵ_{23}. However, ϵ_{33} of TiC shows higher positive value than that of Ti$_2$AlC and Ti, thus TiC system expands more along c direction during the shear process than Ti$_2$AlC and Ti systems. In addition, ϵ_{23} of Ti$_2$AlC and Ti systems show lower negative value than that of TiC, thus Ti$_2$AlC and Ti systems have more shear deformation than TiC system. In graphite, ϵ_{33} shows two jumps during the shear deformation, while ϵ_{23} does not change like other systems.

Now, we want to understand why different systems are deforming in different directions with different distances. To understand the deformation behavior, we studied stresses under simple relaxed alias and pure alias shear deformations, shown in Fig. 5.6 and Fig. 5.7. In TiC system, at the level of stacking fault generation, σ_{33} is -145.93, and σ_{23} is 86.08 in the unit of kB, respectively. In Ti$_2$AlC system, σ_{33} is -22.21, and σ_{23} is 60.30 in the unit of kB, respectively. In Ti system, σ_{33} is -16.45, and σ_{23} is 15.60 in the unit of kB, respectively. In TiC, Ti$_2$AlC, and Ti systems, they have negative values of σ_{33}, and positive values of σ_{23}, thus systems expand along c direction and undergo shear deformation along b direction if systems consider relaxation during the shear process, as shown in Fig. 5.5. In graphite system, σ_{33} shows a negative value, but σ_{23} is almost zero, thus graphite expands along c direction without shear deformation along b direction. The analysis suggests that simple relaxed alias shear deformation causes σ_{33} and σ_{23} stresses during the shear process, and the pure alias shear deformation considers relaxation, and causes normal and shear strains, thus σ_{33} and σ_{23} have vanished as shown in Fig. 5.7.

We calculated residual stresses to study the elasticity of shear deformation. The residual stress shows how the stress is different from the elastic stress. The elastic stress is calculated by multiplication of elastic constants and strain. The residual stresses of TiC, Ti$_2$AlC, Ti, and graphite are shown in Fig. 5.8. Particularly, we focused on R_{13}, which shows a degree of elasticity of shear deformation, since top plane moves to a direction during the shear process. In TiC and Ti systems,

(a) TiC

(b) Ti$_2$AlC

(c) Ti
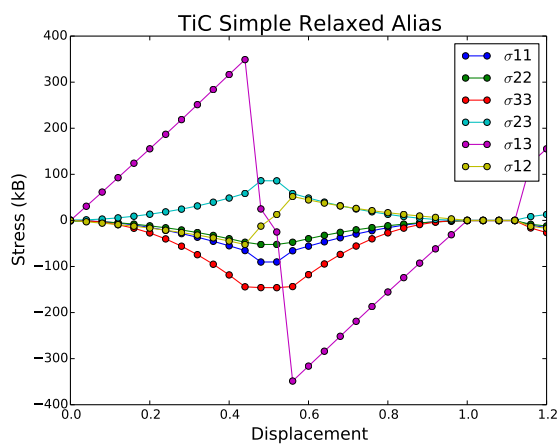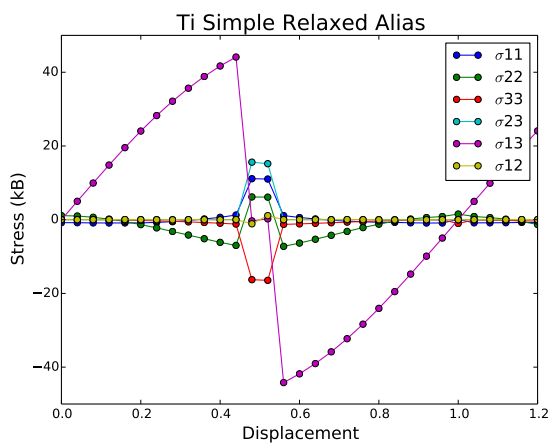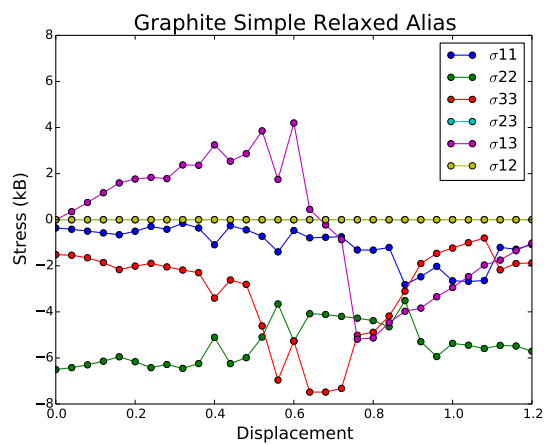
(d) Graphite

Figure 5.6: Stress curves of (a) TiC, (b) Ti$_2$AlC, (c) Ti, and (d) graphite under simple relaxed alias shear deformation.

(a) TiC

(b) Ti$_2$AlC

(c) Ti
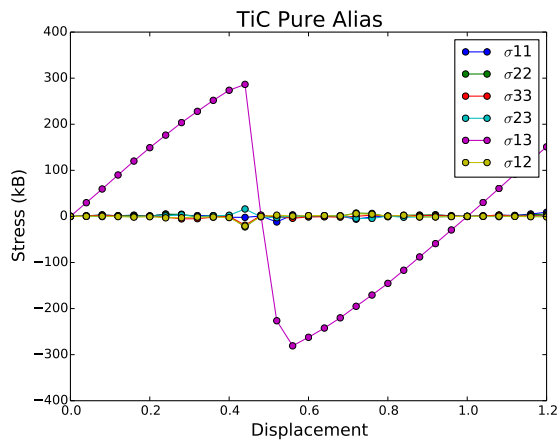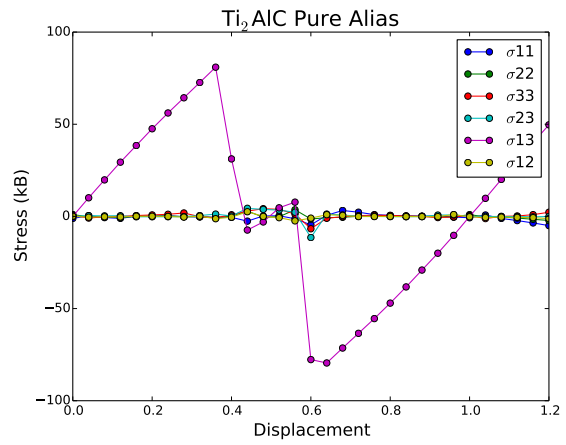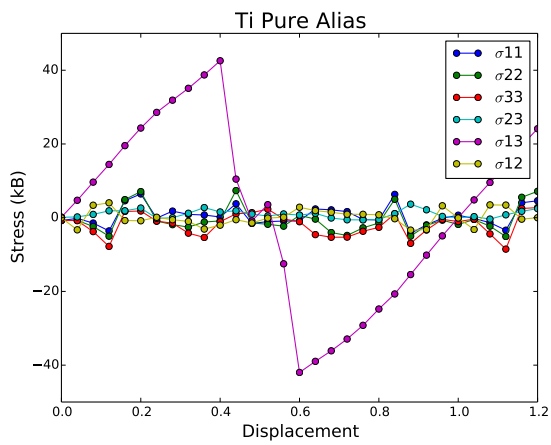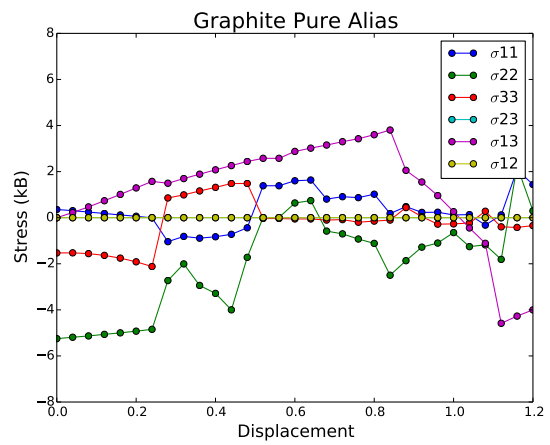
(d) Graphite

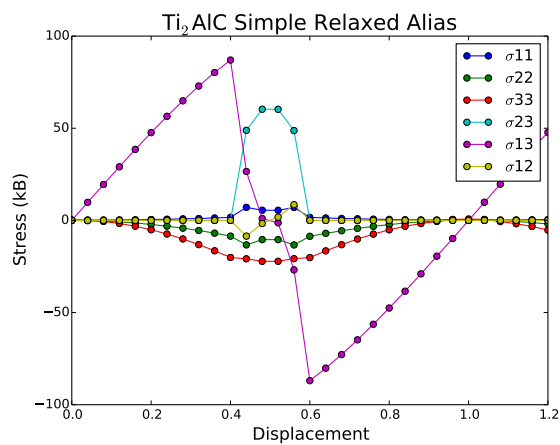Figure 5.7: Stress curves of (a) TiC, (b) Ti$_2$AlC, (c) Ti, and (d) graphite under pure alias shear deformation.

(a) TiC

(b) Ti$_2$AlC

(c) Ti
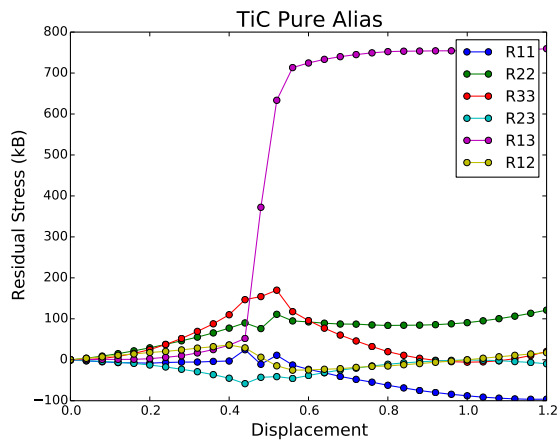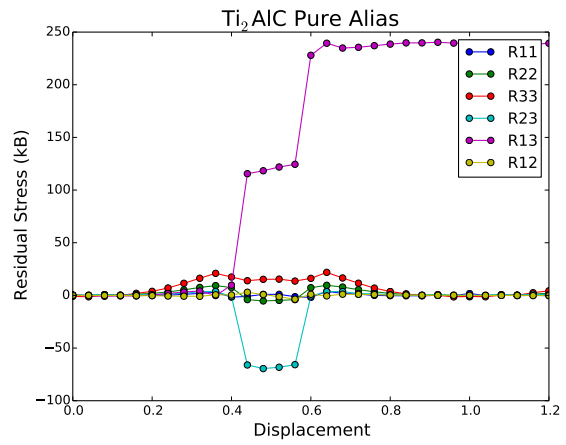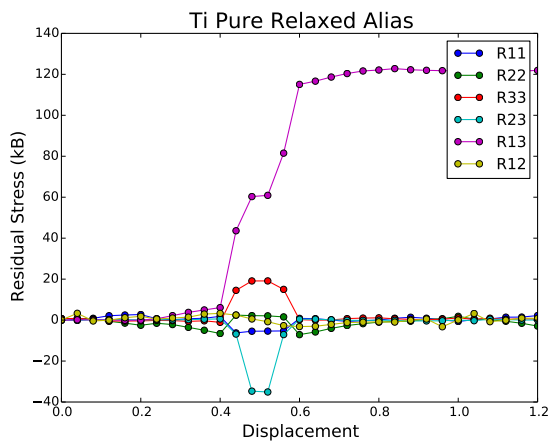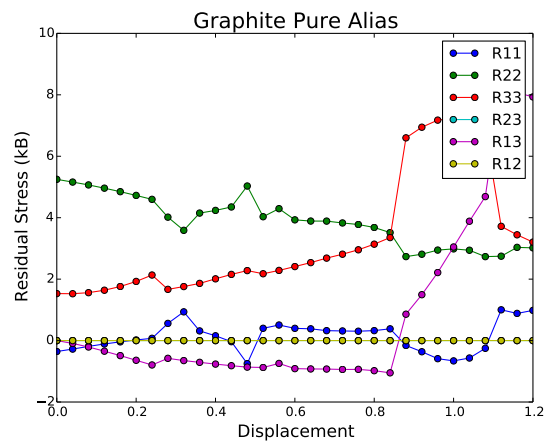
(d) Graphite

Figure 5.8: Residual stress curves of (a) TiC, (b) Ti$_2$AlC, (c) Ti, and (d) graphite under pure alias shear deformation.
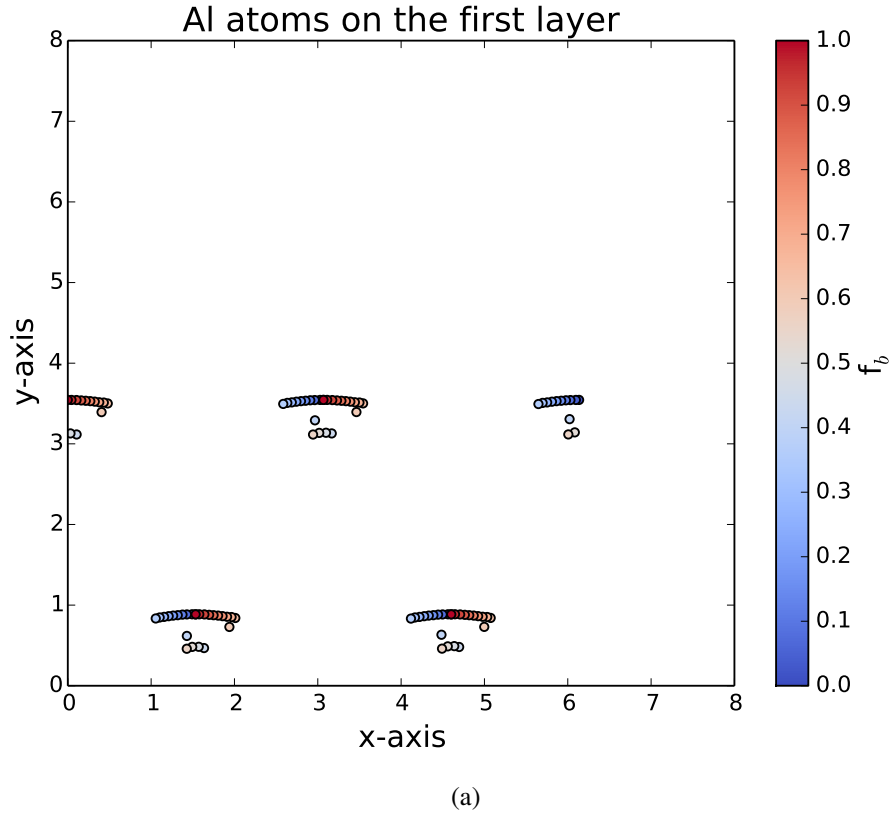
Figure 5.9: In Ti$_2$AlC system, coordinates of Al atoms on the first layer.

R_{13} increases around after 0.2 of displacement. They undergo elastic deformation up to 0.2, then undergo plastic deformation after 0.2. In Ti$_2$AlC system, $_R13$ sharply increases after 0.4. The analysis suggests that the stacking fault generation is plastic deformation, but before the generation of stacking fault, the system deforms elastically.

In the above, we studied how the unit cells deform during the shear process by calculating strain values. Here, in Ti$_2$AlC system, we obtained position coordinates of elements on each layer to study how atoms move during the shear process. The position coordinates of aluminium on the first layer is shown in Fig. 5.9. The color bar represents the shear process, and there are 4 regions, since we have 4 aluminium atoms on the first layer. The shear is applied to the a direction, and at the beginning of the shear deformation, aluminium moves along the a direction linearly. Then, in the middle, aluminium atoms jump along the b direction. The analysis suggests that even though

(a)

(b)

(c)

(d)

(e)

(f)

(g)

(h)
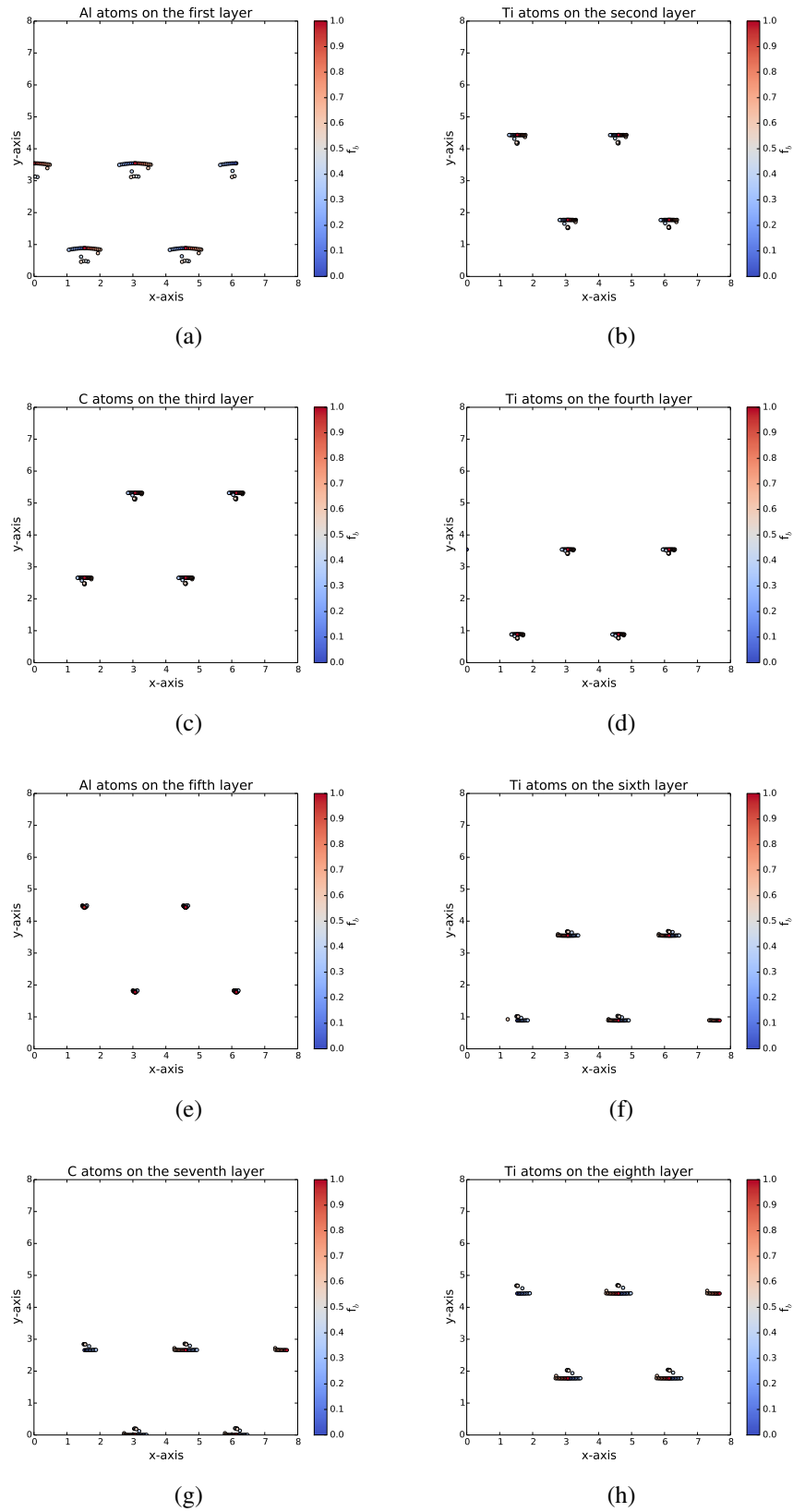
Figure 5.10: In Ti$_2$AlC system, atomic positions of each layers.

61
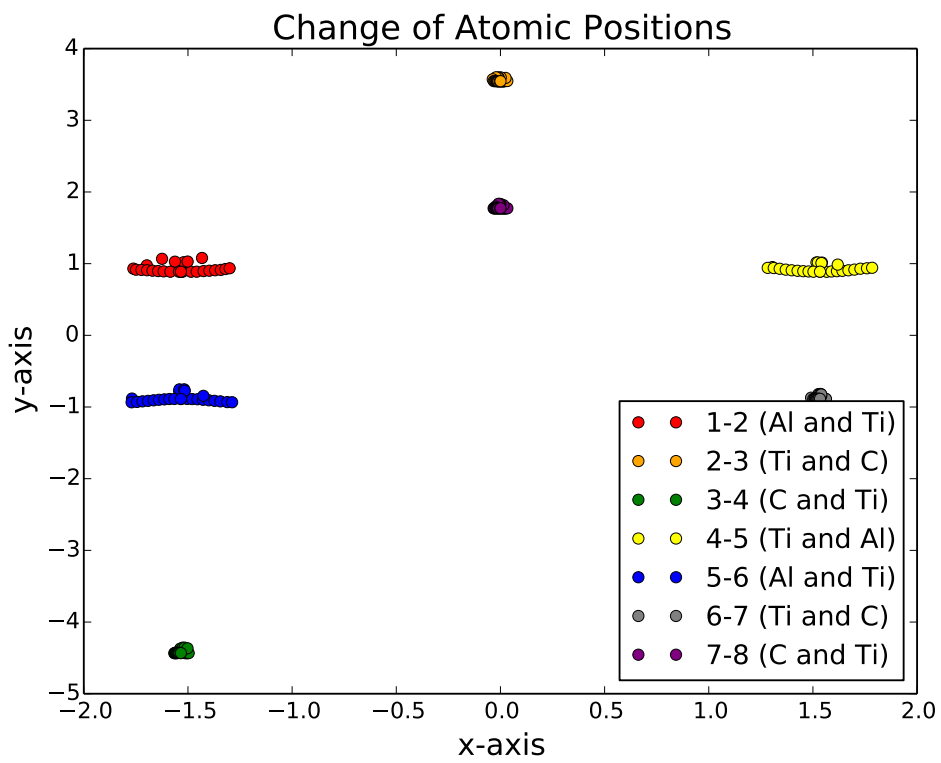
Figure 5.11: In Ti$_2$AlC system, change of atomic positions between neighboured layers.

the shear is applied to the a direction, the stacking fault has generated along the b direction. The position coordinates of elements on all layers are shown in Fig. 5.10. As we studied above, M-A bond strength is relatively weaker than M-X bond strength, thus aluminium atoms move more than titanium and carbon atoms. However, aluminium atoms on the fifth layer, which is a center layer along the c direction, don't move during the shear process. Thus, we calculated the change of atomic positions between neighboring layers, and it is shown in Fig. 5.11. The red, blue, and yellow markers are the change of atomic positions between aluminium and titanium atoms, and other markers are the change of atomic positions between titanium and carbon atoms. The analysis suggests that stacking fault has generated between aluminium and titanium layers.

6.   HIGH-THROUGHPUT DFT CALCULATIONS

6.1   Structural and Elastic Properties of (M_1M_2)AlC MAX phases

In the 1960s, Nowotny and coworkers have discovered MAX phases. In 1996, Barsoum and El-Raghy have reported a unique combination of properties, which are both of metals and ceramics. Many experimental works are done and ongoing successfully. However, the problem is that a family of the possible candidates of MAX phases is very large. We can consider 9 chemicals as M element, 12 chemicals as A element, and carbon and nitrogen as X element. If we consider only 211, 312, and 413 pure MAX phases, we have 648 possible candidates. If we move on to the solid solution MAX phases, the number of possible candidates is extremely increasing. We suggest a high-throughput DFT calculation as a solution to this problem. We studied (M_1M_2)AlC systems, and M = Ca, Sc, Ti, V, Cr, Mn, Fe, Co, Ni, Cu, Zn, Zr, Nb, Mo, Hf, and Ta. We fixed Al as an A element, since aluminium containing MAX phases are expected to have good thermal and oxidation resistance by forming alumina layer at the surface, then studied how the different M site mixing affects structural and elastic properties. The resultant high-throughput DFT calculations for a- and c- lattice parameters, mixing enthalpies, and Young's modulus are shown in Fig. 6.1. Lattice parameters of a and c of (M_1M_2)AlC systems are shown in Fig. 6.1(a) and 6.1(b). Basically different M elements have their own atomic radius and electron negativity, thus (M_1M_2)AlC systems have different a and c lattice parameters with different M elements. Mixing enthalpy is shown in Fig. 6.1(c), which is an energy of (M_1M_2)AlC subtracted from energies of its pure elements like M_1, M_2, Al, and C. The negative value of mixing enthalpy means that (M_1M_2)AlC system is stable upon mixing. However, to precisely study the stability of (M_1M_2)AlC systems, the study of the stability of binary, ternary, and quaternary byproducts has to be followed. Lastly, Young's modulus of (M_1M_2)AlC systems are shown in Fig. 6.1(d). Here, we plot Young's modulus as a function of the a-lattice parameter, and it shows that if we have a specific target Young's modulus, we can design a-lattice parameter from different (M_1M_2)AlC systems. Tuning
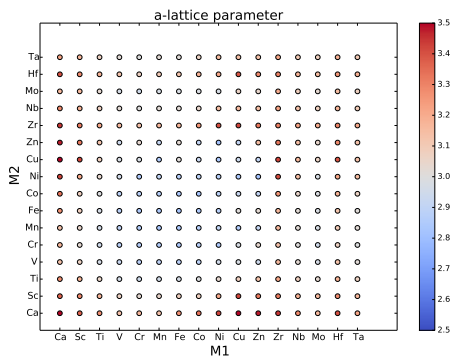
(a) a-Lattice parameter
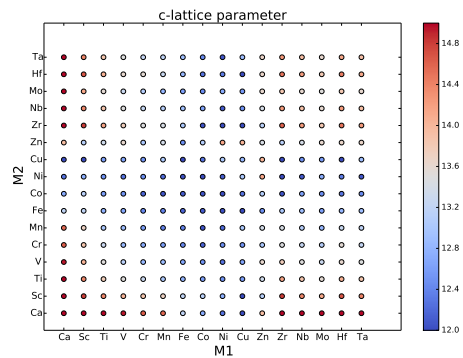
(b) c-Lattice parameter
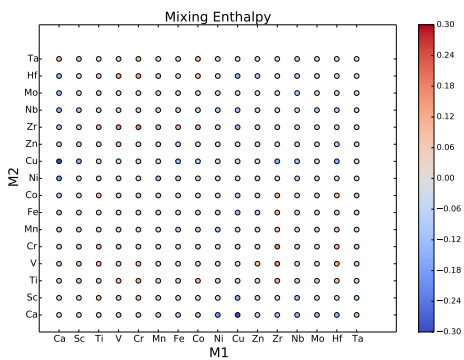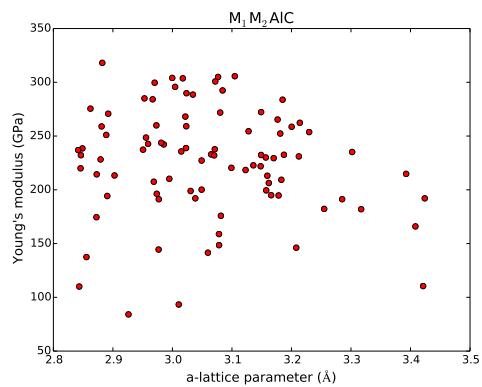
(c) Mixing Enthalpy

(d) Young's modulus

Figure 6.1: (a) a-Lattice parameter, (b) c-lattice parameter, (c) mixing enthalpy, (d) Young's modulus of $(M_1 M_2)$AlC

(a) Cleavage Energy   (b) Cleavage Stress
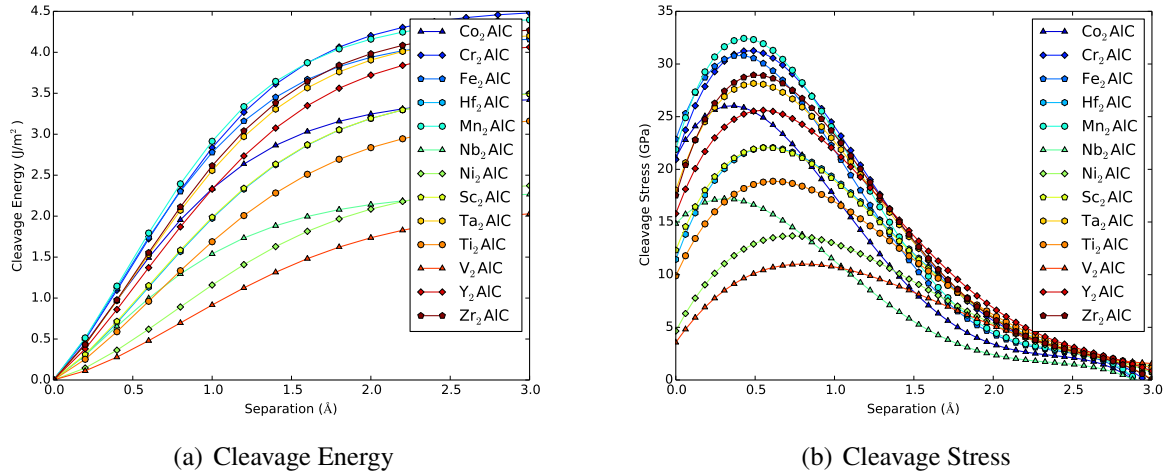
Figure 6.2: (a) Cleavage energy and (b) cleavage stress of the M_2AlC.

lattice parameter is important in the application of a coating, since lattice mismatch stress plays an important role in the stability of coated layer.

6.2 Cleavage and Stacking Fault Energies

Here we studied the cleavage behavior of M_2AlC systems with M = Sc, Ti, V, Cr, Mn, Fe, Co, Ni, Y, Zr, Nb, Hf, and Ta. Again aluminium is fixed as an A element and studied how different M elements affect the cleavage behavior. Particularly we studied 211 systems, since in the previous section we studied how different stacking numbers affect cleavage behavior, and the analysis suggest that the stacking number does not significantly affect the cleavage behavior. The calculated cleavage energy and stress are shown in Fig. 6.2. The cleavage energies increase sharply up to around 1 of separation for all cases, and the energy converges to certain value at about 3 . The calculated critical stresses are shown in Table 6.1 and Fig. 6.4, and the sequence exactly follows the sequence of M element in periodic table. In the first row of the table, from Sc_2AlC to Mn_2AlC the critical stress increases, then from Mn_2AlC to Ni_2AlC the critical stress decreases. In the second row of the table, from Y_2AlC to Nb_2AlC the critical stress increases. Lastly, in the third row of the table, from Hf_2AlC to Ta_2AlC the critical stress increases. When we compare the critical stresses of M_2AlC in the same columns, the critical stress decreases from first row to second row, then

66

	Sc$_2$AlC	Ti$_2$AlC	V$_2$AlC	Cr$_2$AlC	Mn$_2$AlC	Fe$_2$AlC	Co$_2$AlC	Ni$_2$AlC
	13.68	22.06	28.15	31.25	32.42	30.80	26.03	17.21

	Y$_2$AlC	Zr$_2$AlC	Nb$_2$AlC
	11.01	18.86	25.60

	Hf$_2$AlC	Ta$_2$AlC
	22.07	28.94

Table 6.1: The critical stress of M$_2$AlC systems with M = Sc, Ti, V, Cr, Mn, Fe, Co, Ni, Y, Zr, Nb, Hf, and Ta in the unit of GPa.

	Sc$_2$AlC	Ti$_2$AlC	V$_2$AlC	Cr$_2$AlC	Mn$_2$AlC	Fe$_2$AlC	Co$_2$AlC	Ni$_2$AlC
M	-1.46	-1.99	-1.47	-0.96	+0.37	+0.67	+0.90	+0.94
Al	+0.78	+0.98	+0.50	-0.06	-2.55	-2.84	-2.95	-2.98
C	+2.15	+3.00	+2.44	+2.00	+1.79	+1.49	+1.14	+1.09

	Y$_2$AlC	Zr$_2$AlC	Nb$_2$AlC
M	-1.49	-2.60	-1.01
Al	+0.84	+1.21	+0.84
C	+2.15	+3.98	+2.15

	Hf$_2$AlC	Ta$_2$AlC
M	-3.02	-2.89
Al	+1.36	+0.62
C	+4.68	+5.16

Table 6.2: Charge transfer of M, Al, and C elements is obtained by Bader analysis for M$_2$AlC systems with M = Sc, Ti, V, Cr, Mn, Fe, Co, Ni, Y, Zr, Nb, Hf, and Ta.
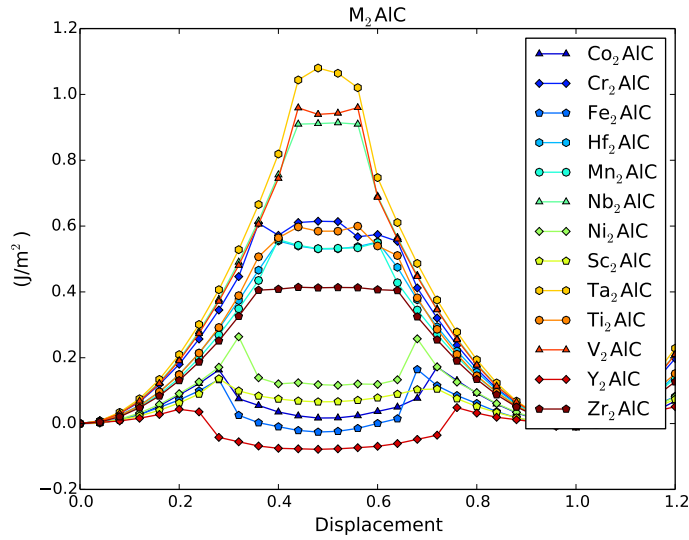
Figure 6.3: Shear energy curves of the M_2AlC under $\langle 2\bar{1}\bar{1}0 \rangle \{0001\}$ pure alias shear deformation

the critical stress increases from second row to third row. To better understand a trend of critical stresses, we calculated the charge transfer, which is shown in Table 6.2. Hafnium and tantalum in third row have larger atomic volume than M elements is first and second rows. However both hafnium and tantalum have very low charge transfer, which means they lose more electrons and turn to highly positive charged ions. Thus both Hf_2AlC and Ta_2AlC in third row have high critical stresses.

Here we studied the shear behavior of M_2AlC systems with M = Sc, Ti, V, Cr, Mn, Fe, Co, Ni, Y, Zr, Nb, Hf, and Ta. Again aluminium is fixed as an A element and studied how different M element affect the shear behavior. The calculated shear energies are shown in Figure 6.3. Ta_2AlC system has the highest energy barrier during the shear process at around a 0.5 of displacement, and Y_2AlC has the lowest energy barrier during the shear process at around a 0.2 of displacement. The analysis suggest that if M-A bond is strong, the USFE value is high and stacking fault is generated at the late stage during the shear process, and if M-A bond is weak, the USFE value is low and stacking fault is generated at the early stage during the shear process. The calculated USFE of M_2AlC systems are shown in Table 6.3 and Fig. 6.4. In the first row, USFE increases from Sc_2AlC

Sc$_2$AlC	Ti$_2$AlC	V$_2$AlC	Cr$_2$AlC	Mn$_2$AlC	Fe$_2$AlC	Co$_2$AlC	Ni$_2$AlC
0.13	0.59	0.95	0.61	0.55	0.16	0.17	0.26

Y$_2$AlC	Zr$_2$AlC	Nb$_2$AlC
0.05	0.41	0.91

	Hf$_2$AlC	Ta$_2$AlC
	0.55	1.08

Table 6.3: The unstable stacking fault energies (USFE) of M$_2$AlC systems with M = Sc, Ti, V, Cr, Mn, Fe, Co, Ni, Y, Zr, Nb, Hf, and Ta in the unit of J/m^2.
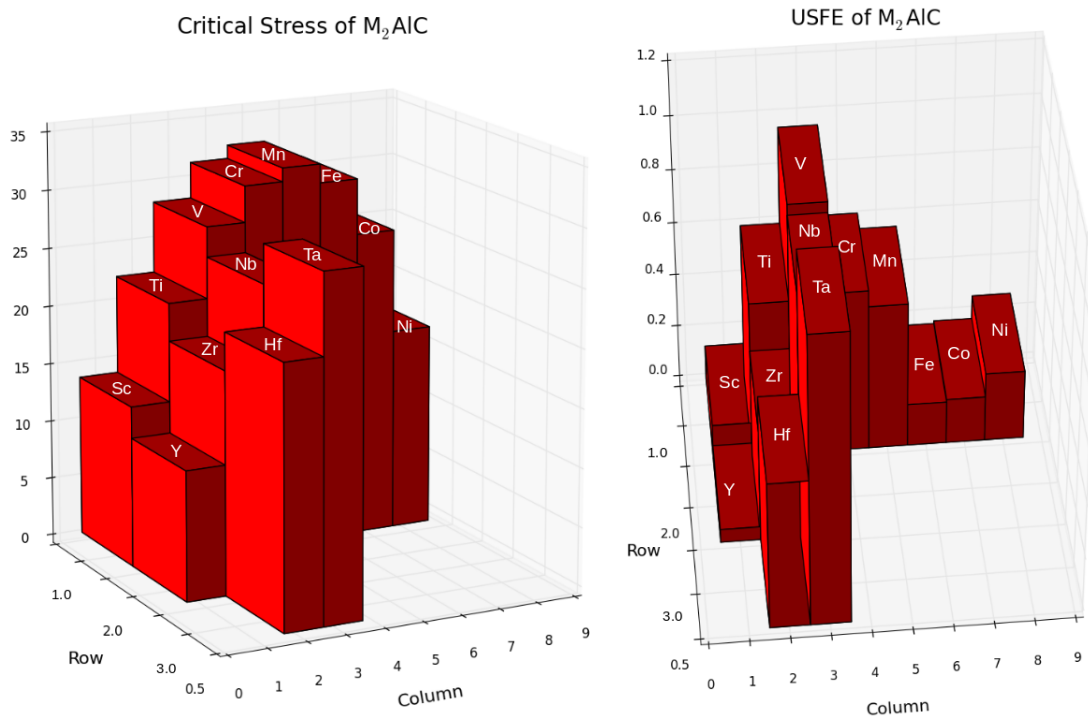
Figure 6.4: Critical stress and USFE of M$_2$AlC MAX phases.

to V_2AlC, then USFE decreases from V_2AlC to Fe_2AlC. In the second row, USFE increases from Y_2AlC to Nb_2AlC. Lastly, in the third row, USFE increases from Hf_2AlC to Ta_2AlC. A trend of USFE is very similar to that of critical stress.

The shear energy curves show that the Y_2AlC system has a stable sheared structure. In addition, Fe_2AlC, Co_2AlC, Sc_2AlC, Ni_2AlC systems have a meta stable sheared structure. Thus we studied stacking sequences of Y_2AlC system. The plane view normal to the b direction and a direction are shown in Fig. 6.5. In the plane view normal to the b direction, there is no difference on stacking sequences before and after shearing. However, in the plane view normal normal to the a direction, there is a stacking sequence difference before and after shearing. If we see solid, dashed, and dotted line in the upper half and lower half planes, all the atoms are aligned in the same sequences. However, the stacking fault has generated in the shaded region. To better understand, the Al-Y_1-Y_2 stacking sequences are shown in Fig. 6.6. Before the shearing, Al-Y_1-Y_2 has ABA stacking sequence. However, after the searing, Al-Y_1-Y_2 has ABC stacking sequence. The analysis suggests that Y, Fe, Co, Sc, and Ni can have stable or meta stable sheared structure with ABC stacking sequence of Al-Y_1-Y_2.

Figure 6.5: Crystal structures of Y_2AlC before and after shearing.

Figure 6.6: Different stacking sequences of A, M1, M2 before and after shearing.

7. CONCLUSIONS

First, we investigated the structural, electronic, elastic, thermodynamic, and mechanical properties of $Ti_3(Si_xAl_{1-x})C_2$ systems to understand the composition-properties relationship. The c-lattice parameter decreases and the elastic modulus increase with increasing amount of Si. To address this, the charge d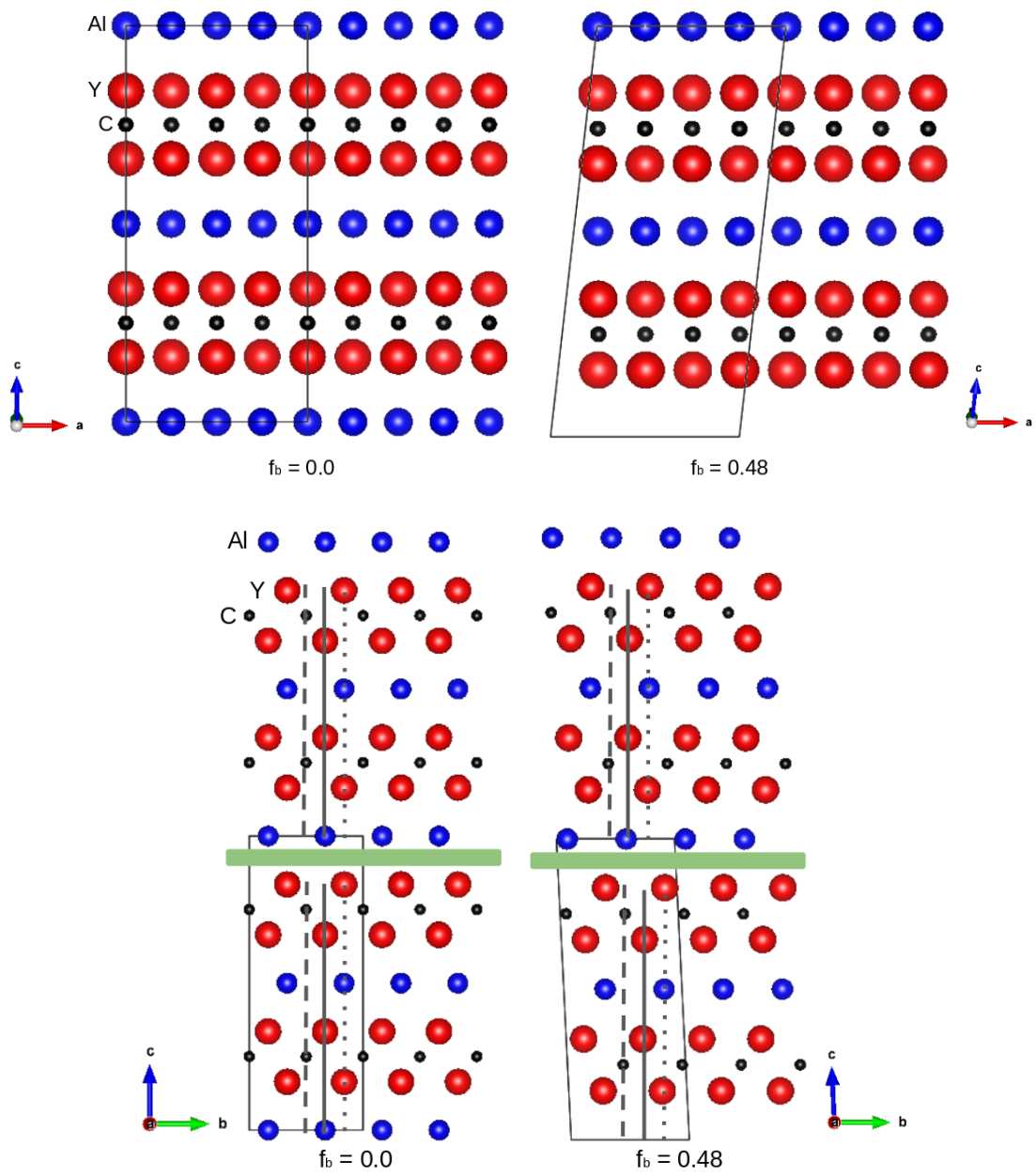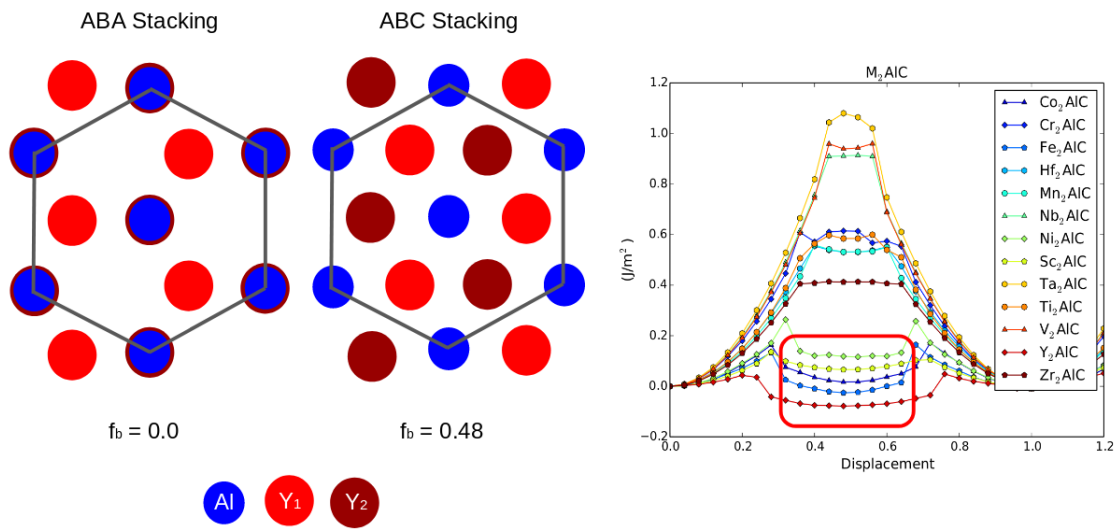ensity analysis is followed, and the charge density analysis shows that the charge density near the A element atom increases with increasing amount of Si makes the M-A bond stronger. In addition, the critical stress and USFE increase with increasing amount of Si. The stacking fault energy is investigated along the a and b directions, and the analysis shows that the a direction shear deformation is more preferable than the b direction shear deformation, since the a direction shear deformation shows lower USFE than that of the b direction shear deformation. We considered pure alias, pure affine, simple alias, and simple affine shear deformations. The analysis shows that the pure alias shear deformation is most preferable, which mean that the top layer moves first and the displacement propagates to lower layers during the shear process.

Second, we studied the effect of number of stacking layers on deformation behaviors to understand the structural-properties relationship. This study was motivated by the question of whether the number of stacking layers in MAX phases played a important role in their intrinsic cleavage and shear behaviors. Our results suggest that there is no significant effect of the number of stacking layers on the cleavage and shear behaviors. With different stacking numbers in $Ti_{n+1}AlC_n$ and $Ta_{n+1}AlC_n$ systems with n = 1-5, they show similar critical energies and USFE. The cleavage and shear behaviors are dominated by the weakly bonded M-A layers, and the stacking number does not affect significantly the M-A bond strength.

Third, we studied cleavage and shear behaviors of different types of layered materials Ti_2AlC, TiC, Ti, and graphite. The MAX phases have a unique combination of properties both of ceramics and metals, and this study was motivated by whether the deformation behaviors of MAX phases are similar the ceramics or metals. Our results show that the critical stress and USFE of Ti_2AlC (MAX phases) are close to those of Ti (metal). Thus, we would say the MAX phases are similar

to metals in terms of the deformation behaviors. We also calculated the critical stress and USFE of graphite, and they are dramatically low when compared to Ti_2AlC, TiC, and Ti. This result might be able to show why only the graphite can be fully delaminated using the simple ultra sonication. In addition, in Ti_2AlC system, we studied which and how atoms move during the shear deformation. Our results suggest that if the a direction shear is applied to the system, the Al atoms displace along the b direction.

Lastly, we used high-throughput DFT calculations to study structural and elastic properties of $(M_1M_2)AlC$ systems with M = Ca, Sc, Ti, V, Cr, Mn, Fe, Co, Ni, Cu, Zn, Zr, Nb, Mo, Hf, and Ta. Our results show that lattice parameter and elastic properties can be tuned within the wide range when we consider solid solution MAX phases. For example the a lattice parameter is in the range from around 2.85 to around 3.45 , and the Young's modulus is in the range from around 80 GPa to around 320 GPa. The mixing enthalpy briefly shows the possibility of synthesis of $(M_1M_2)AlC$. In addition we studied cleavage and shear behaviors of $(M_1M_2)AlC$. The stacking fault energy analysis shows that some MAX phases (M = Y, Fe, Co, Sc, and Ni) have stable or meta stable states with sheared structure. M_2AlC have ABA stacking before the shear deformation, and have ABC stacking after shear deformation. Al displaces during the shear deformation, and Al can stay in different lattice site with stable or meta stable state if M_2AlC has Y, Fe, Co, Sc, or Ni as a M element.

REFERENCES

[1] W. Son, H. Gao, T. Duong, A. Talapatra, M. Radovic, and R. Arróyave, "Effect of a mixing on elastic modulus, cleavage stress, and shear stress in the $Ti_3(Si_xAl_{1-x})C_2$ max phase," *Physical Review B*, vol. 95, no. 23, p. 235131, 2017.

[2] H. Gao, R. Benitez, W. Son, R. Arroyave, and M. Radovic, "Structural, physical and mechanical properties of $Ti_3(Al_{1-x}Si_x)C_2$ solid solution with x= 0–1," *Materials Science and Engineering: A*, vol. 676, pp. 197–208, 2016.

[3] W. Son, T. Duong, A. Talapatra, H. Gao, R. Arróyave, and M. Radovic, "Ab-initio investigation of the finite-temperatures structural, elastic, and thermodynamic properties of Ti_3AlC_2 and Ti_3SiC_2," *Computational Materials Science*, vol. 124, pp. 420–427, 2016.

[4] W. Son, T. Duong, A. Talapatra, E. Prehn, Z. Tan, M. Radovic, and R. Arróyave, "Minimal effect of stacking number on intrinsic cleavage and shear behavior of $Ti_{n+1}AlC_n$ and $Ta_{n+1}AlC_n$ MAX phases," *Journal of Applied Physics*, vol. 123, no. 22, p. 225102, 2018.

[5] W. Jeitschko, H. t. Nowotny, and F. Benesovsky, "Carbides of formula t2mc," *Journal of the Less Common Metals*, vol. 7, no. 2, pp. 133–138, 1964.

[6] W. Jeitschko, H. Nowotny, and F. Benesovsky, "Die h-phasen Ti_2TlC, Ti_2PbC, Nb_2InC, Nb_2SnC und Ta_2GaC," *Monatshefte für Chemie und verwandte Teile anderer Wissenschaften*, vol. 95, no. 2, pp. 431–435, 1964.

[7] H. Wolfsgruber, H. Nowotny, and F. Benesovsky, "Die kristallstruktur von Ti_3GeC_2," *Monatshefte für Chemie und verwandte Teile anderer Wissenschaften*, vol. 98, no. 6, pp. 2403–2405, 1967.

[8] W. Jiang, J. Zhang, and L. Wang, "Spark plasma sintering of max phases and their related composites," in *MAX Phases and Ultra-High Temperature Ceramics for Extreme Environments*, pp. 1–33, IGI Global, 2013.

[9] M. W. Barsoum, "The $M_{N+1}AX_n$ phases: A new class of solids: Thermodynamically stable nanolaminates," *Progress in Solid State Chemistry*, vol. 28, no. 1-4, pp. 201–281, 2000.

[10] M. W. Barsoum and M. Radovic, "Elastic and mechanical properties of the MAX phases," *Annual review of materials research*, vol. 41, pp. 195–227, 2011.

[11] M. Radovic and M. W. Barsoum, "MAX phases: bridging the gap between metals and ceramics," *American Ceramics Society Bulletin*, vol. 92, no. 3, pp. 20–27, 2013.

[12] M. Sundberg, G. Malmqvist, A. Magnusson, and T. El-Raghy, "Alumina forming high temperature silicides and carbides," *Ceramics International*, vol. 30, no. 7, pp. 1899–1904, 2004.

[13] X. Wang and Y. Zhou, "High-temperature oxidation behavior of Ti_2AlC in air," *Oxidation of Metals*, vol. 59, no. 3, pp. 303–320, 2003.

[14] G. Song, Y. Pei, W. Sloof, S. Li, J. T. M. De Hosson, and S. Van der Zwaag, "Oxidation-induced crack healing in Ti_3AlC_2 ceramics," *Scripta Materialia*, vol. 58, no. 1, pp. 13–16, 2008.

[15] H. Yang, Y. Pei, J. Rao, and J. T. M. De Hosson, "Self-healing performance of Ti_2AlC ceramic," *Journal of Materials Chemistry*, vol. 22, no. 17, pp. 8304–8313, 2012.

[16] M. Radovic, M. Barsoum, A. Ganguly, T. Zhen, P. Finkel, S. Kalidindi, and E. Lara-Curzio, "On the elastic properties and mechanical damping of Ti_3SiC_2, Ti_3GeC_2, $Ti_3Si_{0.5}Al_{0.5}C_2$ and Ti_2AlC in the 300–1573k temperature range," *Acta Materialia*, vol. 54, no. 10, pp. 2757–2767, 2006.

[17] P. Finkel, M. Barsoum, and T. El-Raghy, "Low temperature dependencies of the elastic properties of Ti_4AlN_3, $Ti_3Al_{1.1}C_{1.8}$, and Ti_3SiC_2," *Journal of Applied physics*, vol. 87, no. 4, pp. 1701–1703, 2000.

[18] Z. Sun, "Progress in research and development on MAX phases: a family of layered ternary compounds," *International Materials Reviews*, vol. 56, no. 3, pp. 143–166, 2011.

[19] J.-P. Palmquist, S. Li, P. Å. Persson, J. Emmerlich, O. Wilhelmsson, H. Högberg, M. Katsnelson, B. Johansson, R. Ahuja, O. Eriksson, *et al.*, "$M_{n+1}AX_n$ phases in the Ti- Si- C system studied by thin-film synthesis and ab initio calculations," *Physical Review B*, vol. 70, no. 16, p. 165401, 2004.

[20] M. W. Barsoum and T. El-Raghy, "Synthesis and characterization of a remarkable ceramic: Ti_3SiC_2," *Journal of the American Ceramic Society*, vol. 79, no. 7, pp. 1953–1956, 1996.

[21] X. Tong, T. Okano, T. Iseki, and T. Yano, "Synthesis and high temperature mechanical properties of Ti_3SiC_2/SiC composite," *Journal of materials science*, vol. 30, no. 12, pp. 3087–3090, 1995.

[22] J. Zhang, L. Wang, W. Jiang, and L. Chen, "Fabrication of high purity Ti_3SiC_2 from Ti/Si/C with the aids of Al by spark plasma sintering," *Journal of alloys and compounds*, vol. 437, no. 1-2, pp. 203–207, 2007.

[23] E. Schrödinger, "An undulatory theory of the mechanics of atoms and molecules," *Physical review*, vol. 28, no. 6, p. 1049, 1926.

[24] M. Born and R. Oppenheimer, "Zur quantentheorie der molekeln," *Annalen der Physik*, vol. 389, no. 20, pp. 457–484, 1927.

[25] L. H. Thomas, "The calculation of atomic fields," in *Mathematical Proceedings of the Cambridge Philosophical Society*, vol. 23, pp. 542–548, Cambridge University Press, 1927.

[26] E. Fermi, "Un metodo statistico per la determinazione di alcune priorieta dellâĂŹatome," *Rend. Accad. Naz. Lincei*, vol. 6, no. 602-607, p. 32, 1927.

[27] P. Hohenberg and W. Kohn, "Inhomogeneous electron gas," *Physical review*, vol. 136, no. 3B, p. B864, 1964.

[28] W. Kohn and L. J. Sham, "Self-consistent equations including exchange and correlation effects," *Physical review*, vol. 140, no. 4A, p. A1133, 1965.

[29] J. P. Perdew and A. Zunger, "Self-interaction correction to density-functional approximations for many-electron systems," *Physical Review B*, vol. 23, no. 10, p. 5048, 1981.

[30] J. P. Perdew and Y. Wang, "Accurate and simple analytic representation of the electron-gas correlation energy," *Physical Review B*, vol. 45, no. 23, p. 13244, 1992.

[31] G. Kresse and J. Furthmüller, "Efficient iterative schemes for ab initio total-energy calculations using a plane-wave basis set," *Physical review B*, vol. 54, no. 16, p. 11169, 1996.

[32] G. Kresse and J. Furthmüller, "Efficiency of ab-initio total energy calculations for metals and semiconductors using a plane-wave basis set," *Computational materials science*, vol. 6, no. 1, pp. 15–50, 1996.

[33] R. P. Feynman, "Forces in molecules," *Physical Review*, vol. 56, no. 4, p. 340, 1939.

[34] P. E. Blöchl, "Projector augmented-wave method," *Physical review B*, vol. 50, no. 24, p. 17953, 1994.

[35] A. Van de Walle, P. Tiwary, M. De Jong, D. Olmsted, M. Asta, A. Dick, D. Shin, Y. Wang, L.-Q. Chen, and Z.-K. Liu, "Efficient stochastic generation of special quasirandom structures," *Calphad*, vol. 42, pp. 13–18, 2013.

[36] S. Ganeshan, S. Shang, Y. Wang, and Z.-K. Liu, "Effect of alloying elements on the elastic properties of Mg from first-principles calculations," *Acta Materialia*, vol. 57, no. 13, pp. 3876–3884, 2009.

[37] J. Zhang, Y. Li, Y. Wang, Z. Liu, L. Chen, Y. Chu, F. Zavaliche, and R. Ramesh, "Effect of substrate-induced strains on the spontaneous polarization of epitaxial bifeo 3 thin films," *Journal of applied physics*, vol. 101, no. 11, p. 114105, 2007.

[38] S. Shang, Y. Wang, and Z.-K. Liu, "First-principles elastic constants of α-and θ-Al_2O_3," *Applied Physics Letters*, vol. 90, no. 10, p. 101909, 2007.

[39] R. Hill, "The elastic behaviour of a crystalline aggregate," *Proceedings of the Physical Society. Section A*, vol. 65, no. 5, p. 349, 1952.

[40] A. Van De Walle, M. Asta, and G. Ceder, "The alloy theoretic automated toolkit: A user guide," *Calphad*, vol. 26, no. 4, pp. 539–553, 2002.

[41] S. Wei and M. Chou, "Ab initio calculation of force constants and full phonon dispersions," *Physical review letters*, vol. 69, no. 19, p. 2799, 1992.

[42] A. Van De Walle and G. Ceder, "The effect of lattice vibrations on substitutional alloy thermodynamics," *Reviews of Modern Physics*, vol. 74, no. 1, p. 11, 2002.

[43] P. Lazar and R. Podloucky, "Cleavage fracture of a crystal: Density functional theory calculations based on a model which includes structural relaxations," *Physical Review B*, vol. 78, no. 10, p. 104114, 2008.

[44] M. Jahnátek, J. Hafner, and M. Krajčí, "Shear deformation, ideal strength, and stacking fault formation of fcc metals: A density-functional study of al and cu," *Physical Review B*, vol. 79, no. 22, p. 224103, 2009.

[45] T. Bučko, J. Hafner, and J. G. Ángyán, "Geometry optimization of periodic systems using internal coordinates," *The Journal of chemical physics*, vol. 122, no. 12, p. 124508, 2005.

[46] G. Bei, V. Gauthier-Brunet, C. Tromas, and S. Dubois, "Synthesis, characterization, and intrinsic hardness of layered nanolaminate Ti_3AlC_2 and $Ti_3Al_{0.8}Sn_{0.2}C_2$ solid solution," *Journal of the American Ceramic Society*, vol. 95, no. 1, pp. 102–107, 2012.

[47] A. A. Voevodin, D. V. Shtansky, E. A. Levashov, and J. J. Moore, *Nanostructured thin films and nanodispersion strengthened coatings*, vol. 155. Springer Science & Business Media, 2006.

[48] P. Lazar and R. Podloucky, "Ab initio study of tension-shear coupling in NiAl," *Physical Review B*, vol. 75, no. 2, p. 024112, 2007.

[49] P. Lazar and R. Podloucky, "Ab initio study of the mechanical properties of NiAl microalloyed by X= Cr, Mo, Ti, Ga," *Physical Review B*, vol. 73, no. 10, p. 104114, 2006.

[50] A. áPeer Mohamed *et al.*, "Shear induced micromechanical synthesis of Ti$_3$SiC$_2$ MAXene nanosheets for functional applications," *RSC Advances*, vol. 5, no. 63, pp. 51242–51247, 2015.